1-1-2012

Coffee-Rings and Glasses: Colloids Out of Equilibrium

Peter Joseph Yunker
University of Pennsylvania, peter.yunker@gmail.com

Coffee-Rings and Glasses: Colloids Out of Equilibrium

Abstract
This thesis describes experiments that utilize colloids to explore nonequilibrium phenomena. Specifically, the deposition of particles during evaporation and the glass transition are explored.

In the first set of experiments, we found that particle shape has a profound effect on particle deposition. We evaporated drops of colloidal suspensions containing micron-sized particles that range in shape from isotropic spheres to very anisotropic ellipsoids. For sessile drops, i.e., drops sitting on a solid surface, spheres are deposited in a ring-like stain, while ellipsoids are deposited uniformly. We also confined drops between glass plates and allowed them to evaporate. During evaporation, colloidal particles coat the air-water interface, forming colloidal monolayer membranes (CMMs). As particle anisotropy increases, CMM bending rigidity was found to increase. This increase in bending rigidity provides a new mechanism that produces a uniform deposition of ellipsoids and a heterogeneous deposition of spheres.

In the second set of experiments, we employed colloidal suspensions to investigate the character of glassy materials. ``Anisotropic glasses'' were investigated with ellipsoidal particles confined to two-dimensional chambers at high packing fractions; this system enabled the study of the effects of particle shape on the vibrational properties of colloidal glasses. Low frequency modes in glasses composed of slightly anisotropic particles are found to have predominantly rotational character. Conversely, low frequency modes in glasses of highly anisotropic particles exhibit a mix of rotational and translational character.

Aging effects in glasses were explored using suspensions of temperature-sensitive microgel spheres. We devised a method to rapidly quench from liquid to glass states, and then observed the resultant colloidal glasses as they aged. Particle rearrangements in glasses occur collectively, i.e., many particles move in a correlated manner. During aging, we observed that the size of these collective rearrangements increases. Thus, the slowing dynamics of aging appear governed by growing correlated domains of particles required for relaxation.

Using the same microgel particles, the transformation of a crystal into a glass due to added disorder was investigated by adding smaller particles into a quasi-two-dimensional colloidal crystal. The crystal-glass transition bears structural signatures similar to those of the crystal-fluid transition, but also exhibits a sharp change in dynamic heterogeneity which ``turns-on'' abruptly as a function of increasing disorder.

Finally, we investigated the influence of morphology and size on the vibrational properties of disordered clusters of colloidal particles. Spectral features of cluster vibrational modes are found to depend strongly on the average number of nearest neighbors but only weakly on the number of particles in each glassy cluster. The scaling of the median phonon frequency with nearest neighbor number is reminiscent of athermal simulations of the jamming transition.

Degree Type
Dissertation

Degree Name
Doctor of Philosophy (PhD)

COFFEE-RINGS AND GLASSES: COLLOIDS OUT OF EQUILIBRIUM

Peter Joseph Yunker

A DISSERTATION

in

Physics and Astronomy

Presented to the Faculties of the University of Pennsylvania in Partial

Fulfillment of the Requirements for the Degree of Doctor of Philosophy

2012

Arjun G. Yodh, James M. Skinner Professor of Science

Supervisor of Dissertation

A.T. Charlie Johnson, Associate Professor of Physics

Graduate Group Chairperson

Dedication

To my family

Acknowledgements

No man is an island, and even if a graduate student lives alone on an island, no thesis is written alone. I owe a great debt of gratitude to a large number of people. I'll start with those who were with me from the beginning, my parents and siblings. Their love and support is an integral part of who I am today. My parents nurtured my interest in science and technology from a young age, taught me to figure things out on my own, and encouraged me to find a vocation that is also my avocation. Next, I must thank my fianceé and best friend, Erin Buckley. Erin is always there for me, and there's no one in the world I would rather spend time with. From our marathon-first-date in New York, to our engagement to in Paris, I'll always treasure the time we spent together in grad school.

I am tremendously grateful to my advisor, Arjun Yodh. Arjun has been my ideal mentor. He encourages creativity, and allows students to invent and pursue their own ideas - with the understanding that you explain and justify these ideas and experiments in gory detail. Additionally, Arjun taught me a great deal about communication in science, from writing papers to giving talks. I'm embarrassed to think of the first paper I wrote and the first talk I gave in grad school. Thanks to Arjun's direct style of criticism and encouragement, I (hopefully) have progressed significantly from that point.

During my time at Penn, I have been privileged to collaborate with many experts in soft matter. I am especially grateful to Andrea Liu and Tom Lubensky, who inspired many of my experiments, and then helped me to understand them. Randy Kamien consistently would "look-in" on us experimentalists from time-to-time. Doug Durian gave me key advice on a number of occasions. I have also been fortunate to know and work with Kevin Aptowicz, from West Chester

University, and Piotr Habdas, from St. Joseph's University. They both aided me considerably, especially when I was first learning the ropes in research, and it has been especially rewarding to continue working with them.

I don't know that I can thank all of my wonderful labmates enough. I must start by acknowledging Dan Chen and Ahmed Alsayeed, who taught me the basics when I first joined the group, from Köhler illumination to sample preparation. I distinctly remember Ahmed scanning through samples so fast I couldn't even tell what we were looking at and Dan making pristine microscope slides that made the ones I prepared look like my dog made them. But Dan and Ahmed were patient, and they made joining the Yodh group a pleasurable experience. I was also fortunate to work with Yilong Han early in my graduate career. Yilong taught me a great deal about programming in IDL, and crafting a research project in general.

One of the great pleasures I had in my time at Penn was working with my labmate Zexin Zhang. Zexin was a great collaborator, and a better friend. His friendly-optimism was infectious, and his knowledge of chemistry was invaluable. Tim Still was a great source of knowledge about chemistry, discussions about physics, and debates about esoteric subjects. Ke Chen was a valuable collaborator and challenger, who invigorated the lab with his density of states work.

Enormous thanks go to my fellow graduate students, Oni Basu, Matt Lohr, and Matt Gratale. The four of us had a lot of fun together, in and out of physics. Matt Lohr entertained the lab with his unique sense of humor and enthusiasm. As I recall, Gratale and I may have engaged in one or two discussions about sports. Oni proved invaluable as a dog-sitter, making it much easier to leave town. I couldn't have asked for a better set of graduate students to to work and learn with me. I should also thank my classmate and good friend Wesley Baker, who was a great friend to

me during my time here at Penn.

Finally, I should thank my dog, Betty. You may think it is silly to acknowledge an animal in a thesis, but Betty has been an invaluable friend who freely gives her love and happiness to others.

ABSTRACT

COFFEE-RINGS AND GLASSES: COLLOIDS OUT OF EQUILIBRIUM

Peter Joseph Yunker

Arjun G. Yodh

This thesis describes experiments that utilize colloids to explore nonequilibrium phenomena. Specifically, the deposition of particles during evaporation and the glass transition are explored.

In the first set of experiments, we found that particle shape has a profound effect on particle deposition. We evaporated drops of colloidal suspensions containing micron-sized particles that range in shape from isotropic spheres to very anisotropic ellipsoids. For sessile drops, i.e., drops sitting on a solid surface, spheres are deposited in a ring-like stain, while ellipsoids are deposited uniformly. We also confined drops between glass plates and allowed them to evaporate. During evaporation, colloidal particles coat the air-water interface, forming colloidal monolayer membranes (CMMs). As particle anisotropy increases, CMM bending rigidity was found to increase. This increase in bending rigidity provides a new mechanism that produces a uniform deposition of ellipsoids and a heterogeneous deposition of spheres.

In the second set of experiments, we employed colloidal suspensions to investigate the character of glassy materials. “Anisotropic glasses” were investigated with ellipsoidal particles confined to two-dimensional chambers at high packing fractions; this system enabled the study of the effects of particle shape on the vibrational properties of colloidal glasses. Low frequency

modes in glasses composed of slightly anisotropic particles are found to have predominantly rotational character. Conversely, low frequency modes in glasses of highly anisotropic particles exhibit a mix of rotational and translational character.

Aging effects in glasses were explored using suspensions of temperature-sensitive microgel spheres. We devised a method to rapidly quench from liquid to glass states, and then observed the resultant colloidal glasses as they aged. Particle rearrangements in glasses occur collectively, i.e., many particles move in a correlated manner. During aging, we observed that the size of these collective rearrangements increases. Thus, the slowing dynamics of aging appear governed by growing correlated domains of particles required for relaxation.

Using the same microgel particles, the transformation of a crystal into a glass due to added disorder was investigated by adding smaller particles into a quasi-two-dimensional colloidal crystal. The crystal-glass transition bears structural signatures similar to those of the crystal-fluid transition, but also exhibits a sharp change in dynamic heterogeneity which "turns-on" abruptly as a function of increasing disorder.

Finally, we investigated the influence of morphology and size on the vibrational properties of disordered clusters of colloidal particles. Spectral features of cluster vibrational modes are found to depend strongly on the average number of nearest neighbors but only weakly on the number of particles in each glassy cluster. The scaling of the median phonon frequency with nearest neighbor number is reminiscent of athermal simulations of the jamming transition.

Contents

List of Figures

Chapter 1

Introduction

We live in a nonequilibrium world. Everyday, the sun rises, increasing the local temperature, and then sets, decreasing the temperature. Vapor condenses overnight, only to evaporate during the day. Snow melts in the afternoon sun, only to freeze again under the moon. We too are nonequilibrium systems. We consume food, which is broken down to energy and subsequently used or stored. Despite their ubiquity, however, generation of an understanding of nonequilibrium systems represents a major challenge for physicists. Traditional statistical mechanics is applicable to systems that remain in equilibrium. Thus, carefully constructed experimental studies of nonequilibrium media are especially valuable. Controlled experiments in this vein are tools that help guide the effort to develop a non-equilibrium version of statistical mechanics (e.g., [26, 150]).

Colloids are especially well-suited for the study of nonequilibrium phenomena. The traditional colloidal suspension consists of solid particles (e.g., polystyrene), typically 1 nm to 100 μm in size, suspended in a fluid (e.g., water). Ink and paint are common examples of such

colloids. However, colloids are not limited to solids suspended in liquids. Colloids include emulsions, which are fluids suspended in fluids (e.g., milk), aerosols, which are solid particles suspended in gases (e.g., dust), and foams, which are gases suspended in liquids (e.g., styrofoam). Micron-sized colloids are especially useful as they are small enough to experience Brownian motion, but large enough to be easily observed via optical microscopy. In fact, colloidal experiments offer access to both microscopic and macroscopic information, thus (potentially) enabling the two to be directly linked. Colloids are remarkably malleable, too. Almost any aspect of their microscopic properties can be tuned, from particle shape to interparticle interaction to particle packing fraction. In fact, some of these parameters can even be changed *in situ* (e.g., particle size [66, 68, 142, 147, 176]).

The great diversity of colloids presents opportunities to perform a multitude of experiments, but choosing the correct one to match the science sought is challenging. Modification of most parameters produces only trivial changes. A change in the size of colloidal particles at constant volume fraction, for example, does not qualitatively change the suspension's structure or dynamics. Our experimental approach seeks to identify which parameters can induce large qualitative changes. For example, particles with different shapes can exhibit different phase diagrams (e.g., [60, 180]). Along with particle shape, we are especially interested in confinement effects, the competition between order and disorder, and the role of "stickiness" in particles with short-range interparticle interactions. By performing controlled colloidal experiments that carefully examine the effects of these parameters, we have helped to advance knowledge of out-of-equilibrium systems.

In my time at Penn, I have been fortunate to work on a number of fascinating colloidal experiments. This work includes investigations of geometric frustration in buckled colloidal monolayers [68]; use of temperature-sensitive PNIPAM particles to demonstrate structural vestiges of the athermal jamming transition in a thermal system [191]; studying aging in rapidly quenched aging glasses [181]; exploration of disorder-induced transitions from crystal-to-glass [182]; measurement of vibrational properties of jammed colloidal glasses [24]; experimental identification of a class of "soft spots" in colloidal glasses that are likely to rearrange [25]; measurement of the vibrational properties of glasses composed of anisotropic particles [183]; measurement of the vibrational properties of disordered colloidal clusters [184]; comparative studies of differences in correlated rearrangement events in glasses composed of purely repulsive particles and glasses composed of attractive particles [192]; discovery of the effects of particle shape in evaporating drops, e.g., on the coffee-ring effect [186]; and exploration of surfactant effects on the drying of evaporating drops [156]. Very recently, we have explored the role of particle shape in evaporating drops in confinement [185], and the growth process of colloidal particles deposited at the edge of evaporating drops (to be submitted). The rest of this chapter will present a brief overview of the main topics and results covered in this thesis (i.e., references [181–184, 186] and the confined droplet evaporation work). At the end of the chapter an outline of the organization of the dissertation is provided.

1.1 Coffee-Ring Effect

If you have spilled a drop of coffee or tea and left it to dry, then you might have observed that the stain left behind is not uniform, but ring-shaped. Specifically, the stains are darker near the edges

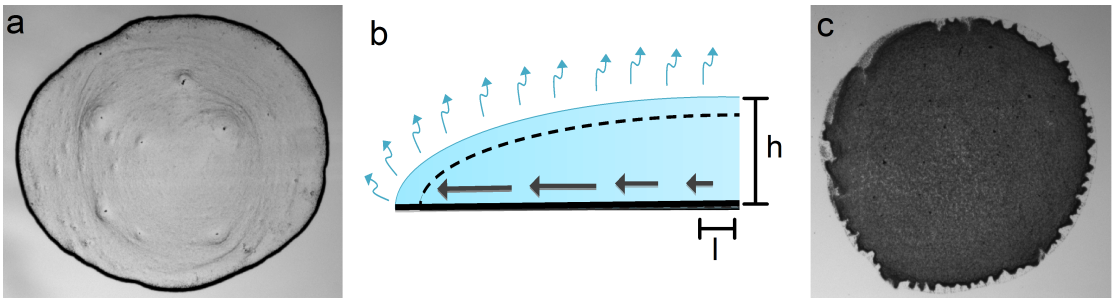

Figure 1.1: a. Image of the coffee-ring left behind when a drop of a suspension of spheres evaporates. b. Schematic diagram of the evaporation process depicting capillary flow induced by pinned edges. If the contact line were free to recede, the drop profile would be preserved during evaporation (dashed line). However, the contact line remains pinned, and the contact angle decreases during evaporation (solid line). Thus, a capillary flow is induced, flowing from the center of the drop to its edges; this flow replenishes fluid at the contact line. c. Image of the uniform coating left behind when a drop of a suspension of spheres evaporates.

than in the middle (Fig. 1.1). While a stray drop of coffee may seem to be of trivial importance, it is actually rich with nonequilibrium physics. The so-called coffee-ring effect is the product of the interplay between fluid dynamics, surface tension, evaporation, diffusion, capillarity, and more. Understanding the coffee-ring effect requires understanding these complex parameters in a far-from-equilibrium setting. Briefly, the edges of a drop easily become pinned and cannot recede towards the middle of a drop, i.e., the diameter of a pinned drop cannot decrease. However, the edges of a drop are thinner than the middle (Fig. 1.1); thus, water flows from the middle of the drop to the edge of the drop to replenish what has evaporated away.

Of course, if the coffee-ring effect were only present in coffee and tea, its practical importance would be nonexistent. In fact, the coffee ring effect is manifest in systems with diverse constituents ranging from large colloids [36–38] to nanoparticles [15] to individual molecules (e.g., salt) [89]. Due to its ubiquity, the coffee-ring manages to cause problems in a wide range of practical applications which call for uniform coatings, such as printing [128], genotyping [46, 47], and complex assembly [39]. Paint is another system susceptible to the coffee-ring effect. To

avoid uneven coats, paints often contain a mixture of two different solvents. One is water, which evaporates quickly, leaving the pigment carrying particles stuck in the second, thicker solvent. The particles are unable to rearrange in this viscous solvent and are then deposited uniformly. Unfortunately, this solvent also evaporates relatively slowly (this is one reason why it might be boring to watch paint dry). While a number of methods to avoid the coffee-ring effect have been discovered [15, 77, 83, 124, 126, 171], they typically involve significant modifications of the system. Thus, finding simple ways to avoid the coffee-ring effect and control particle deposition during evaporation could greatly benefit a wide range of applications.

To this end, we asked (and answered) a simple question: does particle *shape* affect particle deposition [186]? At first glance, it may appear that shape should not matter. Colloidal particles of any shape are susceptible to the radially outward flow of fluid that drives the coffee-ring effect. However, changing particle shape dramatically changes the behavior of particles on the air-water interface. In fact, anisotropic ellipsoids deform the air-water interface while isotropic spheres do not [16, 19, 105, 106, 111, 112, 127]. Deforming the air-water interface induces a strong inter-particle capillary attraction between ellipsoids. This causes ellipsoids to form a loosely-packed network that can cover the entire air-water interface, leaving ellipsoids much more uniformly distributed when evaporation finishes. Conversely, spheres pack densely at the drop's edge, producing a coffee-ring when evaporation has finished. Thus, particle *shape* can produce uniform coatings Fig. 1.1c.

The mechanism that produces a uniform coating requires the presence of an air-water interface that spans the entire area covered by the drop. If a drop is confined between two glass plates, then the air-water interface is only present at the drop edges Fig. 1.2a. However, we

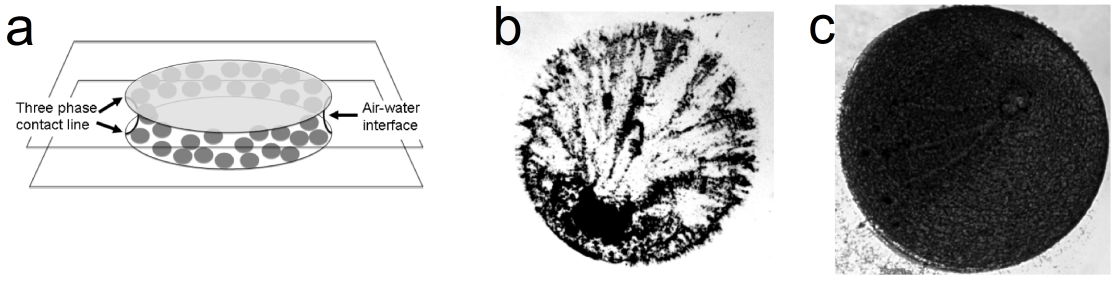

Figure 1.2: a. Cartoon depicting droplet evaporating in a confined geometry. The particle-populated air-water interface and three phase contact lines are labeled. b. Image of the heterogenous deposition of spheres in a confined geometry. c. Image of the homogenous deposition of ellipsoids in a confined geometry.

found that even if a drop is confined between two glass plates, the spheres are still deposited heterogeneously, and the ellipsoids are still deposited uniformly [185] Fig. 1.2b,c. During evaporation, colloids coat the air-water interface. These particle laden interfaces form "colloidal monolayer membranes" (CMMs), which can behave elastically [9, 111, 119, 141, 165]. During evaporation, CMMs are observed to buckle in a manner similar to spherical-shell-shaped elastic membranes [34, 102, 131]. By extending the description of buckled spherical elastic membranes to our quasi-2D geometry [99], we are able to determine the CMM bending rigidity. As particle anisotropy increases, CMM bending rigidity increases as well. This increase in bending rigidity is responsible for the shape-dependent differences in particle deposition in confined drops. The evidence suggests that increased bending rigidity reduces contact line bending and pinning and induces uniform deposition of ellipsoids.

1.2 Glasses

If you ask the layman to describe glass, they'll think of windows and cups, and most likely they will tell you two things: it's transparent and it's hard. The transparency of window glass is

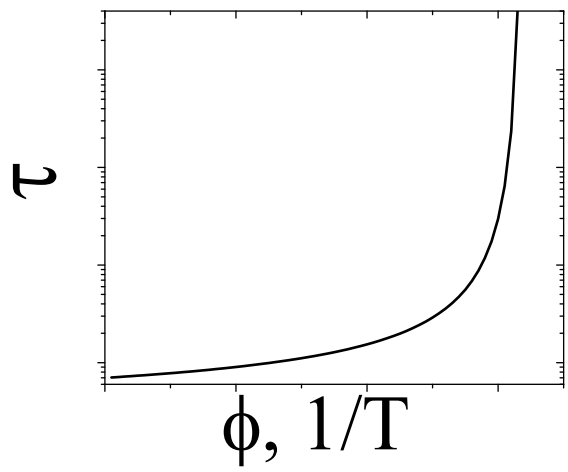

Figure 1.3: The relaxation time, τ, the average time it takes a typical particle in the glass to be displaced by its diameter increases as packing fraction ϕ increases in a colloidal glass, or as T decreases (or 1/T increases) in a molecular glass. While τ increases substantially, it does not change sharply, so the glass transition is defined based on an arbitrary threshold.

understood as a result of an electronic band gap, but the reasons for why glass is hard is an active field of study. While ordered systems undergo a sharp phase transition from liquid to crystal, the transition from liquid to glass is defined more arbitrarily. As the glass transition is approached, particle dynamics dramatically slow down. This is evident from the particle relaxation time (τ), i.e., the average time it takes a typical particle in the glass to be displaced by its diameter (see Fig. 1.3). However, τ does not change discontinuously with respect to volume fraction or temperature and a threshold is arbitrarily selected to define the glass transition point. Compounding this mystery is the rather surprising number of common physical features observed across a broad spectrum of jammed or dynamically arrested systems including colloidal suspensions [169], granular media [2, 168], metallic glasses [148, 149], and polymer glasses [74]. The fact that systems with such different microscopic constituents behave qualitatively similarly has led to a search for unifying explanations.

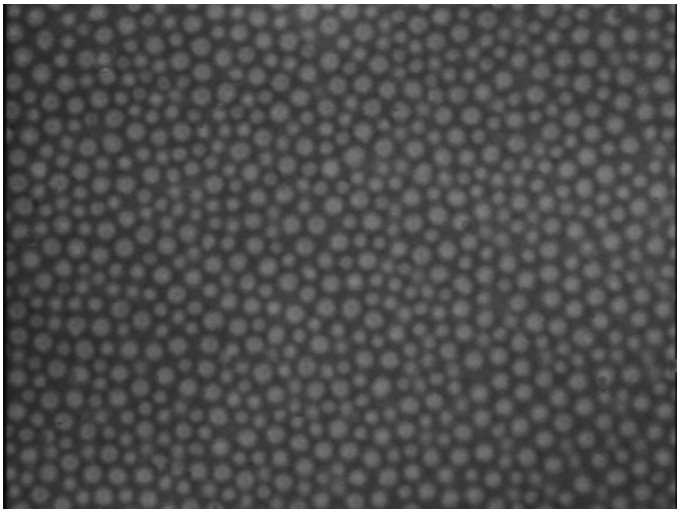

Figure 1.4: Experimental image of a colloidal glass composed of two sizes of PNIPAM particles (~ 1.4 μm and ~ 1.0 μm in diameter) confined between two glass plates to a quasi-2D chamber.

Colloidal glasses are attractive systems to study (see Fig. 1.4). Like molecular and polymer glasses, colloidal glasses are thermal. However, the motions of individual particles can be directly resolved in colloidal glasses, unlike molecular and polymer glasses. Colloidal glass experiments take advantage of this single-particle resolution. For example, collective rearrangements in colloidal glasses were directly imaged, and observed to increase in size as packing fraction increases [169]. Additionally, the interactions of purely repulsive spherical colloidal particles are simpler than the complex interactions of polymers and molecules. This simplicity readily permits direct comparisons with theoretical predictions. Recently, for example, a heroic colloid experiment which measured particle relaxation times varying from 10^{-3} seconds to 10^{5} seconds found significant deviations from mode-coupling theory predictions [17]. In a different vein, experiments performed with soft particles versus packing fraction have discovered a predicted structural signature of the jamming transition [191].

1.2.1 Aging in Glasses

After initial formation, glasses relax via a non-equilibrium process called aging. During aging, glass *dynamics* slow dramatically and become more heterogeneous. Thus, glass dynamics depend on elapsed time from the quench, which we refer to as the waiting time, t_w. This time dependence can be seen in the ensemble-averaged particle mean square displacement (MSD) (Fig. 1.5) [31]. The initial MSD plateau corresponds to particle "in-a-cage" behavior, and the "upturn" at longer times occurs when these cages rearrange. Notice that as aging time t_w increases, the MSD upturn occurs at later times. Here, the upturn time increases by many orders of magnitude until it finally falls outside the experimental window.

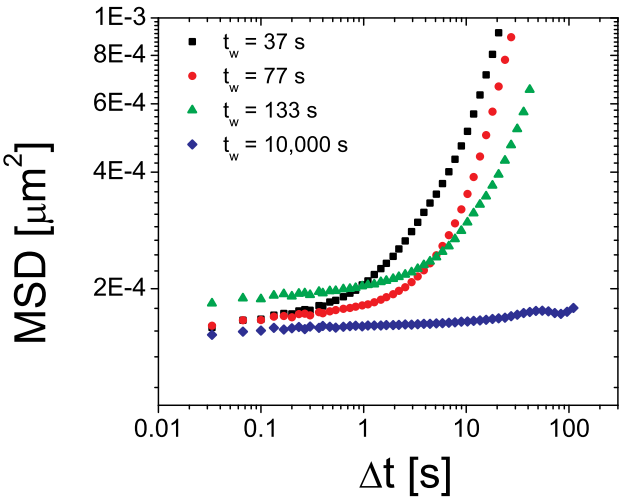

Figure 1.5: The mean square-displacement (MSD) during aging. As aging time, or waiting time (t_w) increases, the upturn in the MSD occurs at later times. Eventually, the upturn does not occur within the experimental window.

Despite such an immense change in particle dynamics, the accompanying structural changes of the colloidal glass have proven difficult to identify [27, 28, 31]. For example, colloidal experiments were performed utilizing magnetic stir bars to "rejuvenate" colloidal glasses [27, 31];

these experiments did not observe any change in structure, even though they found dramatic decreases in dynamics. In their experiments, however, particles continued to flow for a period of time after the stir bar was turned off, and it was difficult to isolate the effects of aging until the flow stopped. Interestingly, simulations suggest that if experiments could observe aging at an earlier time after rejuvenation, they ought to be able to observe structural changes (e.g., [28]).

In the experiments to be presented in this thesis, we rapidly quenched colloidal samples from the liquid phase to the glass phase via optical heating [181]. We dispersed a small amount of red dye in a suspension of temperature-sensitive microgel particles, and illuminated the sample with an intense mercury lamp. The red dye preferentially absorbed the green light from the lamp. The excited dye molecules then relax nonradiatively, thus increasing the temperature of the suspension. This temperature increase is enough to drive (melt) the suspension from the glass phase to the liquid phase. After allowing particles to fluidize, we turn off the lamp. Because the microscope and the rest of the sample remain at their original low temperature, the excess heat dissipates rapidly (< 0.1 seconds), and the suspension is quickly quenched back in to the glass state. At this time, aging begins, and our observation window begins as well.

Thanks to our large observation window (in time), i.e., from the moment the glass is formed and extending $10,000$ seconds, we were able to observe a variation of short-ranged structural order. More significantly, we observed an increase in the number of fast moving particles involved in the collective rearrangements (Fig. 1.7) that significantly change a particle's local neighborhood during aging (Fig. 1.6). This observation provides clues for understanding the slowing dynamics of aging. Over time, rearrangements become more complex and involve more particles, and thus occur less often.

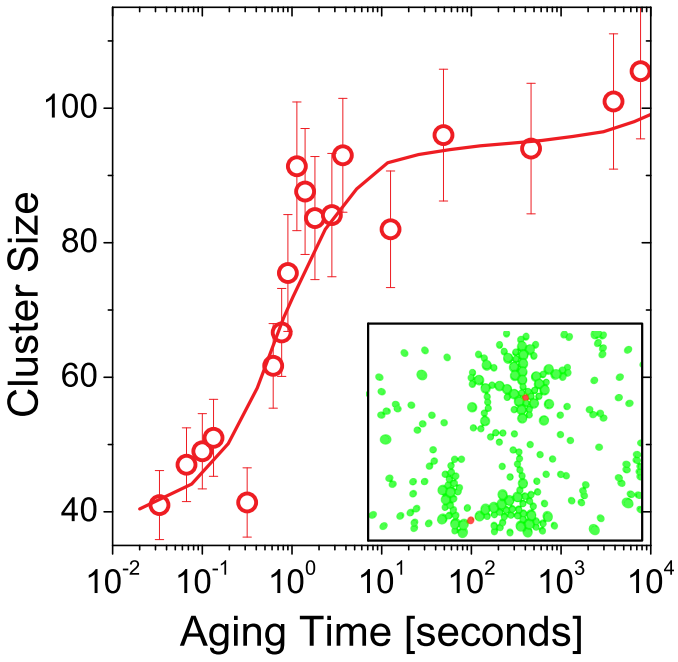

Figure 1.6: The number of fast moving particles involved in the collective rearrangements that significantly change a particle's local neighborhood during aging, plotted versus aging time. Inset: Image of rearranging clusters constructed from experimental data. Green indicates a fast moving particles. Red indicates a particle whose local neighborhood is significantly changing.

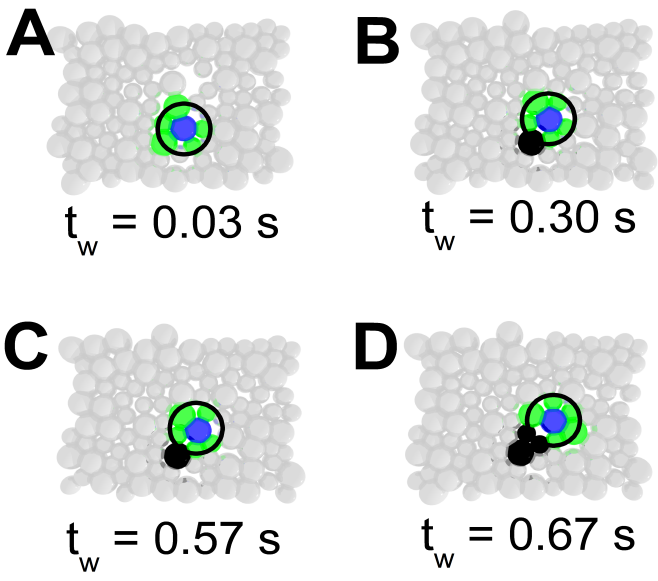

Figure 1.7: a-d. Cartoon of a particle undergoing a cage rearrangement (particle positions taken from experimental data from Chapter 4). The blue particle undergoes a cage rearrangement. These rearrangements are the source of dynamic heterogeneity.

1.2.2 The Crystal-to-Glass Transition

Disorder plays a critical role in traditional melting and freezing phenomena and in the formation of glasses. Melting from crystal-to-fluid, for example, is a sharp transition accompanied by loss of orientational and translational order, and by a dramatic decrease in flow resistance and rearrangement timescale. By contrast, orientational and translational order do not change significantly at the liquid-to-glass transition, even as viscosity and rearrangement timescale diverge [164]; nevertheless frozen-in residual disorder is critical for glass formation.

In two-dimensional glass simulations [65,125,174] and experiments [6,191], it's common to use a mixture of particles with two different diameters. Rapid quenches are sufficient to prevent crystallization and thus a glass forms in three-dimensions [7,8,49,96,115,144,175]. However, in two-dimensions, crystallization occurs much more easily. Thus an additional amount of disorder must be present to prevent crystallization. This is often accomplished by mixing two different sizes of particles (typically with a diameter ratio ~ 1.4). If there aren't enough small particles, then the system will crystallize. Thus, experiments and simulations typically utilize systems with $25 - 50\%$ small particles. We sought to explore what happens between these two limits. Specifically, we varied the fraction of small particles from 0 to 0.5, and we followed the colloidal system as it transitioned from a crystal to a glass (Fig. 1.8).

We found that the transition from crystal-to-glass is much sharper than the transition from liquid-to-glass [182]. The crystal-to-glass transition bears structural signatures similar to those of the crystal-to-liquid transition, but also features a sharp change in particle dynamics. At the transition point, dynamic heterogeneity "turns-on" abruptly. Thus, we may be able to understand the glass transition as the result of an order-to-disorder transition.

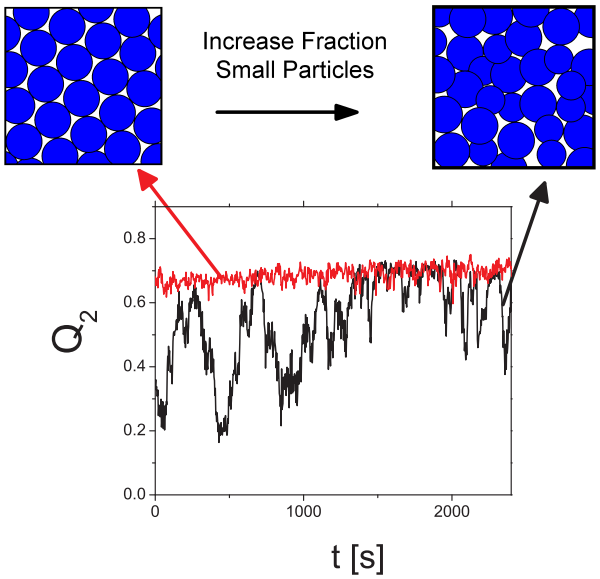

Figure 1.8: Top: Cartoon demonstrating that by adding small particles, a monodisperse crystal can transition to a glass. Bottom: Q_2, the fraction of mobile particles, plotted versus time for crystalline samples (red line) and glass samples (black line).

1.2.3 Particle Shape affects Glass Properties

Much of the physics of glasses has been derived from studying dense suspensions of spheres. Absent friction, the rotation of spheres is unimportant, i.e., for frictionless spheres only translational degrees of freedom are nontrivial. However, the constituent particles of many glasses are anisotropic in shape or have orientation-dependent interactions; such anisotropies are suspected to affect many properties of glasses [44, 45, 82, 97, 114, 152]. Therefore, exploration of glasses composed of anisotropic particles holds potential to uncover new consequences for both the physical mechanisms of the glass transition and for materials applications [170].

We were thus inspired to investigate the effects of particle shape in glasses [183]. Colloidal glasses were prepared, composed of ellipsoidal particles confined in two-dimensional chambers

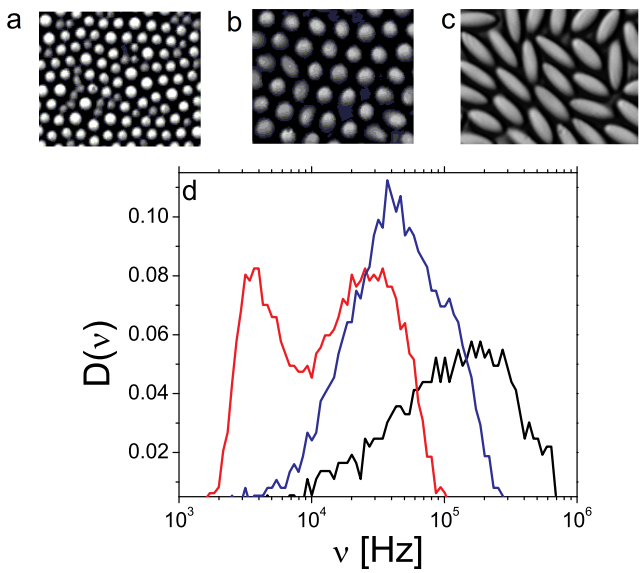

Figure 1.9: a-c. Experimental images of glasses composed of spheres (a), slightly anisotropic particles (b), and very anisotropic particles (c). d. Plot of DOS for glasses composed of spheres (black line), slightly anisotropic particles (red line), and highly anisotropic ellipsoids (blue line).

at high packing fractions (Fig. 1.9). The phonon modes of these ellipsoidal glasses were extracted from measurements of particle displacement correlations. From these experiments, we learned that low frequency modes in glasses composed of ellipsoidal particles with major/minor axis aspect ratios $\sim$1.1 are observed to have predominantly rotational character. Conversely, low frequency modes in glasses of ellipsoidal particles with larger aspect ratios ($\sim$3.0) exhibit a mix of rotational and translational character. All glass samples were characterized by a distribution of particles with different aspect ratios. Interestingly, even within the same sample it was found that small-aspect-ratio particles tend to participate relatively more in rotational modes, while large-aspect-ratio particles tend to participate relatively more in translational modes.

1.3 Disordered Clusters

Investigations of the glass transition have typically focused on dense suspensions of purely repulsive particles. The phase behavior of such systems is controlled by the packing fraction. At low packing fractions these suspensions are fluids, while at high packing fractions these suspensions are solids. Conversely, particles with strong short-range attraction can behave like solids even at low packing fractions (see Fig. 1.10). Specifically, attractive particles can form a gel, which percolates over large distances and can produce macroscopic mechanical response. They also can form dense clusters, which have very large local packing fractions. In fact, dense clusters can look identical to small regions within bulk glasses.

This idea raises some interesting questions. For example, how big does a disordered cluster have to be to behave like a bulk glass? This question is reminiscent of an ancient problem in philosophy, the Sorites' paradox. This paradox asks if items can be precisely defined, or if descriptions are necessarily vague. The traditional statement of this paradox involves a heap of sand: A large pile of sand can easily be described as a "heap." If you take one grain away, you still have a "heap." However, if you do this enough times, you eventually only have one grain, which is clearly not a heap. It's unclear if an exact lower limit can be defined in the number of grains necessary for a heap. Rather than approach disordered clusters philosophically, we sought to explore how cluster morphology and cluster size affect the vibrational properties of disordered materials held together by strong attractive interactions [184]. Since the vibrational properties of bulk colloidal glasses have already been measured [24], one has a clear result for comparison. New understanding thus gained elucidates fundamental differences between glassy materials composed of particles with attractive versus repulsive interactions, uncovers deep connections

between vibrational spectra, mechanical stability, and the jamming problem, and discovers the attributes of a disordered cluster that endow it with the properties of bulk glasses. My experiments on clusters, surprisingly, show that the spectra and character of vibrational modes depend strongly on the average number of neighbors but only very weakly on the number of particles in the cluster. In other words, a cluster with the same average number of neighbors as a bulk glass will behave like a bulk glass regardless of the number of particles in the cluster. Furthermore, our observations about the dependence of median phonon frequency on the average nearest neighbor number parallel concurrent observations about the relationship between local isostatic structures and the average nearest neighbor number. Cluster vibrational properties thus appear to be strongly connected to cluster mechanical stability (i.e., the fraction of locally isostatic regions), and the scaling of median frequency with nearest neighbor number is reminiscent of the behavior of packings of spheres with repulsive interactions at the jamming transition. Computationally generated random networks of springs corroborate observations and further suggest that connections between phonon spectra and nearest neighbor number are generic to disordered networks.

1.4 Technical Advances

Most experiments described in this dissertation utilize relatively standard techniques in new ways. However, some of the experiments required development of new techniques, or extension of old ones to new situations. To study aging glasses, we developed a technique that uses optical heating to rapidly quench microgel suspensions from the liquid phase to the glass phase. In our phonon studies, we extended a technique that calculates a system's vibrational modes from

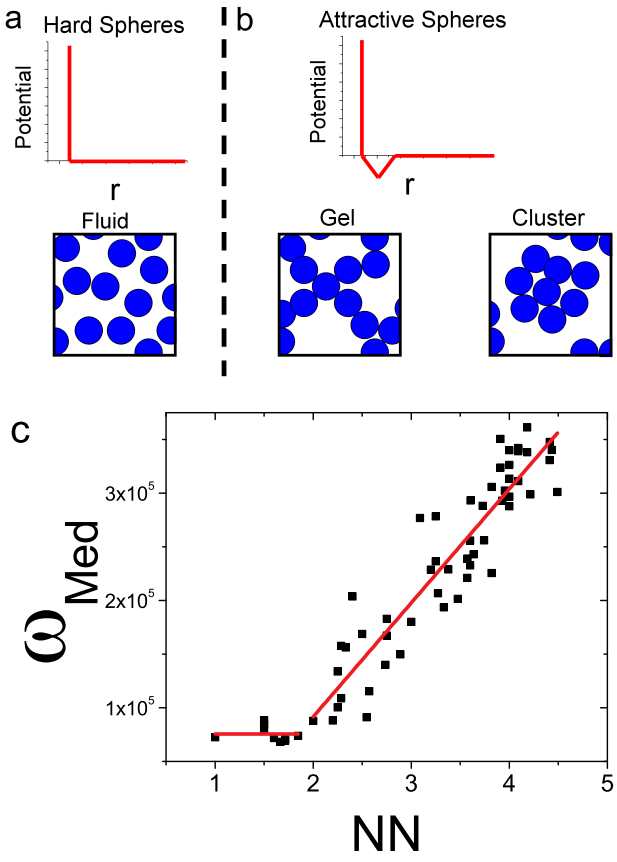

Figure 1.10: a. Purely repulsive hard spheres form a fluid phase at low packing fractions. b. Conversely, particles with short-range attraction can form solid phases at low packing fractions, such as macroscopic gels and locally dense clusters. c. Median vibrational frequency (ω_{Med} plotted versus average number of nearest neighbors (NN) for clusters of many different sizes and shapes. Two regimes are readily identifiable, above and below $NN = 2$.

particle displacements to include a rotational degree of freedom that is required for investigation of glasses composed of anisotropic particles. Finally, we developed a method to extract elastic properties of quasi-2D membranes from images of buckled membranes by extension of similar techniques previously employed for spherical membranes.

1.4.1 Rapid Quenching of Microgel Particle Liquids

In order to study aging, it is desirable to observe a glass starting from just after its formation. As noted in Section 1.2.1, previous methods of rejuvenating glass prevented observation for tens or hundreds of seconds after the glass is formed. In order to observe aging at the earliest times, we developed a method to rapidly quench from liquid to glass through a new experimental twist utilizing optical heating. A small amount of red dye, is released into the suspension. This dye absorbs light from a mercury lamp focused through the microscope objective. The sample field of view lies at the center of the illumination region. There, the temperature is increased by $\sim$4 degrees in $\sim$0.1 seconds via light absorption and molecular relaxation processes. The NIPA particle radii are thus abruptly decreased by $\sim$0.1 μm, and the local area fraction (ϕ_A) is decreased by $\sim 10\%$. While the lamp is on, the particles are in the liquid state. The Brownian time of micron sized particles is $\sim$1 second, and the lamp is only on for $\sim$6 seconds, so thermophoretic effects are avoided. However, everything else (e.g., the rest of the sample, the microscope, etc.) is held at the original low temperature; thus when the mercury lamp is turned off, the excess heat rapidly dissipates, and particles swell to their original size in less than 0.1 seconds. The rapid change from small-ϕ_A (liquid) to large-ϕ_A creates a glass. Aging begins (t_w = 0 seconds) once the sample returns to thermal equilibrium and particles have completely returned to their original size. Thus, this technique enables us to begin watching a glass age immediately after it

is formed.

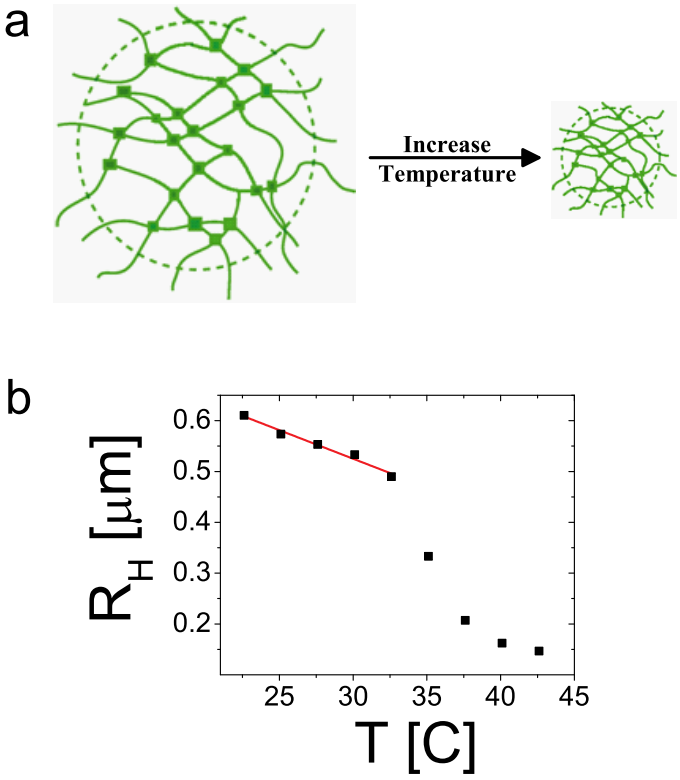

Figure 1.11: a. PNIPAM particles are depicted in cartoon form. When temperature is increased, PNIPAM particles decrease their diameters. b. Hydrodynamic radius, R_H of PNIPAM particles as a function of T.

1.4.2 Measurement of Phonon Modes for Anisotropic Particles

As introduced in Section 1.2.3, we measured the vibrational properties of ellipsoidal glasses. Previously, we were among the first researchers to apply displacement correlation matrix methods to translational degrees of freedom [23, 57, 58, 90]. Those methods work well for suspensions of spheres. However, for anisotropic particles, rotations are important and must be taken into account. We extracted vibrational properties of ellipsoidal glasses by measuring rotational and translational displacement correlations. To do so, we extended the procedure for spheres

([24]) to incorporate a rotational degree of freedom. Following [18], we expect undamped hard particles that repel entropically near but below the jamming transition to give rise to solidlike vibrational behavior on time scales long compared to the collision time but short compared to the time between particle rearrangement events [57, 58]. Thus, the stiffness matrix arising from entropic repulsions is directly related to the dynamical matrix characterizing vibrations. By performing this analysis, we found that the vibrational properties of glasses are highly dependent on particle shape.

1.4.3 Theory of Buckled Quasi-2D Membranes

By analyzing the shape of a buckled spherical membrane, information can be extracted about the membrane's elastic properties [99]. However, far less work has been done on disc-shaped membranes, as introduced in in Section 1.1. To understand the elastic properties of the membrane that forms when a drop is evaporated in confinement (i.e., the elastic properties of the CMMs), we extended analytical descriptions of elastic membranes to our quasi-2D geometry wherein observations about bending and buckling geometry are unambiguous. Following [99], we describe the stretching and bending energy associated with membrane buckling events. The deformation energy is located within the deflected rim. Membranes buckle in such a way as to minimize their energy, so we then minimize the total buckling energy with respect to the rim size. As a result of minimizing the total bending and stretching energy, $\kappa/E = d^4/(3r^2)$, where κ is the membrane bending rigidity, E is the Young's modulus, d is the rim width, and r is the drop radius. Thus, by measuring d and r, we can experimentally determine κ/E.

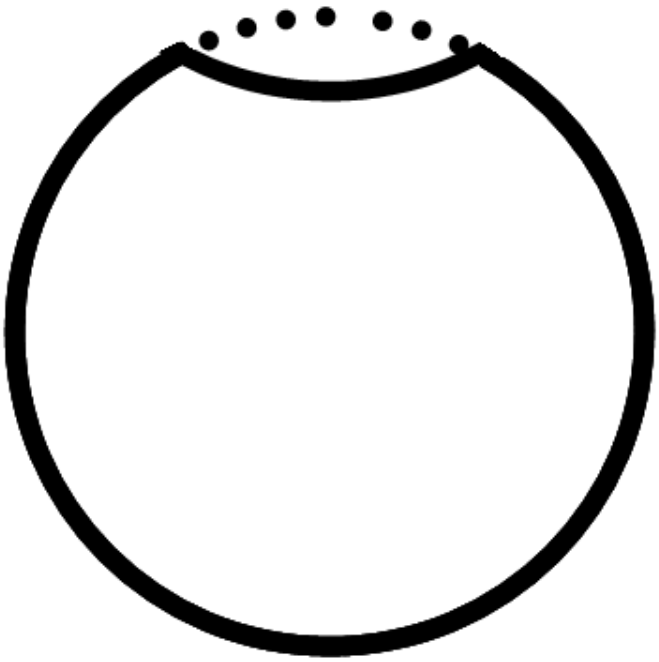

Figure 1.12: Cartoon representation of a buckling event. The dotted line represents the initial membrane configuration (before the buckling event).

1.5 Organization

The content of this thesis is organized as follows. We first discuss our investigation of particle behavior in evaporating drops and the coffee-ring effect (Chapter 2). This work was published [186]. We demonstrate that particle shape strongly affects the deposition of particles during evaporation. Next, we investigate the role of particle shape in evaporating drops in confined geometries, and show how to extract the bending rigidity of the membranes formed by particles adsorbed on the air-water interface (Chapter 3). This work is published [185]. We then shift to experiments investigating the behavior of glasses and related transitions. We first discuss experiments that use optical heating to quench a liquid to a glass; this scheme permits the detailed study of aging in glasses (Chapter 4). This work is published [181]. Then, we report

the mechanisms by which crystals transform into glasses as the amount of quenched disorder increases (Chapter 5). This work is published [182]. In Chapter 6 we investigate the effect of particle shape on the vibrational modes in glasses composed of ellipsoidal particles. This work is published [183]. Next, we investigate the effect of particle number and network connectivity on the vibrational modes in disordered clusters, allowing is to identify when small clusters start to behave like bulk glasses (Chapter 7). This work is published in [184]. Finally, in Chapter 8 we summarize the work presented in this dissertation, and suggest future directions for the investigation of nonequilibrium colloids.

Chapter 2

Coffee Ring Effect Undone by Shape Dependent Capillary Interactions

2.1 Introduction

When a drop of liquid dries on a solid surface, its solute is deposited in ring-like fashion. This phenomenon, known as the coffee ring effect [37, 40, 76], is familiar to anyone who has dried a drop of coffee. During the drying process, drop edges become pinned, and capillary flow outward from drop center brings suspended particles to the edge as evaporation proceeds. After evaporation, suspended particles are left highly concentrated along the original drop edge. The coffee ring effect is manifest in systems with diverse constituents ranging from large colloids [36–38] to nanoparticles [15] to individual molecules [89]. In fact, notwithstanding the many practical applications for uniform coatings in printing [128], biology [46,47], and complex assembly [39], the ubiquitous nature of the effect has proven difficult to avoid [15, 77, 83, 124, 126, 171]. Here

we experimentally show that suspended particle *shape* matters for coatings and can be used to eliminate the coffee ring effect. Ellipsoidal particles deposit uniformly during evaporation. The anisotropic particles significantly deform interfaces, producing strong interparticle capillary interactions [16, 19, 105, 106, 111, 112, 127]. Thus, after the ellipsoids are carried to the air-water interface by the same outward flow that causes the coffee ring effect for spheres, strong long-ranged interfacial attractions towards other ellipsoids lead to the formation of loosely-packed quasi-static or arrested structures on the air-water interface [54, 105, 106, 111]. These structures prevent the suspended particles from reaching the drop edge and ensure uniform deposition. Interestingly, under appropriate conditions, suspensions of spheres mixed with a small number of ellipsoids also produce uniform deposition.

A drop of evaporating water is a complex, difficult-to-control, non-equilibrium system. Along with capillary flow, the evaporating drop features a spherical-cap-shaped air-water interface and Marangoni flows induced by small temperature differences between the top of the drop and the contact line [38]. Attempts to reverse or ameliorate the coffee ring effect have thus far focused on manipulating capillary flows [15, 77, 83, 124, 126, 171]. In this contribution we show that uniform coatings during drying can be obtained simply by changing particle *shape*. The uniform deposition of ellipsoids after evaporation (Fig. 2.1 a) is readily apparent, and it stands in stark contrast to the uneven "coffee ring" deposition of spheres (Fig. 2.1 b) in the same solvent, with the same chemical composition, and experiencing the same capillary flows (Fig. 2.1 c).

A landmark paper by Deegan, *et al.*, captured all of the qualitative theoretical features of the coffee-ring effect. Essentially, the edges of evaporating drops easily become pinned, and cannot

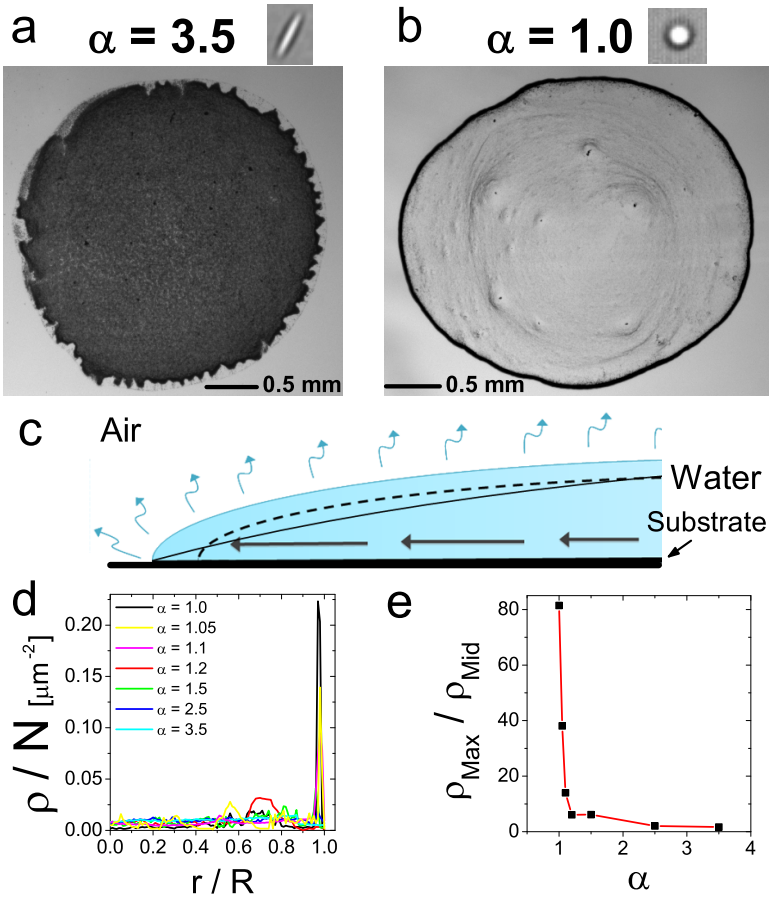

Figure 2.1: a. Image of the final distribution of ellipsoids after evaporation. b. Image of the final distribution of spheres after evaporation. c. Schematic diagram of the evaporation process depicting capillary flow induced by pinned edges. If the contact line were free to recede, the drop profile would be preserved during evaporation (dashed line). However, the contact line remains pinned, and the contact angle decreases during evaporation (solid line). Thus, a capillary flow is induced, flowing from the center of the drop to its edges; this flow replenishes fluid at the contact line. d. Droplet-normalized particle number density, ρ/N, plotted as function of radial distance from center of drop for ellipsoids with various major-minor axis aspect ratios. e. The maximum local density, ρ_{Max}, normalized by the density in the middle of the drop, ρ_{Mid}, is plotted for all α. Red lines guide the eye.

recede, i.e., the drop diameter cannot decrease Fig. 2.2. As the edge of the drop is thinner than the middle of the drop, fluid must flow from the middle of the drop to the edge of the drop to replenish the water that has evaporated away. In other words, the water lost due to evaporation, quantified by the evaporative flux, J, must be canceled by water gained via a flow of fluid, with flow velocity v. In a square shaped area with length l and height h, Jl^2 must be equal to vlh. To first order, $J \propto v$ (Fig. 2). By solving the diffusion equation, it can be shown that J diverges as the edge is approached as $J \propto (R-r)^{\lambda}$, where $\lambda = (\pi - 2\theta_c)/(2\pi - 2\theta_c)$. Thus, $v \propto (R-r)^{\lambda}$. Additionally, since the drop height, h, decreases approximately linearly over time, as $h \propto (t_f - t)$. However, the outward flow must cancel the evaporative flux at all times, so $v \propto (t_f - t)$. Thus, simply be pinning the edges of a drop, a complex radially outward flow is induced.

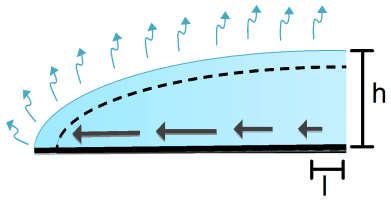

Figure 2.2: Schematic diagram of the evaporation process depicting capillary flow induced by pinned edges. If the contact line were free to recede, the drop profile would be preserved during evaporation (dashed line). However, the contact line remains pinned, and the contact angle decreases during evaporation (solid line). Thus, a capillary flow is induced, flowing from the center of the drop to its edges; this flow replenishes fluid at the contact line.

2.2 Method and Materials

Much of the physics of the coffee ring effect has been demonstrated with micron-sized polystyrene particles [37]. Here we also utilize such polystyrene particles and simply modify their *shape*.

Our experiments employ water drops containing a suspension of micron-sized polystyrene spheres (Invitrogen) stretched asymmetrically to different aspect ratios [21, 72]. We evaporate the drops on glass slides (Fisher Scientific) and study suspensions containing particles of the same composition, but with different major-minor diameter aspect ratio (α), including spheres ($\alpha = 1.0$), slightly deformed spheres ($\alpha = 1.05, 1.1, 1.2, 1.5$), and ellipsoids ($\alpha = 2.5, 3.5$); we study volume fractions (ϕ) that vary from $\phi = 10^{-4}$ to 0.2.

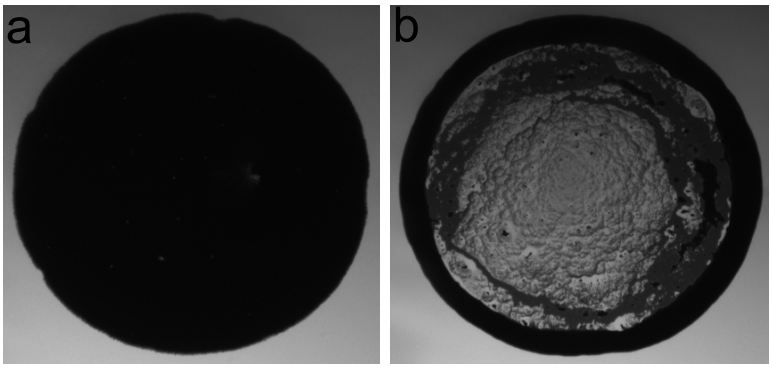

Figure 2.3: a. The final distribution of ellipsoids, evaporated from a suspension with initial volume fraction $\phi = 0.20$. b. The final distribution of spheres, evaporated from a suspension with initial volume fraction $\phi = 0.20$.

To create ellipsoidal particles, 1.3 μm diameter polystyrene particles are suspended in a polyvinyl alcohol (PVA) gel and are heated above the polystyrene melting point ($\sim$100 °C), but below the PVA melting point ($\sim$180 °C) [21, 72]. Polystyrene melts in the process, but the PVA gel only softens. The PVA gel is then pulled so that the spherical cavities containing liquid polystyrene are stretched into ellipsoidal cavities. When the PVA gel cools, polystyrene solidifies in the distorted cavities and becomes frozen into an ellipsoidal shape. The hardened gel dissolves in water, and the PVA is removed via centrifugation. Each sample is centrifuged and washed with water at least 10 times. We performed a separate set of experiments investigating the effects PVA has on evaporating drops, in order to ensure the PVA was not affecting our

results. In these experiments, we carefully controlled the PVA weight percent. We found that if a sample contains more than 0.5% PVA by weight, then the contact line depins very quickly after the drop is placed on a glass slide. However, in samples with less than 0.5% PVA by weight, the contact line behavior is identical to the contact line behavior in drops without PVA. To confirm that small amounts of PVA do not affect the deposition of spheres, we added PVA (0.45% by weight) to a suspension of spheres. During evaporation, the contact line remains pinned, and the spheres exhibit the coffee ring effect. Further, when ellipsoids are diluted by a factor of 100, and thus the PVA weight percent is decreased by a factor of 100 (to an absolute maximum of 0.05%), the deposition of the spatially uniform deposition of ellipsoids persists. Each iteration of this process creates $\sim 10^9$ ellipsoidal particles in ~ 50 μl suspensions. The particles are charge-stabilized, and the resultant suspensions are surfactant-free. Snapshots of experimental particles are shown in the insets of Fig. 2.1 a, b. The aspect ratio polydispersity is $\sim 10\%$. To ensure the preparation process does not affect particle deposition, our spheres undergo the same procedure, absent stretching.

2.3 Capillary Interactions

While spheres and ellipsoids behave similarly in bulk fluid (at small packing fractions, far from any crystalline phases), their behavior is dramatically different on the air-water interface. Specifically, anisotropic particles significantly deform interfaces, producing strong interparticle capillary interactions [16, 19, 105, 106, 111, 112, 127]. These deformations can be understood from expanded solutions of the Young-Laplace equation. Briefly, the Young-Laplace equation states $\Delta h = p_{air} - p_{water}$, where Δ is the Laplacian, h is the height of the air-water interface, p_{air}

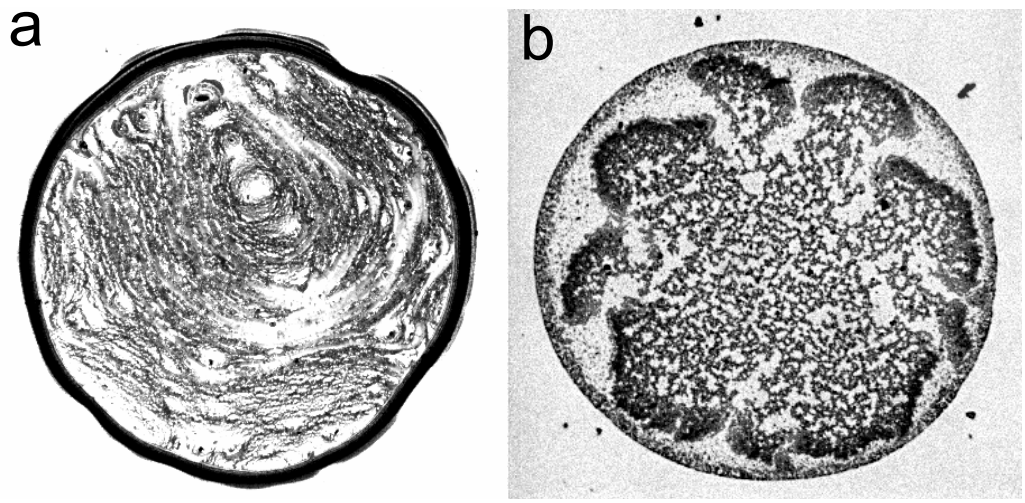

Figure 2.4: a. The final distribution of core-shell polystyrene-PNIPMAM spheres. These hydrophilic particles exhibit the coffee ring effect. b. The final distribution of core-shell polystyrene-PNIPMAM ellipsoids. These particles, which are both anisotropic and hydrophilic do not exhibit the coffee ring effect.

is the pressure in the air, and p_{water} is the pressure in the water [155]. Gravitational effects can be ignored for micron-sized polystyrene particles in water, so the pressure change over the interface is 0. For polar coordinates, $\Delta h(r,\phi) = (r^{-1}\partial_r r\partial_r + r^{-2}\partial_\phi^2)h(r,\phi) = 0$. This problem is remarkably similar to electrostatics, and can be solved through separation of variables, i.e., with the ansatz $h(r,\phi) = R(r)\Phi(\phi)$. This leads to $(r^{-1}\partial_r r\partial_r R(r))\Phi(\phi) + (r^{-2}\partial_\phi^2\Phi(\phi))R(r)) = 0$. Since this equation must hold as r and ϕ are varied independently, each term in the equation must the same constant, leadingly termed m^2. Thus, $\partial_\phi^2\Phi(\phi) = m^2\Phi(\phi)$ and $r\partial_r r\partial_r R(r) = m^2 R(r)$, which are solved by $\Phi = A_m cos(m(\phi - B_m))$ and $R = C_m r^{-m}$. The height at the edge of the particle is then $h(r,\phi) = \sum_{m=0}^{\infty} D_m cos(m(\phi - B_m))$. The monopole term $m = 0$ corresponds to the height of the interface being uniformly lowered (raised). Thus, it could be relaxed by simply raising (lowering) the particle. The monopole term is only stable in an external field (e.g., gravity); since there are no external forces pulling on the particles, this term must be 0.

The dipole term $m = 1$ corresponds to the height of the interface being lowered on one side, and raised on the opposite side. Thus, it could be relaxed by simply rotating the particle, i.e., lowering the high side and raising the low side. The dipole term is only stable when an external torque is applied; since there are no external torques acting on the particles, this term must be 0. Therefore, the lowest allowed term is the quadrupole term ($m = 2$), i.e., $h(r, \phi) \propto cos(2(\phi - B_2))A_2 r^{-2}$.

The above derivation never mentioned anisotropic boundary condition. In fact, the quadruploar form for $h(r, \phi)$ is applicable in general to any deformation of the air-water interface (absent external forces and torques). Instead of particle shape, the air-water interface can be deformed if the three-phase contact line is heterogeneously pinned on a sphere (see Fig. 2.5). This also produces a quadrupolar profile of the interfacial height. However, the linear size of deformation from contact-line-roughness is typically smaller than the linear size of deformation from shape-based-roughness (for example, see reference [127]).

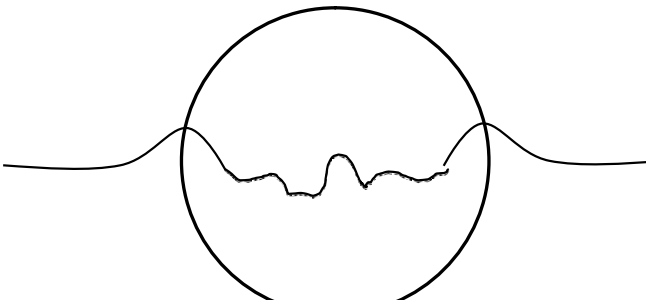

Figure 2.5: Cartoon of a heterogeneously pinned three-phase contact line on a sphere. This contact-line-roughness deforms the air-water interface with a quadrupolar symmetry, similar to the shape-based deformations characteristic of ellipsoids.

2.4 Evaporation of Colloidal Suspensions

During the drying process, the droplet contact line remains pinned in all suspensions, and fluid (carrying particles) flows outward from drop center to replenish the edges. Spherical particles are efficiently transported to the edge, either in the bulk or along the air-water interface, leaving a ring after evaporation is complete. Anisotropic particles ($\alpha > 1.0$), however, are only transported toward the edge until they reach the air-water interface. Once at the air-water interface, ellipsoids experience strong long-ranged attractions to other ellipsoids [16, 19, 105, 106, 111, 112], leading to the formation of loosely-packed quasi-static or arrested structures at the interface [54]. The interparticle attraction between ellipsoids on the interface is more than two orders of magnitude stronger than the attraction between spheres on the interface [127]. Thus, anisotropic particles in these "open" structures are strongly bound to each other and to the interface, so the energy cost of deforming, moving, or breaking up these clusters is very large. As a result, ellipsoid mobility is markedly reduced, and they resist the radially outward flow. Finally, during the last stages of evaporation, surface flows [77] are observed to carry ellipsoids on the air-water interface from the drop edges back towards the drop center. This process often leaves a region near the contact line mostly void (see experimental snapshots Fig. 2.6 g and h). The voided region decreases as ϕ increases (the aforementioned bump in $\rho(r)$ for $\alpha = 1.2$ is located at the edge of this voided region). Thus, when evaporation is complete, anisotropic particles are much more uniformly deposited on the glass surface than spheres. While spheres also adsorb onto the interface during evaporation, they do not significantly deform the interface [106]. Therefore, the radially outward fluid flow continues to push them to the drop's edge [38]. Fig. 2.1 shows the final deposition, after evaporation on glass slides at 23 °C, of two particle suspensions ($\phi = 0.005$, 1 μl) with

different aspect ratios. Spherical particles are primarily deposited at the original perimeter of the droplet (Fig. 2.1 b). Ellipsoidal particles are distributed much more uniformly (Fig. 2.1 a).

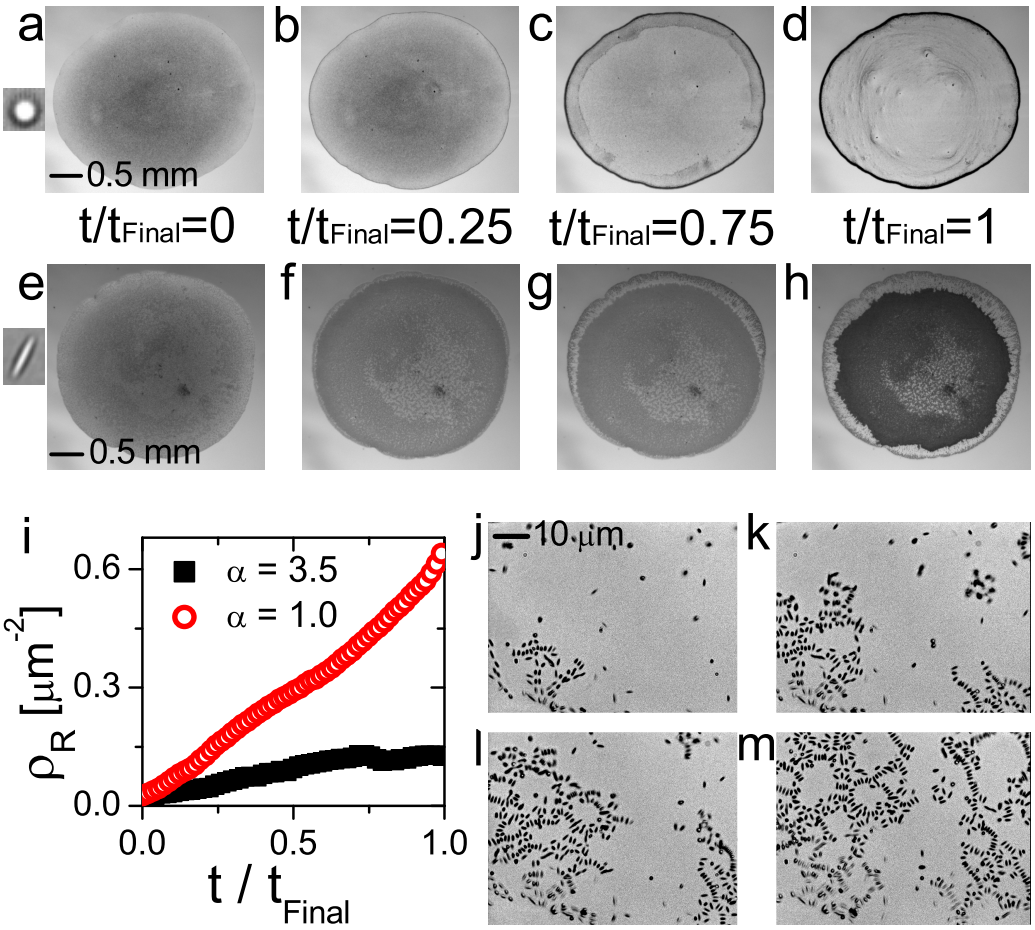

Figure 2.6: a-d. Experimental snapshots at different times during the evaporation of a drop of spheres. e-h. Experimental snapshots at different times during the evaporation of a drop of ellipsoids with aspect ratio $\alpha = 3.5$. i. The areal particle density, ρ_R, located within 20 μm of the contact line (i.e., drop edge) as a function of time during evaporation. j-m. Images of the assembly of ellipsoids at the air-water interface over the same time intervals during evaporation. Loosely-packed structures form on the air-water interface, preventing ellipsoids from reaching the drop edge. The three phase contact line can be seen in the bottom left corner of these snapshots.

2.4.1 Characterization of Particle Deposition

To quantify the behavior shown qualitatively in Fig. 2.1 a and b, we determined the areal number fraction of particles deposited as a function of radial distance from the drop center (Fig. 2.1 d). Specifically, image analysis enables counting of the number of particles, N_r, in an area set by the annulus bounded by radial distances r and $r + \delta r$ from the original drop center [37, 38]; here δr is $\sim$8 μm. The areal particle density $\rho(r) = N_r/A$, with $A = \pi((r + \delta r)^2 - r^2)$. To further eliminate small sample-to-sample particle density differences, we normalize ρ by the total number of particles in the drop, N, and thereby report $\rho(r)/N$ as a function of r/R, where R is the drop radius. Dilute suspensions ($\phi = 0.005$) are utilized to improve image quantification. For spheres ($\alpha = 1.0$), ρ/N is $\sim$70 times larger at $r/R \approx 1$ than in the middle of the drop. Conversely, the density profile of ellipsoidal particles is fairly uniform as a function of r/R, though there is a slight increase at large r/R. As aspect ratio is increased in between these extremes, the peak at large r/R decreases. Specifically, a clear coffee ring effect persists for particles only marginally distorted from their original spherical shape ($\alpha = 1.05$ and 1.1), but particles that are slightly more anisotropic ($\alpha = 1.2$) are deposited uniformly.

To further quantify the peaked deposition of spheres and the more uniform deposition of ellipsoids, we calculate and plot ρ_{MAX}/ρ_{MID} (Fig. 2.1 e), where ρ_{MAX} is the maximum value of ρ (typically located at $r/R \approx 1$) and ρ_{MID} is the average value of ρ in the middle of the drop ($r/R < 0.25$). For spheres, $\rho_{MAX}/\rho_{MID} \approx 70$. As aspect ratio increases slightly ($\alpha = 1.05$ and 1.1) ρ_{MAX}/ρ_{MID} decreases to $\sim$ 38 and 13, respectively. For ellipsoids, ρ_{MAX}/ρ_{MID} is more than ten times smaller. A second, relatively small aspect-ratio deposition effect is also observed for the ellipsoids; as α increases above 1.2, ρ_{MAX}/ρ_{MID} decreases slightly. Note,

the value of ρ_{MAX}/ρ_{MID} was observed to be largely independent of initial volume fraction, i.e., ρ_{MAX}/ρ_{MID} fluctuated by approximately $\pm 10\%$ as volume fraction changed between $\phi = 10^{-4}$ and 0.2.

When the volume fraction is large enough, the drop surface should become saturated with particles, such that the remaining particles in the bulk are transported to the drop edge. However, at high volume fractions it becomes difficult to quantify the local particle density. Thus, while the particles that cannot attach to the interface are likely transported to the drop edge, it is difficult to demonstrate that this occurs. We evaporated a drop of ellipsoids ($\alpha = 3.5$) suspended at volume fraction $\phi = 0.20$. An experimental snapshot after evaporation is complete demonstrates that overall the coffee ring effect is destroyed, but the local density cannot be extracted (Fig. 2.3). An image of the final distribution of spheres evaporated from a suspension with initial packing fraction $\phi = 0.20$ is included for comparison.

2.4.2 Characterization of Evaporation Process

Quantification of the spatio-temporal evaporation profile of the suspensions provides a first step towards understanding why ellipsoids are deposited uniformly. To this end, we measure drop mass of different suspensions (20 μl in volume, 6.0 mm in radius, $\phi = 0.005$), during evaporation (Fig. 2.7). (Note, large-volume drops are utilized in this experiment to improve the accuracy of the evaporation rate measurement.) The drop mass decreases linearly in time, and the mass rate-of-change of 10.0 μg/s is the same for drops of sphere suspension, drops of ellipsoid suspension, and for drops of water absent colloid. The evaporation behavior is also consistent with steady-state vapour-diffusion-limited evaporation of a spherical-cap-shaped drop with a pinned contact line [36, 37].

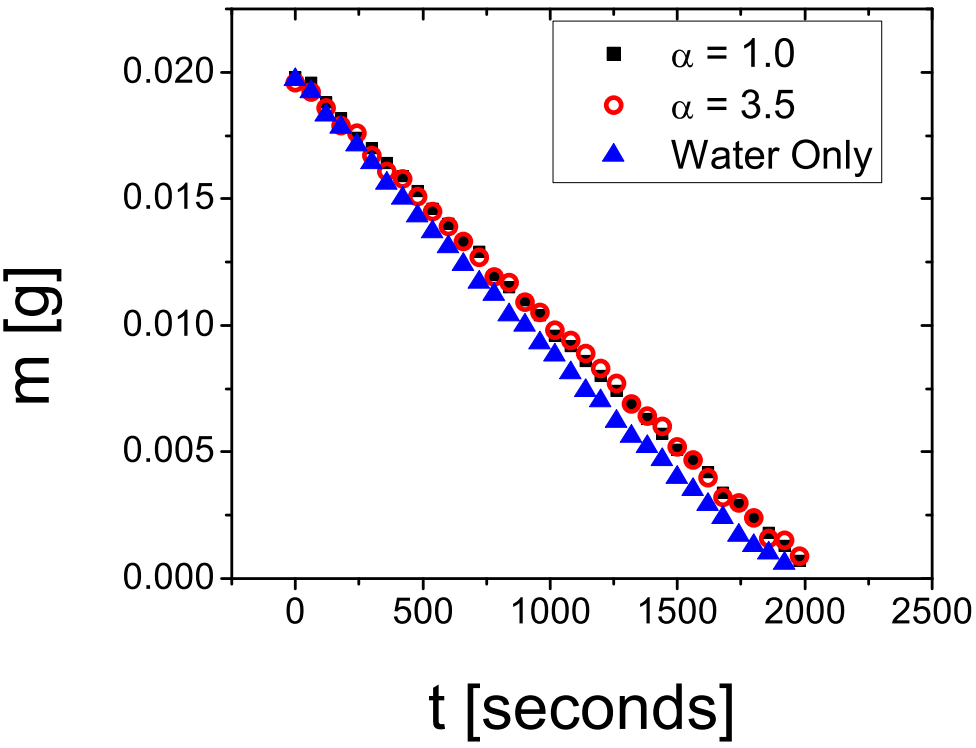

Figure 2.7: The mass, m, of drops of different suspensions is plotted versus time, t, for evaporating drops. Suspensions of spheres ($\alpha = 1.0$ black squares) and ellipsoids ($\alpha = 3.5$ open red circles) are shown, as well as a drop of water absent colloids (blue triangles).

To confirm that the contact line remains pinned until the final stage of evaporation, we measured the radius of the 1 μl drops ($\phi = 0.005$) during evaporation by video microscopy (Fig. 2.8). Using this data, the time at which evaporation finishes, t_{Final}, is readily identified as the time when the drop radius shrinks to zero. Interestingly, we find the radius decreases by less than 10% until $t = 0.8 \cdot t_{Final}$; i.e., the contact line is pinned for the vast majority of the evaporation time period in all samples. For suspensions of ellipsoids, the contact line becomes partially depinned around $t = 0.7 \cdot t_{Final}$, but does not become completely depinned until $t = 0.8 \cdot t_{Final}$. The experiments thus demonstrate that despite similar contact line behavior, capillary flow, and

evaporation rates, the deposition of spheres and ellipsoids differs significantly.

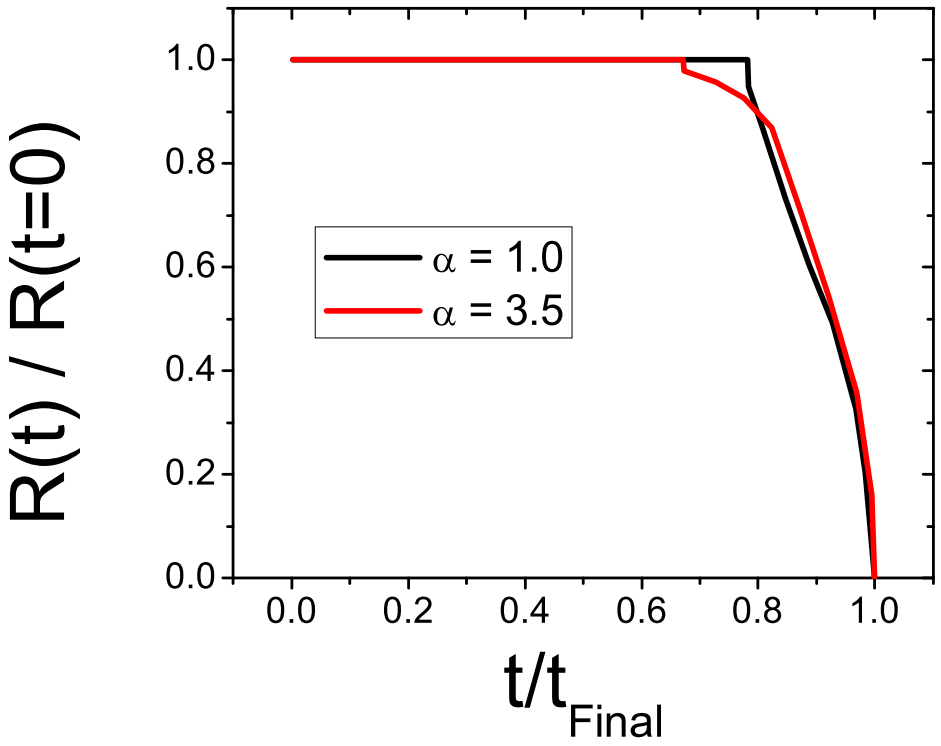

Figure 2.8: The radius, R, of drops of different suspensions is plotted versus time, t, for evaporating drops. Suspensions of spheres ($\alpha = 1.0$ black line) and ellipsoids ($\alpha = 3.5$ red line) are shown. To facilitate comparisons, the time is normalized by the time evaporation ends (t_{Final}), and R is normalized by the value of R at $t = 0$ s.

Experimental image snapshots clearly reveal that while spheres are carried to the drop's edges (Fig. 2.6 a-d), ellipsoids are carried there to far lesser degree (Fig. 2.6 e-h). We measured the average areal particle density close to the contact line, $\rho_R = \int_{r=R-20\mu m}^{r=R} \rho(r)dr$ as a function of time (Fig. 2.6 i), and thereby demonstrated that ellipsoid density grows at a slower rate than sphere density. For spheres, ρ_R increases linearly until evaporation is complete, with a slope of 0.54 s^{-1}. The areal density of ellipsoids near the contact line, however, stops growing at $t/t_{Final} = 0.75$; for $t/t_{Final} < 0.75$, ρ_R increases with a slope of 0.15 s^{-1}, less than $1/3$ the

slope for spheres despite similar evaporation rates, capillary flows, and contact line behaviors.

2.4.3 Particle Behavior during Evaporation

Images of particles near the drop's contact line (Fig. 2.6 j-m) reveal that unlike spheres, which are carried from the bulk all the way to the contact line (Fig. 2.9 a-c), most ellipsoids adhere to the loosely-packed structures at the air-water interface before they reach the contact line (Fig. 2.9 d-f). This capillary attraction has been characterized in prior experiments as long-ranged and very strong [32,101,103,105,106,127]. The loosely-packed configurations formed by ellipsoids on the interface are, in fact, structurally similar to those seen in previous experiments of ellipsoids at flat air-water and water-oil interfaces [105, 106, 111]. They produce a surface viscosity that is much larger than the bulk viscosity, facilitating ellipsoid resistance to radially outward flows. Note, spheres also adsorb onto the interface during evaporation. However, spheres do not strongly deform the interface [106] and they experience a much weaker interparticle attraction than ellipsoids [127]; thus, radially outward fluid flows push spheres to the drop's edge [38].

In order to quantify the ability of interfacial aggregates of ellipsoids to resist bulk flow, we calculated the Boussinesq Number for ellipsoids with $\alpha = 3.5$. The Boussinesq number, B_0, is the ratio of the surface drag to the bulk drag: $B_0 = \frac{G'}{\tau L}$ where τ is shear stress from bulk flow, G' is the elastic modulus of the interfacial layer, and L is the probed lengthscale [157]. B_0 will vary spatially with the local number of ellipsoids on the air-water interface, so we focus here on a region within 40 μm of the contact line. We first calculated B_0 at an early time ($t = 0.1\ t_F$). The shear stress, calculated from the particle velocity and drop height is $\tau \approx 3 \cdot 10^{-4}$ Pa. About 40% of the surface is covered with ellipsoids. Using the surface coverage area fraction, we obtained the modulus of the interfacial monolayer (G' $\approx 10^{\cdot -3}$ N/m)

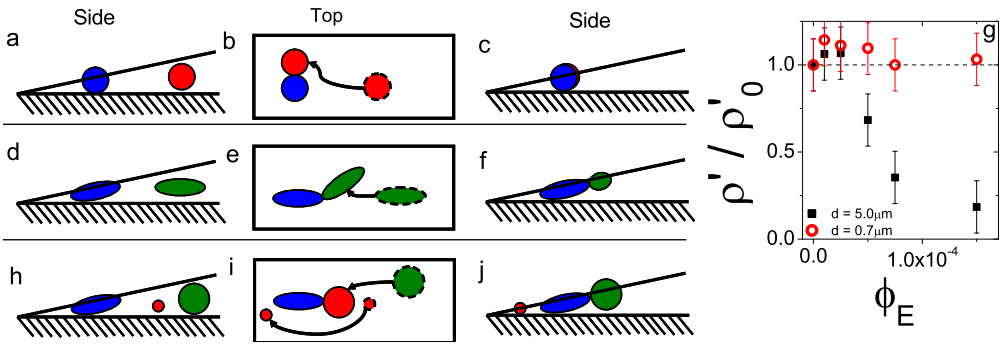

Figure 2.9: For all cartoons, the left panel is a side view at an early time, the right panel is a side view at a later time, and the center panel is a top view showing particle trajectories in between those times. a-c. Cartoon depicting capillary flow that carries spheres to the drop's edge. Spheres leave a ring-like formation after evaporation. d-f. Cartoon depicting capillary flow that carries ellipsoids to drop's surface. Ellipsoids become attached to the air-water interface, where they form loosely-packed structures. These effects erase the coffee ring effect; the final deposit of ellipsoids is uniform. g. The deposition of mixtures of spheres and ellipsoids are characterized by the ratio $\rho' = \rho_{Max}/\rho_{Mid}$, where ρ_{Max} is the maximum local density and ρ_{Mid} is the density in the middle of the drop, as a function of ellipsoid volume fraction, ϕ_E. Two sizes of particles are studied: $d = 5.0$ μm (black squares), $d = 0.7$ μm (red circles), where d is the particle diameter. To best capture the evolution of the deposition as ϕ_E increases, ρ' is normalized by ρ'_0, the value of ρ' when there are no ellipsoids present, i.e., $\phi_E = 0$. The coffee ring effect persists for mixtures of small spheres and ellipsoids, but the coffee ring is destroyed for mixtures of large spheres and ellipsoids. Error bars represent the statistical uncertainty that results from finite bin sizes. h-j. Cartoon depicting capillary flow that carries suspensions of spheres and ellipsoids to the drop's edge. Spheres that are smaller than the ellipsoid continue to travel all the way to the edge, and exhibit the coffee ring effect. Spheres larger than the ellipsoids are affected by deformations of the air-water interface, and join the ellipsoids in loosely packed structures forming at the interface.

from previous experimental studies [111]. The probed lengthscale, L, is at most 0.01 m. Thus, at t $= 0.1$t$_F$, B$_0 \sim 300$. This calculation is performed at different times during evaporation, until the aggregate of ellipsoids begins flowing towards the drop center (Fig. 2.10). The Boussinesq number grows exponentially with time: B$_0 \propto exp(\frac{t}{0.12t_F})$. This is expected as τ grows linearly with particle velocity, which increases by a factor of $\sim$ 2 during evaporation. However, G' grows exponentially with the ellipsoidal area fraction [111], and area fraction increases by a factor of ~ 3. Thus, the exponential growth of G' dominates this calculation. Finally, note that for spheres, B$_0 < 1$.

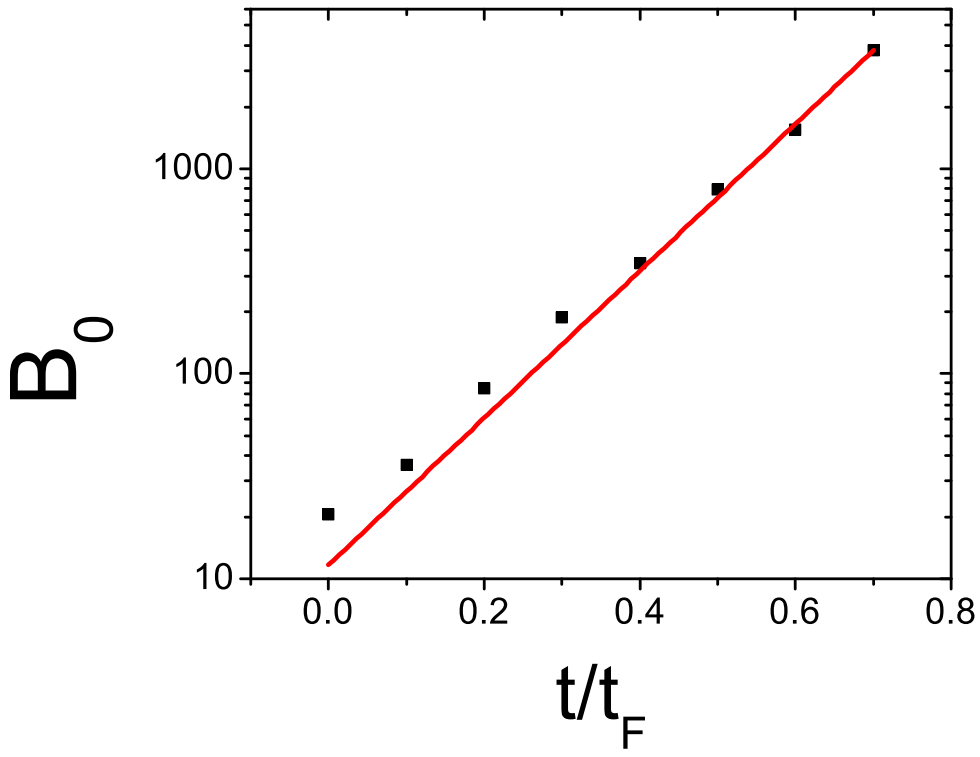

Figure 2.10: The Boussinesq number, B$_0$, for ellipsoids with $\alpha = 3.5$ is plotted versus time, t, normalized by the time evaporation finishes, t$_F$. The red line is the best exponential fit.

Experimental snapshots of the region within 40 μm of the drop contact line confirm that

while spheres pack closely at the edge (Fig. 2.11 a), ellipsoids form loosely packed structures (Fig. 2.11 b), which prevent particles from reaching the contact line. Particles with $\alpha = 1.2$ and 1.5 pack at higher area fractions than ellipsoids with $\alpha > 1.5$, resulting in larger values of ρ_{MAX}/ρ_{MID} for $\alpha = 1.2$ and 1.5 and producing the small peak in $\rho(r)$ at $r/R = 0.7$ for $\alpha = 1.2$. The structures on the air-water interface appear to be locally arrested or "jammed" [54], i.e., particles do not rearrange. Once an ellipsoid joins a collective structure, its position relative to other ellipsoids changes by less than 20 nm (lower limit of our resolution), and the structure only rearranges when new particles become attached to the interface.

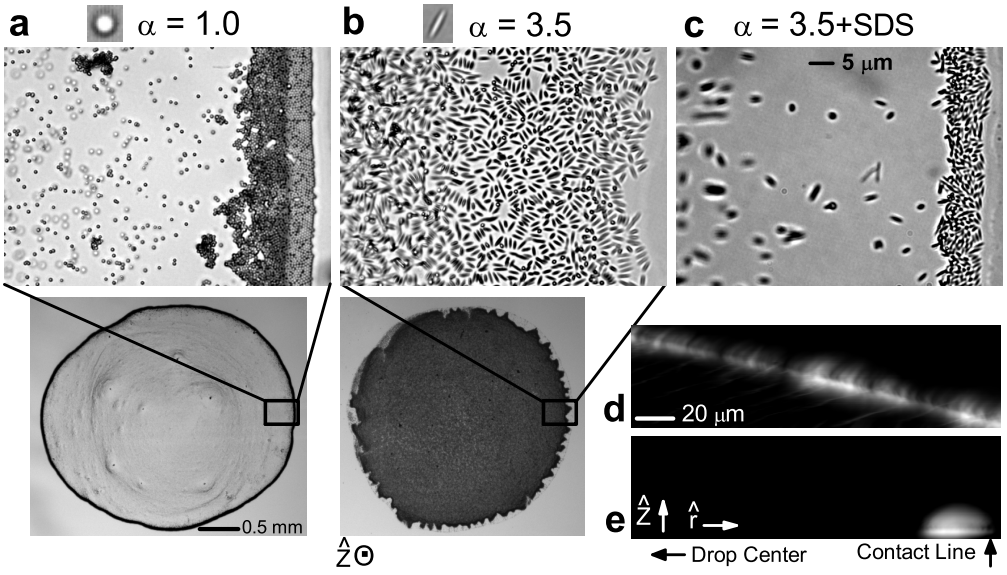

Figure 2.11: a-c. Images of a region within 40 μm of the drop contact line, taken at time $t/t_{Final} = 0.5$, for suspensions of spheres (a), suspensions of ellipsoids with $\alpha = 3.5$ (b), and ellipsoids with $\alpha = 3.5$ mixed with a surfactant (SDS) at 0.2% by weight. While spheres pack closely at the contact line, ellipsoids form loosely packed structures. Added surfactant lowers the surface tension of the drop, making ellipsoidal particles pack closely at the contact line, thus restoring the coffee ring effect. For a and b, pictures of the entire drop after evaporation are shown and the magnified region is indicated. d,e. Confocal projections of suspension of ellipsoids ($\alpha = 2.5$) and spheres (d and e, respectively) onto the z-r plane in cylindrical coordinates. While spheres are efficiently transported to the contact line, ellipsoids sit at the air-water interface.

To confirm that deformations of the interface are responsible for the uniform deposition of ellipsoids, we add a small amount of surfactant (sodium dodecyl sulfate, SDS, 0.2% by weight) to a suspension of ellipsoids with $\alpha = 3.5$. Surfactant lowers the surface tension of the drop, thus making interfacial deformations less energetically costly and shorter-range. This restores the coffee ring effect; ellipsoids pack closely at the contact line (Fig. 2.11 c), in a manner similar to spheres. The ellipsoids no longer strongly deform the air-water interface and their interactions with other ellipsoids are correspondingly reduced; as a result, they move more easily along and on-and-off the interface and are able to pack close to the contact line. (Note, surfactants can also induce surface flows and depin the contact line. The effect of surfactants in drying drops was explored in reference [156].) Further, ellipsoids increase the air-water surface tension, as evidenced by an increase in contact angle. The three-phase contact angle, θ_C, was measured by placing a large drop (~ 100 μl) on a glass slide. Then, a side-view picture was taken, allowing the contact angle to be measured (Fig. 2.12). Spheres do not modify the contact angle. However, as α increases, θ_C increases as well. Specifically, θ_C increases from $\sim 15^\circ$ for spheres to $\sim 35^\circ$ for ellipsoids with α=3.5 (Fig. 2.10).

We obtain direct evidence that the ellipsoids sit at the air-water interface, using three-dimensional confocal microscopy. Confocal snapshots are shown in Fig. 2.11 d and e. By integrating the brightness of each pixel over a period of 0.05 seconds, only particles that are roughly stationary during this time period appear in the images. Snapshots are then projected onto a side-view of the drop. The confocal snapshots clearly confirm that ellipsoids sit at the air-water interface (Fig. 2.11 d), while spheres do not and are carried all the way to the contact line (Fig. 2.11 e).

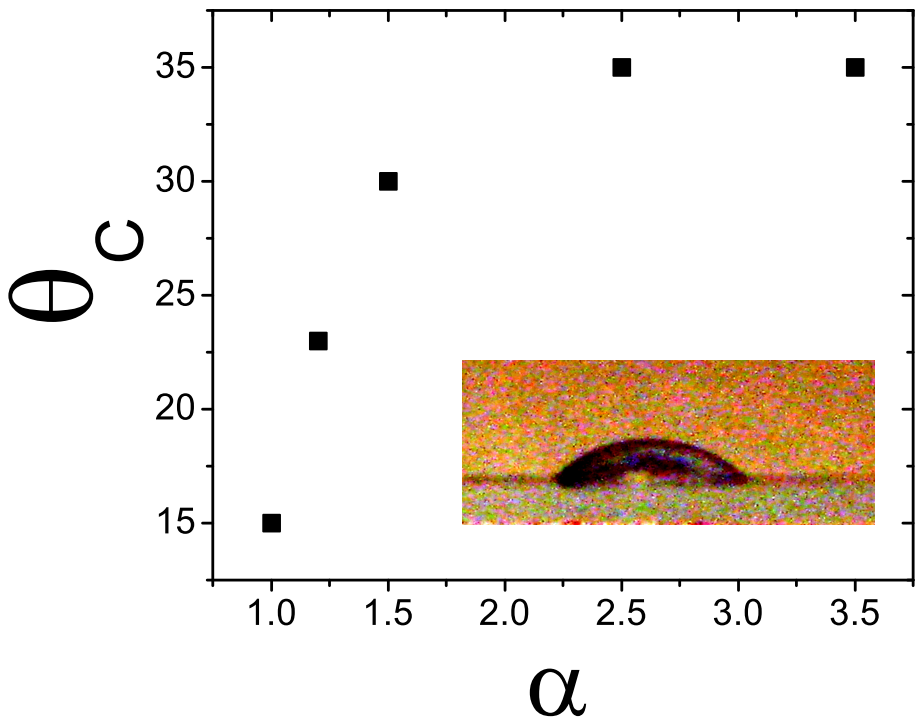

Figure 2.12: The three-phase contact angle, θ_C, is plotted versus aspect ratio, α. Inset: Image of a 100 μl drop of a suspension containing ellipsoids with $\alpha = 3.5$

2.4.4 Adsorption Position

To confirm that it is the behavior of ellipsoids at the drop's edge that produces the uniform deposition of ellipsoids we measured where ellipsoids adsorb on the air-water interface. Based on this, we were able to calculate the density of ellipsoids adsorbed on the air-water interface (ϕ), i.e., the number of ellipsoids on the air-water interface per unit area, versus radial distance (Fig. 2.13). The majority of particles are deposited at the drop's edge. In fact, $\sim 84\%$ of particles adsorb on the air-water interface near the drop's edge. This is consistent with previous experiments with spheres, which found that $\sim 10\%$ of spheres adsorb on the air-water interface in the middle of the drop [36, 38]. Thus, their behavior at the edge of the drop must be what produces the uniform deposition of ellipsoids.

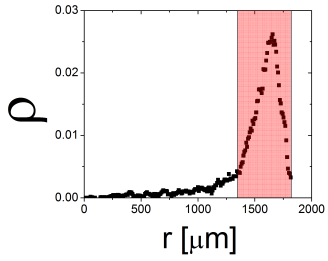

Figure 2.13: The density of adsorbed ellipsoids (ρ), i.e., the number of adsorbed ellipsoids per unit area, plotted versus radial position, r. The shaded region contains $\sim 84\%$ of adsorbed particles.

2.4.5 Single Particle Trajectories

To understand the different behaviors of spheres and ellipsoids at the edge of drying drops, it is instructive to observe some individual particle trajectories. First, the trajectory of a single sphere is highlighted in Fig. 2.14. When spheres reach the drop's edge, their progress is halted by a wall of spheres already at the drop's edge. Spheres then pack densely, and cannot rearrange as

they "jam" in a ring-shaped configuration. This is demonstrated quantitatively for a few typical spheres by plotting the distance between the sphere and the drop's edge (x) versus time (Fig. 2.14 e). Conversely, when ellipsoids reach the drop's edge, they pack loosely on the air-water interface (Fig. 2.15). Thus, ellipsoids already at the drop's edge do not necessarily halt the progress of ellipsoids that arrive at later times. This can be seen in Fig. 2.15 a-c, as an ellipsoid approaches the drop's edge (Fig. 2.15 a), passes underneath a cluster of ellipsoids on the air-water interface (Fig. 2.15 b), and eventually adsorbs on the air-water interface near the drop's edge (Fig. 2.15 c). As evaporation continues, ellipsoids can move along the surface of the drop towards the drop's center (Fig. 2.15 d). This is demonstrated quantitatively for a few typical ellipsoids by plotting x versus time (Fig. 2.15 e).

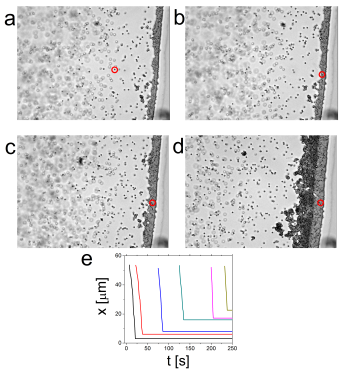

Figure 2.14: a-d. Images of a drop containing spheres during evaporation at four different times ($t = 1, 6, 26$ and 242 seconds). The same sphere is circled in each of the four images. e. The distance from the drop's edge (x) for six typical spheres is plotted versus t. Spheres reach the drop's edge, and quickly become "jammed," and cannot rearrange.

2.5 Final Distribution of Other Anisotropic Particles

We have now analyzed three additional types of anisotropic particles. First, we obtained suspensions of spherical and ellipsoidal polystyrene-PNIPMAM core-shell particles, i.e., polystyrene

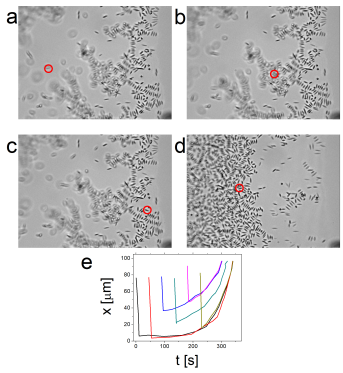

Figure 2.15: a-d. Images of a drop containing ellipsoids during evaporation at four different times ($t = 1, 10, 12$ and 622 seconds). The same sphere is circled in each of the four images. e. The distance from the drop's edge (x) for six typical spheres is plotted versus t. Spheres reach the drop's edge, and quickly become "jammed," and cannot rearrange.

particles coated with PNIPMAM. These suspensions were evaporated at 23 °C; at this temperature, PNIPMAM is hydrophilic. The core-shell spheres exhibit the coffee ring effect (Fig. 2.4(a)). Despite their hydrophilicity, the core-shell ellipsoids are deposited evenly. In fact, they form the same aggregates on the drop surface that polystyrene ellipsoids that are not coated with PNIPMAM do (Fig. 2.4(b)).

Further, we have evaporated suspensions of actin filaments and Pf1 viruses. In each of these suspensions, the contact line becomes depinned at very early times. To prevent this, we add a small amount of 50 nm diameter florescent polystyrene spheres ($\sim 1\%$ by weight), which pin the contact line until the final stage of evaporation ($t > 0.8\ t_F$), and thus exhibit the coffee ring effect. Both the actin filaments and Pf1 viruses are then deposited uniformly. Note, the mean major axis length for Pf1 viruses is ~ 2 μm and the mean major axis length for actin filaments is ~ 20 μm.

2.6 Mixtures of Spheres and Ellipsoids

Finally, we show that the addition of small numbers of ellipsoids to sphere suspensions can also destroy the coffee ring effect. If spheres are smaller than ellipsoids, then the coffee ring persists; if spheres are larger than the ellipsoid minor axis, then the coffee ring is destroyed. To observe this effect we evaporate drops of suspensions containing both ellipsoids and spheres.

Each suspension contains ellipsoids with $\alpha = 3.5$, stretched from particles of diameter $d = 1.3$ μm, and each suspension contains spheres suspended at a volume fraction $\phi = 0.02$. Evaporative deposits are characterized as a function of ellipsoid volume fraction ϕ_E via $\rho'(\phi_E) = \rho_{Max}/\rho_{Mid}$ (Fig. 2.9 g). First, we evaporate suspensions containing smaller spheres with $d = 0.7$ μm along with the ellipsoids at volume fractions ranging from $\phi_E = 0$ to 1.5×10^{-4}. After evaporation, the spheres displayed a clear coffee ring, and this coffee ring persists even if more ellipsoids are added to the initial suspension (Fig. 2.9 g). The coffee ring effect is uninhibited because spheres that are smaller than the ellipsoids are easily able to move under or through the loosely packed particle structures and reach the drop's edge (Fig. 2.9 h-j).

If, instead, we evaporate suspensions containing larger spheres with $d = 5.0$ μm, along with the same ellipsoids at the same volume fractions utilized previously, then different phenomena emerge. When the ellipsoid volume fraction is very small ($\phi_E \leq 2.5 \times 10^{-5}$), the suspensions still exhibit a clear coffee ring effect. However, at larger ϕ_E, the coffee ring is diminished, and it eventually disappears at sufficiently large ϕ_E, i.e., $\phi_E \approx 1.5 \times 10^{-4}$ (Fig. 2.9 g). In this case, the larger spheres adsorb onto the air-water interface farther from the drop edge than do the ellipsoids. In the absence of ellipsoids, the spherical particles form closely-packed aggregates, but in the presence of ellipsoids they instead join the loosely-packed aggregates, thus eliminating

the coffee ring effect (Fig. 2.9 h-j). Thus, uniform depositions can potentially be made with existing suspensions, simply by adding ellipsoids.

2.7 Future Directions

Looking forward, we note that the ability to deposit particles uniformly is desirable in many applications [128]. Unfortunately, most proposed methods for avoiding the coffee ring effect require long multistage processes, which can be costly in manufacturing or require use of organic solvents which are sometimes flammable and toxic (e.g. [15, 77]). Here we have shown that by exploiting a particle's shape, a uniform deposit can be easily derived from an evaporating aqueous solution. The results presented here further suggest that other methods of inducing strong capillary interactions, e.g., surface roughness [155], may also produce uniform deposits.

Additionally, open questions about the behavior of ellipsoids in drying drops persist. Specifically, one may have thought the drop's edge would quickly saturate with ellipsoids during evaporation. However, ellipsoids migrate towards the drop's center during evaporation, thus making room for more ellipsoids to adsorb on the air-water interface near the drop's edge. It is unclear why ellipsoids move towards the drop's center. It could be because of inward fluid flows along the drop's surface, or because it is energetically costly to deform the air-water interface close to the three-phase contact line. Experiments that measure the interaction between an isolated ellipsoid adsorbed on the air-water interface and the three-phase contact line could potentially help explain this phenomenon.

Chapter 3

Influence of particle shape on bending rigidity of colloidal monolayer membranes and particle deposition during droplet evaporation in confined geometries

3.1 Introduction

When colloidal particles adsorb onto air-water, oil-water, and other such interfaces, novel elastic membranes are created [111, 119, 141]. The mechanical properties of these colloidal monolayer membranes (CMMs) can depend on many factors including surface tension, capillary forces, and

particle size, shape, hydrophobicity, packing, and interaction potential. The resulting interface phenomenology is rich with physics that influences a wide range of applications from film drying to Pickering emulsion stabilization [112, 166, 186]. Nevertheless, full understanding of the elastic character of these membranes remains elusive. Recently, significant progress has been made towards measurement of the bulk, shear, and Young's moduli of CMMs, and towards an understanding of particle-induced interfacial mechanisms [9, 111, 119, 141, 165]. Many effects due to particle shape, for example, can be qualitatively explained by shape-dependent capillary interactions [16, 19, 80, 105, 106, 111, 112, 118, 155]; i.e., stiff membranes induced by ellipsoids at the air-water interface are more difficult to deform [111, 130, 162]. One mechanical property of CMMs that has not as yet been measured is bending rigidity. Bending rigidity is important, because the buckling behavior of membranes is controlled by the ratio of bending rigidity (κ) to Young's modulus (E) [99], and, as we shall show, the buckling behavior of membranes can substantially affect phenomena such as particle deposition during droplet evaporation. Unfortunately, such measurements are also difficult because constituent particle diameter is often similar to CMM deformation size [33].

In this contribution we report measurements of the bending rigidity of various colloidal monolayer membranes. We introduce a novel method for extracting bending properties of CMMs which employs evaporating drops in confined geometries and readily permits study of particle-shape effects. To this end, colloidal drops composed of particles with approximately

the same chemical composition, but with shapes ranging from spheres to ellipsoids, are confined between two glass plates and left to evaporate (Fig. 3.1 a). During evaporation, the air-water interface is observed to buckle in a manner similar to spherical-shell-shaped elastic membranes [34,102,131]. To extract membrane bending rigidity, we extend the analytic description of buckled spherical membranes to our quasi-two-dimensional geometry [99]. We find that CMM bending rigidity increases with increasing adsorbed-particle shape-anisotropy. Besides measurement of bending rigidity, its consequences on particle deposition during evaporation in confined geometries are explored. We discover that increased interfacial bending rigidity dramatically changes particle deposition during evaporation. Spheres can locally pin the three-phase contact line, which then bends around the pinning site and produces an uneven deposition. Conversely, the large bending rigidity induced by adsorbed ellipsoids makes deformation of the contact line energetically costly and ultimately induces uniform deposition. Surprisingly, drops of spheres doped with small numbers of ellipsoids are also deposited relatively uniformly in these confined geometries.

3.2 Method and Materials

Our experiments utilize micron-sized polystyrene particles with modified *shape*, stretched asymmetrically to different major-minor diameter aspect ratio, α [21, 52, 72]. The colloidal drops are confined between two glass slides separated by 38.1 μm spacers (Fisher Scientific); qualitatively similar results are found for chambers made from slightly hydrophobic cover slips. We investigate evaporation of these drops, i.e., suspensions containing particles of the same composition

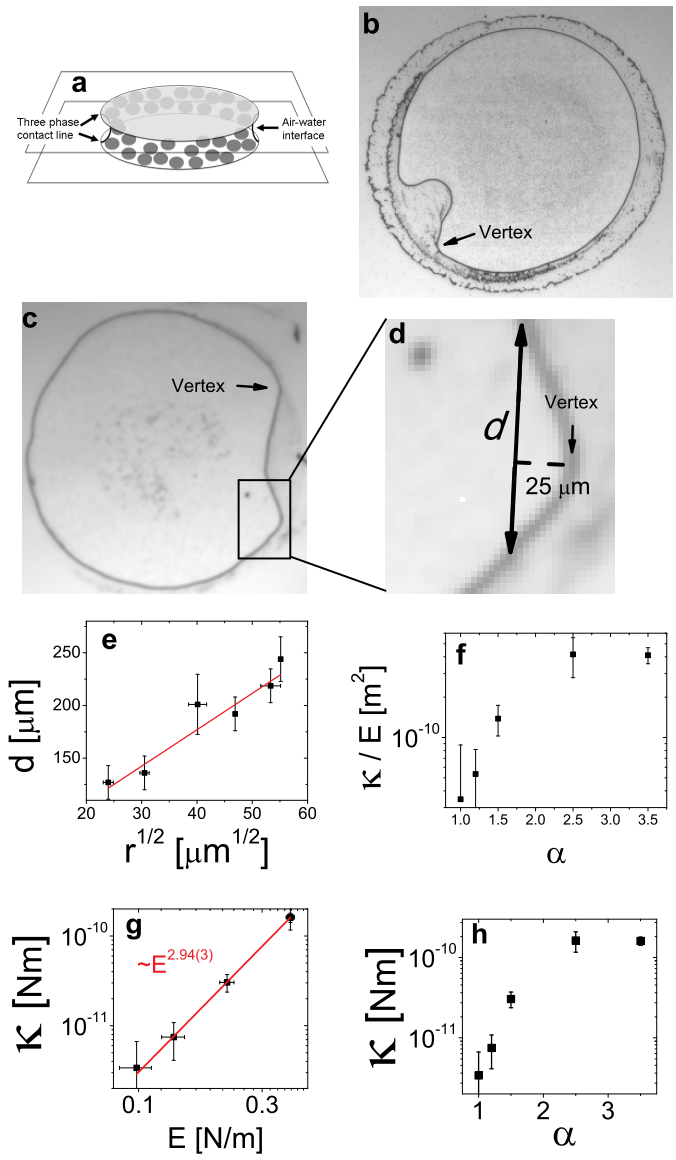

Figure 3.1: a. Cartoon depicting droplet evaporating in a confined geometry. The particle-populated air-water interface and three phase contact lines are labeled. b,c. Examples of buckling events for confined drops containing anisotropic particles with $\alpha = 1.2$ and 1.5 (b,c, respectively). d. Rim width, d (solid line), is defined here in a magnified image of a buckled region, as the interface full-width 25 μ m from the vertex of the bent air-water interface (see dashed line). e. d is plotted versus the square root of the drop radius, r. f. Ratio of the bending rigidity, κ, to the Young's modulus, E, is plotted versus α. g. κ versus E, where E comes from previously reported measurements and calculations. The line represents the best power law fit. h. κ versus α.

but with different major-minor diameter aspect ratio, including spheres ($\alpha = 1.0$), slightly deformed spheres ($\alpha = 1.2, 1.5$), and ellipsoids ($\alpha = 2.5, 3.5$). The spheres are 1.3μm in diameter; all ellipsoids are stretched from these same 1.3μm spheres. We primarily study the particle volume fraction $\phi = 0.01$. (Qualitatively similar results are found for volume fractions ranging from $\phi = 10^{-4}$ to 0.05.) At these low volume fractions, particles densely coat the air-water interface before buckling events occur. The confinement chambers are placed within an optical microscope wherein evaporation is observed at video rates at a variety of different magnifications.

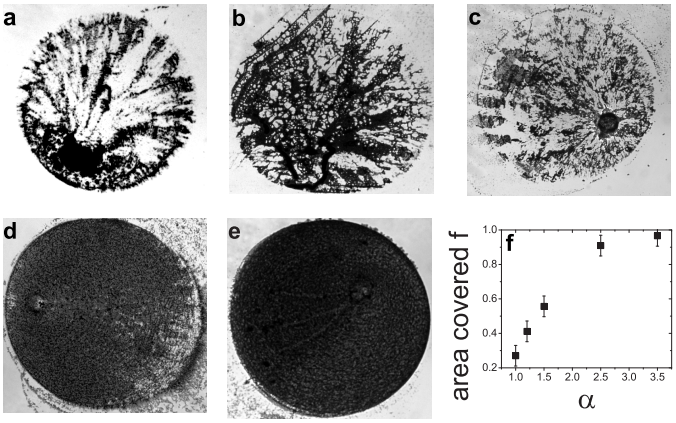

Figure 3.2: Image of the final deposition of particles with major-minor diameter aspect ratio $\alpha = 1.0, 1.2, 1.5, 2.5, 3.5$ (a-e, respectively). f. The area fraction covered by particles after evaporation is complete, *f*, for suspensions of particles as a function of their aspect ratio α.

During evaporation, the air-water interface deforms and crumples (Fig. 3.1 b and c). The buckling behaviors exhibited by the ribbon-like CMMs in confined geometries are strongly dependent on the shape of the adsorbed particles, and the buckling events appear similar to those observed in spherical-shell elastic membranes [99, 167]. Before buckling events occur, particles are maximally packed near the three-phase contact line, regardless of particle shape. Further, because the volume fraction is relatively low, membranes essentially contain a monolayer of

particles, i.e., buckling events occur before multilayer-particle membranes form.

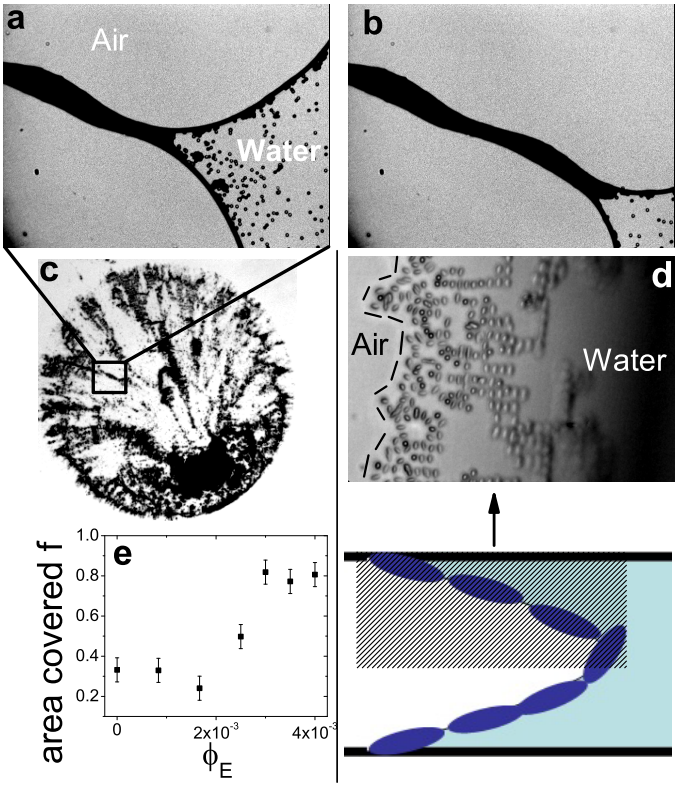

Figure 3.3: a. Image of a pinned region of the air-water interface ($\alpha = 1.0$). When the pinned section does not "snap" off, it leaves behind a channel. b. At a later time ($\sim$100 seconds after (c)), the channel extends, and more particles flow into it, producing a very heterogeneous deposition. c. Image of the final deposition of particles with major-minor diameter aspect ratio $\alpha = 1.0$. The box indicates the deposit left behind by the event depicted in (a) and (b). d. Image of a colloidal monolayer near the three phase contact line in a drop containing ellipsoids ($\alpha = 3.5$). The three phase contact line is labeled with a dashed line on the left side of the image. Particles are adsorbed on the air-water interface, forming a monolayer, as evidenced by the fact that particles become more out of focus, from left to right, as the air-water interface curves. A cartoon below shows a side view of the experimental image. e. The fraction of area covered by particles, *f*, for suspensions of 200 nm diameter spheres doped with different amounts of ellipsoids, represented by the ellipsoid volume fraction, ϕ_E.

3.3 Theory of Buckled Quasi-2D Membranes

To understand this phenomenon, we quantify the elastic properties of the air-water interface with adsorbed particles (i.e., the elastic properties of the CMMs). We extend analytical descriptions of elastic membranes to our quasi-2D geometry wherein observations about bending and buckling geometry are unambiguous. Following [99], we first describe the stretching and bending energy associated with membrane buckling events. Membrane stretching energy can be written as $E_S = 0.5 \int Eu^2 dV$, where E_S is the total membrane stretching energy, E is the 2D Young's modulus, u is the strain, and the integrand is integrated over the membrane volume. For a thin, linearly elastic material, u does not change much in the direction perpendicular to the surface, so $E_S \cong 0.5 \int Eu^2 dA$, where the integral is calculated over the membrane surface area. The unstretched region has $u = 0$. Further, most of the deflected region has $u = 0$, since its configuration is identical to the undeflected membrane; its curvature is simply inverted (Fig. 3.4 a). Thus, the only region under strain is the deflected rim (Fig. 3.4 a). If the entire membrane had experienced a constant radial displacement of ζ, its radius would change from r to $r + \zeta$, and the circumference would change from $2\pi r$ to $2\pi(r + \zeta)$. Then the membrane strain would be $u = 2\pi\zeta/2\pi r = \zeta/r$. If, as is the case for our samples, the displacement is confined to a small region subtended by some angle θ, then the in-plane length of this region changes from θr to $\theta(r + \zeta)$, and the total strain in the membrane is $u = \theta\zeta/\theta r = \zeta/r$. This estimate assumes that the interfacial deflection does not change in the z-direction (out-of-plane), i.e., $\partial\zeta/\partial z \approx 0$. Thus, $E_S \cong 0.5 \int E(\zeta/r)^2 dA$. The integral is performed over an area normal to the glass plates described by $A \approx dh$, where d is the in-plane length of the deflected region, and h is the chamber height. Thus, $E_S \approx 0.5E(\zeta/r)^2 dh$.

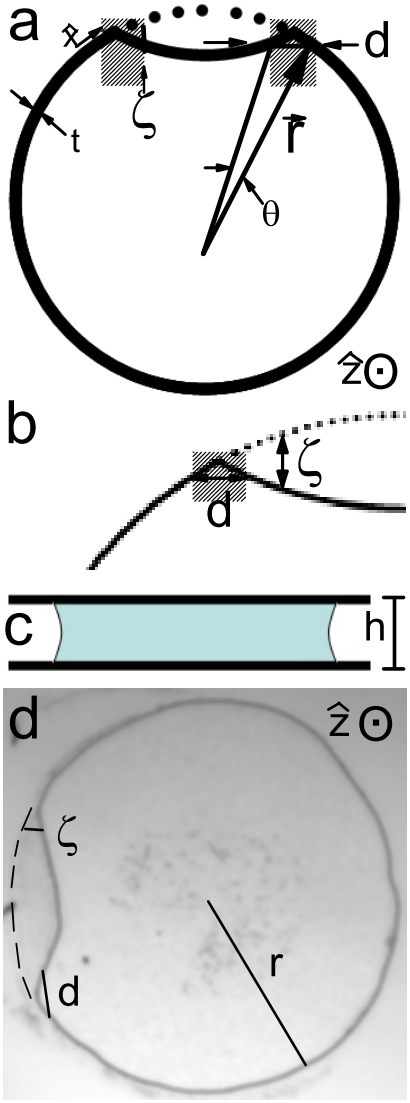

Figure 3.4: a. Buckling event cartoon defining rim full-width, d, drop radius, r, interface displacement, ζ, membrane thickness, t, in-plane direction along membrane surface, $\hat{x}$, angle, θ, and out-of-plane direction, $\hat{z}$. The dotted line represents the initial membrane configuration (before the buckling event). The regions containing all buckling and stretching energy are shaded. All un-shaded regions are unstretched and unbent. b. Magnified buckling event cartoon defining rim full-width, d, and interface displacement, ζ. The regions containing all buckling and stretching energy are shaded. c. Side view cartoon defining chamber height, h. d. Example of buckling event for a confined drop containing anisotropic particles with $\alpha = 1.5$. The rim width, d (solid line), drop radius, r, interface displacement, ζ, and out-of-plane direction, $\hat{z}$, are defined here. Dashed line indicates initial position of membrane.

The membrane bending energy can be written as $E_B = 0.5 \int \kappa K_C^2 dA$, where E_B is the total bending energy, κ is the bending rigidity, and K_C is the membrane curvature. Here, the curvature is $K_C \approx \partial^2 r(\theta)/\partial x^2$, where x is the coordinate in-plane along the membrane. The first derivative can be written as $\partial r(\theta)/\partial x \approx \zeta/d$, as ζ is the change in the membrane position over a distance of approximately d in the x direction. The second derivative can then be estimated as $\partial^2 r(\theta)/\partial x^2 \approx \zeta/d^2$, as the first derivative changes from 0 in the undeflected region to ζ/d in the deflected region of approximate length d. Therefore, $K_C \approx \zeta/d^2$. (This assumes that the second derivative of the deflection in the z-direction is small, i.e., $\partial^2 \zeta/\partial z^2 \approx 0$.) Again, the integral is performed over an area described by $A \approx dh$. Thus, $E_B \approx 0.5\kappa h \zeta^2/d^3$.

The total energy, E_{TOT} from the deflection is $E_{TOT} = E_S + E_B = 0.5E(\zeta/r)^2 dh + 0.5\kappa h\zeta^2/d^3$. This energy is located within the deflected rim (with width d). Membranes buckle in such a way as to minimize their energy. Thus, we next minimize the total deflection energy with respect to d, i.e., $\partial E_{TOT}/\partial d = E(\zeta/r)^2 h - 3\kappa h\zeta^2/d^4 = 0$. As a result of minimizing the total bending and stretching energy, $\kappa/E = d^4/(3r^2)$. Thus, by measuring d and r, we can experimentally determine κ/E. (Note, ζ drops out of the calculation, i.e., a precise determination of ζ is not necessary for this calculation, given the assumptions listed above. Also, this calculation is independent of the depth of the invagination, but it does require that the deflection minimizes the total membrane energy.)

In practice we measure d as the full-width located 25 μm from the rim vertex (see Fig. 3.1 f). However, the value of d is not very sensitive to measurement protocols. Defining d as the full-width at 20 μm or 30 μm from the rim vertex changes its value by approximately 10 percent.

This simple approach enables us to extract the ratio of CMM bending rigidity, κ, to its

Young's modulus, E, from measurements of d and r. In particular, minimizing the bending and stretching energy with respect to d yields the relation $\kappa/E = d^4/(3r^2)$. With all other parameters constant, e.g., particle anisotropy, etc., this formula predicts that $d \propto \sqrt{r}$. (Note, this derivation assumes that the interfacial displacement varies little in the z-direction, i.e., the air-water interface deflects the same distance at the top, middle, and bottom of the chamber.) In Fig. 3.1 e we show results from evaporated drops of particles with anisotropy $\alpha = 1.2$ and with different initial values of r, plotting d versus $\sqrt{r}$. A good linear relationship is observed (coefficient of determination, $R^2 = 0.93$), implying that our analysis is self-consistent. Similar linear results were found for other values of α.

In principle, the air-water interface can be distorted in the z-direction as well as in-plane. We have previously assumed that these distortions are small. The exact location of the air-water interface is difficult to directly measure optically; when light enters the sample, it travels through water, then air, then water again, and finally through air and into the microscope objective. This strongly distorts confocal images. However, using bright field microscopy, we can identify the inner and outer position of the air-water interface, allowing us to estimate the radius of curvature in the z-direction [131] (Fig. 3.5). We find that the radius of curvature is approximately equal to the chamber thickness ($\sim 38.3\mu$m $\pm 1\mu$m). We do not observe any change in this measurement after a buckling event. The relevant partial derivatives are then $\partial\zeta/\partial z \leq 1/38.3$ and $\partial\zeta/\partial z \leq 1/(38.3^2)$, and are thus small.

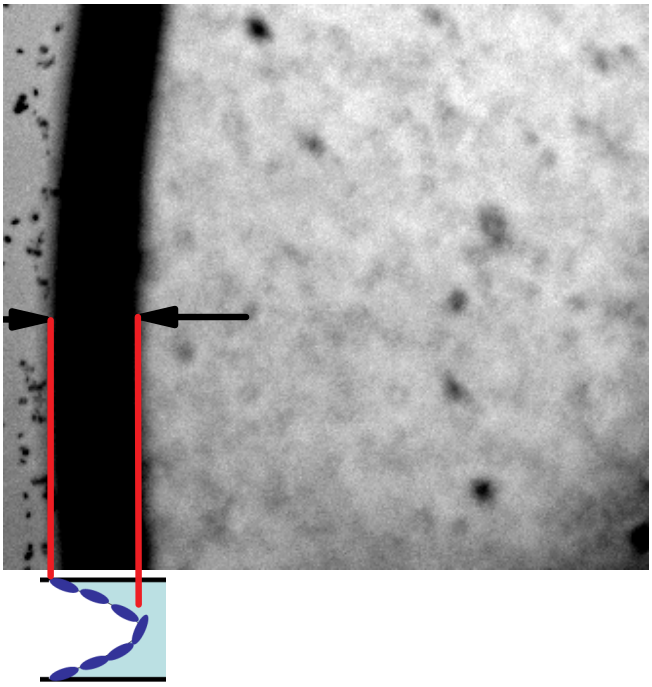

Figure 3.5: Experimental image of air-water interface demonstrating how the radius of curvature is measured. Red lines represent the inner and outer edges of the air-water interface, as shown in the cartoon below.

3.4 Dependence of Bending Rigidity on Particle Shape

We thus extract and plot κ/E for evaporating drops of particles with different α (Fig. 3.1 f). Notice, κ/E increases with increasing α, implying that as α increases, κ increases faster than E, i.e., κ/E is larger for ellipsoids ($\alpha = 2.5$ and 3.5) than for spheres ($\alpha = 1.0$). CMM Young's modulus is known to increase with α [9, 111, 119, 141, 165].

To extract the bending rigidity, we need to know the Young's modulus of the membrane. For particles with $\alpha = 1.0$ and 2.5, we are able to use previously reported values of the bulk modulus [9], B, the shear modulus [111], G', and the relationship $E = 4BG'/(B+G')$ in order to extract the Young's modulus. We were unable to find data for $\alpha = 1.2, 1.5$, or 3.5, so we interpolated from reported values of B and G'. Using these previously reported values, we obtained $E = 0.098, 0.14, 0.22, 0.39$, and 0.39 N/m for $\alpha = 1.0, 1.2, 1.5, 2.5$ and 3.5, respectively.

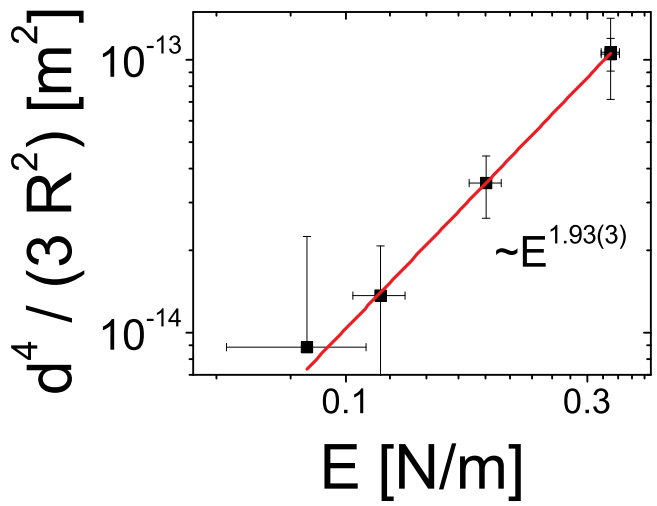

Figure 3.6: As a consistency check, $d^4/(3r^2)$ is plotted versus E. The line represents the best power law fit.

Utilizing previously reported measurements and calculations of E, we plot κ versus E (Fig. 3.1 g) and find that $\kappa \propto E^{2.94(3)}$. This observation is consistent with theoretical models which

predict $\kappa \propto E^3$ [99], however, the full physical origin of this connection is unclear. At first glance, it seems contradictary to claim that $\kappa/E = d^4/(3r^2)$ and $\kappa \propto E^3$. However, these formulae are consistent. A simple elastic model assumes that $E = Yt$ and $\kappa = Yt^3$, where Y is the 3D Young's modulus and t is the membrane thickness [99]. Based on this model, $\kappa = E^3/Y^2$, so $\kappa/E = E^2/Y^2$. Thus, $\kappa/E = E^2/Y^2 = d^4/(3r^2)$. To test this we plot $d^4/(3r^2)$ versus E (Fig. 3.6). The best power law fit is $d^4/(3r^2) \propto E^{1.92(3)}$, implying that these two equations are consistent. Note, this implies that $Y \approx 19$ kPa for all α, which is similar to stiff jello (Fig. 3.7). Additionally, these values of Y allow us to calculate t (Fig. 3.8). The physical interpretations of Y and t are unclear. Finally, we use previously reported measurements and calculations of E to isolate and estimate CMM bending rigidity (Fig. 3.1 h). Clearly, membrane bending becomes more difficult with increasing particle anisotropy.

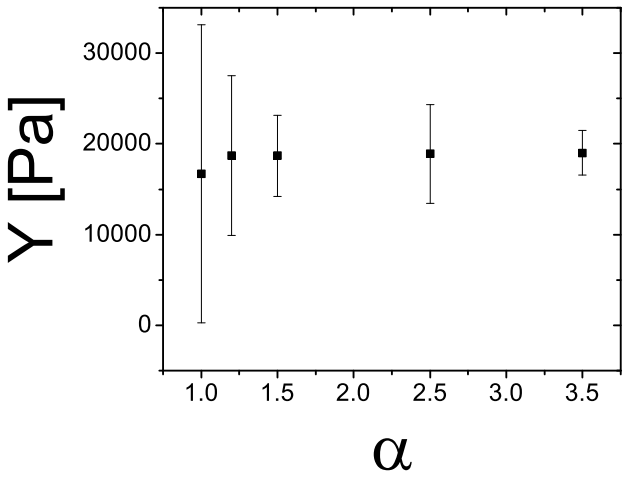

Figure 3.7: 3D Young's modulus, Y, is plotted versus aspect ratio, α.

3.5 Particle Deposition in Confined Geometries

We next turn our attention to the consequences of increased bending rigidity on evaporation processes in confined geometries, specifically particle deposition during drying. Substantial effort has now yielded an understanding of the so-called coffee-ring effect and some ability to control particle deposition from sessile drops [15, 37, 40, 48, 76, 77, 83, 124, 126, 153, 171, 186]. However, much less is known about particle deposition in confined geometries, despite the fact that many real systems [29, 50, 143] and applications [11, 30] feature evaporation in geometries wherein the air-water interface is present only at the system edges. Recent experiments have explored evaporation of confined drops containing spheres [34, 86, 102, 131], and their behaviors differ dramatically from sessile drops containing spheres. In the confined case, as noted previously, particles are pushed to the ribbon-like air-fluid interface, and, as evaporation proceeds, the particle-covered air-water interface often undergoes the buckling events described above.

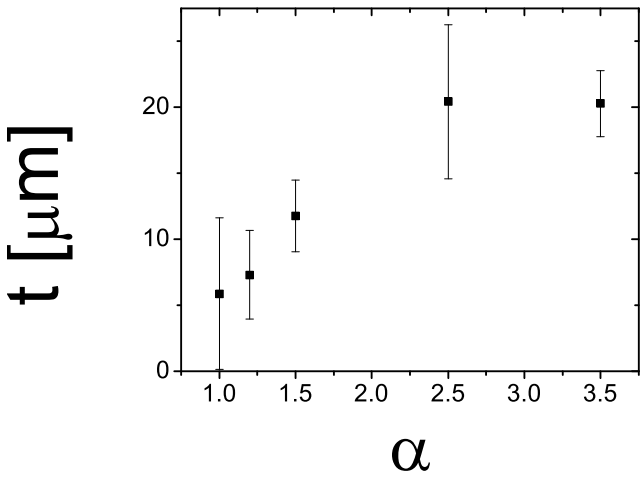

Figure 3.8: The calculated membrane thickness, t is plotted versus aspect ratio, α.

We find that suspended particle shape produces dramatically different depositions as a result of the varying CMM bending moduli. In Fig. 3.2 a-e, the final deposition of particles is shown for $\alpha = 1.0, 1.2, 1.5, 2.5, 3.5$, respectively. Spheres and slightly stretched spheres are deposited heterogeneously, and anisotropic ellipsoids are distributed relatively more uniformly. To describe the final deposition of particles more quantitatively, we plot the fraction of initial droplet area covered by deposited particles after drying, *f* (as introduced in [36]), as a function of anisotropy α (Fig. 3.2 f). To compute *f*, we divide the area into a grid of ($8\ \mu m$ X $8\ \mu m$) squares; a region is considered to be covered, if its area fraction within the square is greater than 0.36. The number of covered regions is then normalized by the total number of squares in the grid, producing *f*. Note, for uniformly deposited particles, the area fraction (based on the initial volume fraction, initial volume, chamber height, and particle size) would be ~ 0.4. The fraction of area covered with particles is observed to increase with α. For $\alpha = 1.2$ and 1.5, f increases modestly. For $\alpha = 2.5$, the deposition is very uniform, and for $\alpha = 3.5$, virtually the entire area is covered uniformly.

High magnification images reveal why spheres and slightly stretched particles deposit unevenly, while ellipsoids deposit more uniformly (Fig. 3.3 a-d). Spheres and slightly-stretched spheres often pin the air-water interface, preventing its motion. In fact, spheres can pin the air-water interface even in very dilute suspensions, i.e., $\phi < 10^{-4}$. As evaporation continues, the CMM interface bends around the pinning site (Fig. 3.3 a). Then, it either pinches off, leaving particles behind, or it remains connected to the pinned site, leading to water flow into the narrow channel that has formed; the latter flow carries particles towards the pinning site (Fig. 3.3 a and b) producing "streaks" of deposited particles (Fig. 3.3 c). Temporal and spatial heterogeneities

along the interface due to these described effects lead to heterogeneous deposition of spherical particles during evaporation.

When ellipsoids approach the drop edge, they also adsorb onto the air-water interface forming ribbon-like CMMs (Fig. 3.3 d) [16, 19, 80, 105, 106, 111, 112]. However, the ellipsoids induce substantial capillary deformations on the air-water interface, creating an elastic membrane with a high bending rigidity. Ellipsoids can also pin the contact line, but bending of the CMM interface around a pinned contact line requires an energetically costly rearrangement of ellipsoids aggregated on the CMM, since attractive particle-particle capillary interactions must be overcome (even at very small ϕ). Conversely, bending of the contact line costs little energy to spheres on the interface, because sphere-sphere capillary interactions on the interface are much weaker than for ellipsoids [105, 106, 127]. As evaporation continues, the ellipsoid-CMM contact line recedes radially, and the ellipsoids near the contact line are deposited on the substrate. This behavior is similar to convective assembly techniques wherein the substrate, or a blade over the substrate, is pulled away from the contact line; a thin film is thus formed that leads to the creation of a monolayer (e.g., [98]). The present system, by contrast, has neither moving nor mechanical parts. Uniform coatings are created essentially as a result of shape-induced capillary attractions which produce CMMs that are hard to bend.

3.6 Mixtures of Spheres and Ellipsoids

To further elucidate the effects of particle shape on deposition, suspensions of 200 nm spheres (α=1.0) with ϕ=0.02 were combined with suspensions containing micron-sized ellipsoids (α=3.5) at lower volume fractions, ϕ= 0 to 4.0×10^{-3}. The resulting colloidal drops were evaporated

in the same confined geometries. The addition of a very small number of ellipsoids has no effect on the deposition of spheres ($\phi \leq 1.7 \times 10^{-3}$). Surprisingly, the addition of a larger, but still small, number of ellipsoids leads to a uniform deposition of both ellipsoids and spheres, i.e., $f \approx 0.8$, despite the fact that spheres outnumber ellipsoids by a significant factor (10^3-10^4) (Fig. 3.3 e). Apparently, spheres do not prevent ellipsoids from adsorbing on the air-water interface, and the CMM bending rigidity is dominated by the presence of ellipsoids. Thus, the membrane still resists bending around pinning sites. This behavior in confined geometries is different than that of sessile drops wherein it was discovered that if the spheres are larger than the ellipsoids, then the spheres are distributed uniformly after drying, but if the spheres are smaller than the ellipsoids, then they exhibit the coffee ring effect [186]. From this perspective, it is somewhat surprising that small spheres are deposited uniformly from droplets doped with small numbers of ellipsoids and confined between glass plates.

Again, the high bending modulus produced by ellipsoids on the CMM helps explain the observations. Both spheres and ellipsoids attach to the air-water interface. Ellipsoids deform the air-water interface, creating an effective elastic membrane with a high bending rigidity. When enough ellipsoids are present, pinning and bending the interface becomes energetically costly and the spheres (and ellipsoids) are deposited as the interface recedes.

3.7 Summary

To summarize, ellipsoids adsorbed on the air-water interface create an effective elastic membrane, and as particle anisotropy aspect ratio increases, the membrane's bending rigidity increases faster than its Young modulus. As a result, when a drop of a colloidal suspension evaporates in a confined geometry, the different elastic properties produce particle depositions that are highly dependent on particle shape. This observed increase in bending rigidity with particle shape aspect ratio holds important consequences for applications of colloidal monolayer membranes as well. For example, increased bending rigidity may help stabilize interfaces (e.g., Pickering emulsions [112]) and thus could be important for many industrial applications, e.g., food processing [41, 166]. In a different vein, our observations suggest that CMMs in confined geometries may be a convenient model system to study buckling processes that are relevant for other systems, e.g., polymeric membranes [163], biological membranes [53], and nanoparticle membranes [121].

Chapter 4

Irreversible Rearrangements, Correlated Domains and Local Structure in Aging Glasses

4.1 Introduction

After initial formation, glasses relax via a non-equilibrium process called aging during which their *dynamics* slow dramatically and become more heterogeneous. Interestingly, the diverging relaxation timescales and viscosities characteristic of the glass transition likely derive from an analogous emergence of heterogeneous particle domains that rearrange in a correlated manner [3]. The structural causes of this so-called dynamic heterogeneity, however, remain elusive. Recent work has searched for connections between dynamics and structure [88, 117, 138, 148, 160, 168, 169, 174], for example, suggesting short-range crystalline order as a structural cause

of dynamic heterogeneity [88, 138, 168]. The fruits of this continued search, if attained, will be directly applicable to the concepts of dynamical arrest as they apply to the glass transition and will thereby unify physical phenomena observed across a broad spectrum of jammed systems including colloidal suspensions [169], granular media [2, 168], metallic glasses [148, 149], and polymer glasses [74].

The slow nature of glass dynamics makes them intrinsically challenging to study, requiring observations on very short and very long timescales. In this paper we ameliorate the timescale problem by studying the aging of colloidal glasses immediately after a deep quench [93]. Bidisperse suspensions of temperature-sensitive colloidal particles confined in two-dimensions (2D) are quenched from liquid to glass states. The rapid and deep quench permits study of glass dynamics from very short timescales to very long timescales, i.e., over observation times sufficient for significant structural changes to occur and evolve. Video microscopy measurements reveal the development of short-range order during aging and establish a direct connection between locally-ordered particles and dynamic heterogeneity. We discover that most of the fast-moving particles are not major participants in the aging process. However, a careful analysis of fast particle dynamics during aging identified an increase in the cluster size of a particular class of correlated particles, clusters of fast-particles participating in *irreversible rearrangements*. These irreversible rearrangements are similar to those recently identified in simulation studies [174]. The increase in irreversible rearrangement cluster size, as well as the observed increase in number of stable particle configurations, directly leads to the slowing dynamics characteristic of aging. Additionally, we find that particles with local crystalline order are very unlikely to irreversibly rearrange. Thus a direct link between local crystalline order, particle rearrangement,

and slowing dynamics is experimentally demonstrated.

4.2 Methods and Materials

The experiment employs an aqueous suspension of micron-size poly(N-isopropyl acrylamide) microgel colloidal spheres (i.e. NIPA particles), whose diameters increase as temperature is reduced [132, 142]. The particles are very similar to those used in recent phase transformation experiments and are described therein [4, 66, 68, 147, 176, 191]. Colloids are especially good models for studying the local structure of high density systems such as glasses, wherein free volume considerations determine local packing [22, 137]. A binary mixture of NIPA particles is sandwiched between two glass cover slips, thereby creating a quasi-2D system (the plate separation is $< 5\%$ greater than the diameter of the large particles [68]). The sample consists of a mixture of NIPA spheres with small and large diameters, D_S = 1.09 μm and D_L = 1.55 μm (for comparison, our resolution is $\sim$ 0.01 μm), respectively, at temperature T = 28.0 C. Approximately 45$\%$ (by number) of the particles are large. There are $\sim$4000 particles in the field of view, and this field of view resides within the middle of a much larger domain containing 325,000 particles. The polydispersity of each particle type is $\sim$3 percent, and the particle interaction potentials have been measured to be short-range repulsive with a soft tail [66]. The use of this binary mixture minimizes the possibility of crystallization, and the softness of the NIPA colloid interparticle potential, by contrast to that of hard spheres, permits access to area fractions far above the glass transition [133, 179].

4.3 Rapid Quenching via Optical Heating

Rapidly quenching from liquid to glass is achieved through a new experimental twist utilizing optical heating. A small amount of red dye (Chromatech - Chromatint Red 1064), 0.3% by weight, is released into the suspension. This dye absorbs light from a mercury lamp focused through the microscope objective. The sample field of view ($\sim 5 \times 10^{-3}$ mm^2) lies at the center of the illumination region ($\sim$1 mm^2). There, the temperature is increased by $\sim$4 degrees in $\sim$0.1 seconds via light absorption and relaxation processes. The NIPA particle radii are thus abruptly decreased by $\sim$0.1 μm, and the local area fraction (ϕ_A) is decreased by $\sim$10%. While the lamp is on, the particles are in the liquid state, as evidenced by their diffusive mean-square particle displacements (MSD): $MSD = \langle \Delta x_i^2 \rangle$ (see Fig. 4.2). The Brownian time of micron sized particles is $\sim$1 second, and the lamp is only on for $\sim$6 seconds, so thermophoretic effects are avoided. When the mercury lamp is turned off, the excess heat rapidly dissipates, and particles swell to their original size in less than 0.1 seconds. The rapid change from small-ϕ_A (liquid) to large-ϕ_A creates a glass. Aging begins (t_w = 0 seconds) once the sample returns to thermal equilibrium and particles have completely returned to their original size, which is verified in situ (see next section).

In order to study aging, we must wait until our suspension has returned to thermal equilibrium, and particles are no longer expanding in size. To determine when particles swell to their original size we look at the size of the particles before, during, and after optical heating. Fig. 4.1 plots the size of the particles versus time, in terms of pixel brightness radius of gyration. The lamp is turned off at approximately t_w = -0.133. At time t_w = 0 seconds, the radius of gyration

of the particles has stopped changing. Thus, our study of aging begins at that time.

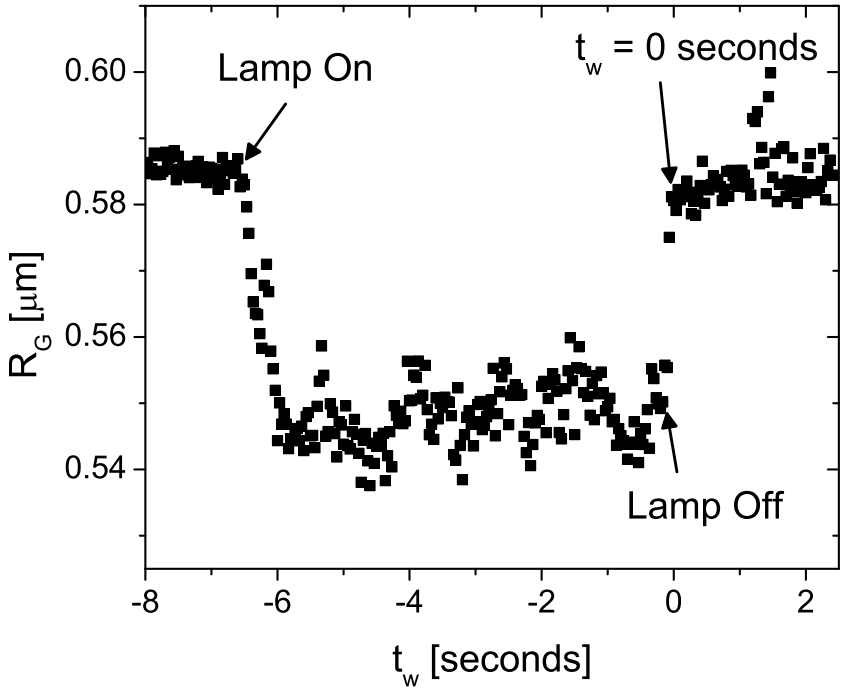

Figure 4.1: Pixel brightness radius of gyration before, during, and after optical heating.

Performing the experimental quench was quite challenging. In particular, selecting the proper amount of red dye proved to be non-trivial. If not enough red dye in the system, then less light from the mercury lamp will be absorbed, and the local temperature will not increase enough to lower the area fraction from that of a glass to that of a liquid. Thus, the quench will not change the system enough, and much smaller changes will be observed. However, since the dye is a suspension of small molecules, too much dye could lead to entropic depletion effects, creating short-range attraction between the NIPA particles. For the experiments described in this paper, we used $\sim$0.3% dye, by weight. This amount of dye was sufficient to increase local temperature by $\sim 4^\circ$ C. To insure that depletion effects were unimportant, we dissolved 0.3% dye by

weight into a dilute suspension of NIPA particles, and then we measured the particle-particles interaction potential. No attraction was observed, thus depletion effects were confirmed to be absent. In-situ, we can screen for depletion effects by watching for particles that stick to the glass slides. In a quasi-2D system, the depletion force would pin the NIPA particles against the glass slides. Our particles were not pinned to the glass slides; thus depletion effects are probably not an issue.

The data contained in this report were collected at five final ϕ_A ranging from ϕ_A = 0.81 to ϕ_A = 0.84; the data presented in Fig. 4.2-4.9 are taken solely from samples with ϕ_A = 0.84, where the effects described below are strongest. This *rapid and deep quench is a unique feature* of the NIPA particle experiments which permits measurement of aging over a broad range of timescales [93] that were not accessible to previous aging experiments [27,31]. A similarly deep quench was reported recently by Assoud *et al.* [42]; their experiment used rapid magnetic field changes to quench long-range repulsive magnetic particles from liquid to *crystal* states in 2D.

4.4 Aging Dynamics

During aging, glass dynamics depend on elapsed time from the quench, which we refer to as the waiting time, t_w. The ensemble-averaged particle MSD shown for different t_w in Fig. 4.2 exhibit aging dynamics of a typical glass [31]. The initial MSD plateau corresponds to caged particle behavior, and the "upturn" at longer times occurs when these cages rearrange. As t_w increases, the MSD upturn occurs at later times until it finally falls outside the experimental window.

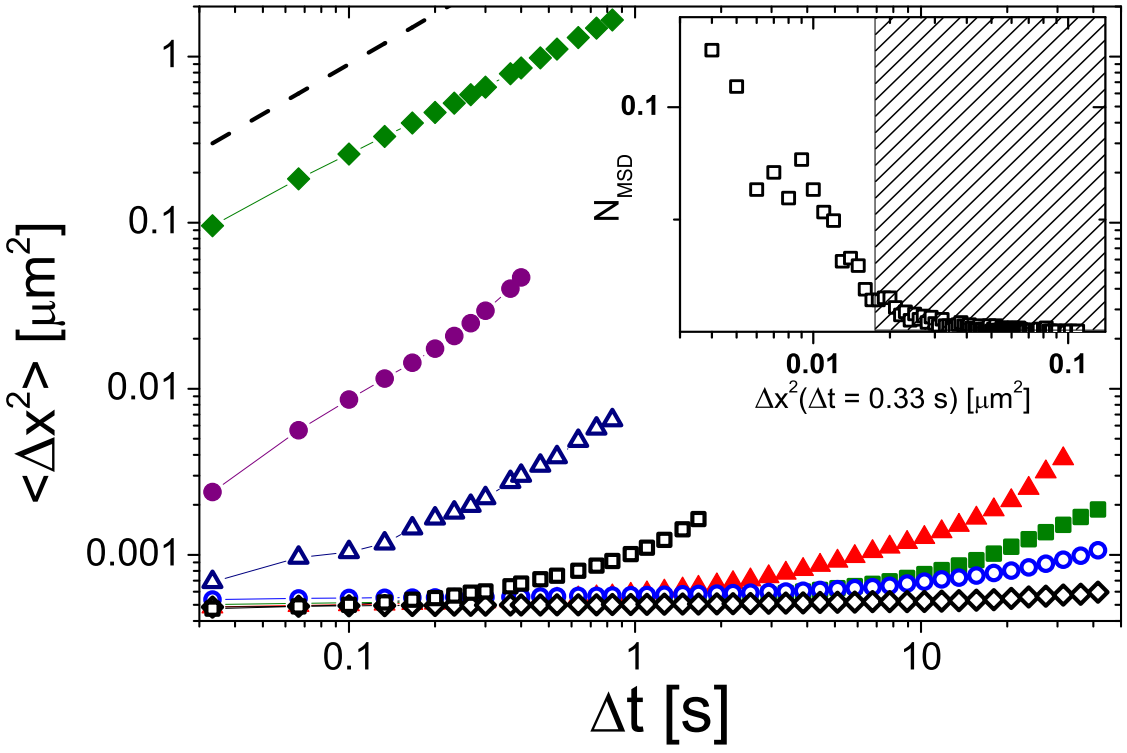

Figure 4.2: Mean-square displacement at different times after the quench (t_w): the liquid state before the quench (solid diamonds), t_w = 0.25 s (solid circles), 1 s (open triangles), 3.33 s (open squares), 36 s (solid triangles), 86 s (solid triangles), 143 s (open circles), and 10,000 s (open diamonds). Solid lines guide the eye, and the dashed line has a slope of 1 on a log-log plot. Inset: N_{MSD}, the fraction of particles with a given mean-square displacement for $0 \leq t_w \leq 3$ seconds and $\Delta t = 0.33$ seconds. All particles that irreversibly rearrange have mean-square displacements that fall in the shaded region.

Surprisingly, the MSD appears to grow faster than linearly with time for $t_w = 0.25$ seconds (Fig. 4.2). This could be because stress-relieving rearrangements push particles, resulting in displacements that are larger than displacements due to Brownian motion. However, this curve only extends over one decade in Δt. Thus, there is not sufficient data to fully comment on the dependence of MSD on Δt within this regime.

To more fully characterize the dependence of the dynamics on t_w, the MSD for two different lag times (Δt = 3.3 seconds, 33.3 seconds) is plotted versus t_w in Fig. 4.3.

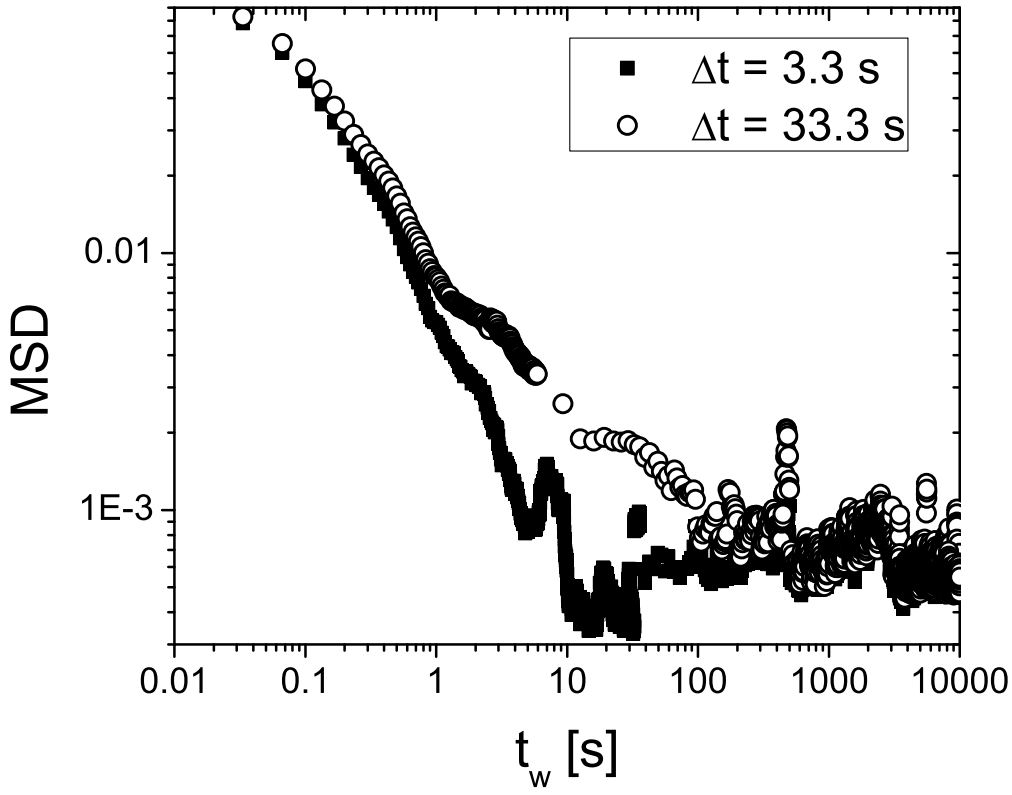

Figure 4.3: The mean-squared displacement versus t_w, for Δt = 3.3 seconds (solid squares) and Δt = 33.3 seconds (open circles).

4.5 Irreversible Rearrangements

Constituent particles in glasses tend to rearrange in a correlated manner involving many neighbors [3, 12, 95, 169], making it difficult to determine which particle configuration was initially unstable by use of mean-square displacements [172, 173]. Thus a different dynamic quantity that isolates the dynamic heterogeneity essential to relaxation appears to be required, such as the *irreversible rearrangement* (IR) [174]. In recent two-dimensional simulations, Widmer-Cooper *et al.* identified a class of particles that undergo *irreversible rearrangements* (IRs) [174]. They found that if a motional event causes a particle to lose four of its nearest neighbors, then the particle rarely recovers its initial configuration. These so-defined irreversible rearrangements facilitate differentiation between affine motions that maintain local structural configurations, and non-affine motions that contribute to relaxation. Neighbors are calculated using a cutoff distance defined by the first minimum in the particle pair correlation function [28,62,94]. Defining neighbors by Voronoi tessellation gave qualitatively similar results. Within our experimental time window, particles never regain their original configurations after losing three nearest neighbors; thus we say that these particles experience an IR. These particles are among the fastest in the system (see Fig. 4.2 inset), and less than 1% are large spheres, consistent with prior work [109].

Specifically, another challenge we face in data analysis concerns defining exactly when an IR occurs for the purpose of calculating clusters of fast particles that contain IRs. This challenge was resolved by identifying a particle as undergoing an IR from the time it lost its first nearest neighbor, until the time it loses its third nearest neighbor. To identify every particle that moved as part of this rearrangement, the lag time, Δt, that we used to identify the 10% fastest particles

was varied and the largest cluster size was selected. One may naively expect the cluster size to simply increase with lag time. However, this is not the case. When the lag time is larger than the rearrangement time, more motional events are considered when selecting the 10% fastest particles. Thus, some of the slowest particles that belong to a particular cluster will be lost, since other unrelated particles will move comparable and larger distances. During aging, Δt increases, roughly following a power law of Δt$\sim$0.8. The lag time ranges from Δt = 0.33 seconds to Δt$\sim$1000 seconds.

At the earliest waiting times, $t_w < 0.5$ seconds, at the time of an irreversible rearrangement, the cluster of fast moving particles contains $\sim$60% of the particles that will ultimately join in the correlated domain. However, at these early times there are more than one irreversible rearrangement per cluster of fast particles, making it impossible to determine a causal link when $t_w < 0.5$ seconds. Fortunately, the irreversible rearrangements that occur after t_w = 0.5 seconds are isolated events.

To study the variation in correlated rearrangements with t_w, we first determined the number of IR events occurring as a function of t_w (Fig. 4.4 A). The rate of IRs is initially high; $\sim$90 events occur when $t_w < 0.4$ seconds. However, the rate slows dramatically thereafter, and only $\sim$15 events occur over the rest of the experiment. Next, we identified particles that move much farther than average. The particles moving farther than r_C were selected, with r_C chosen so that only 10% of all of the particles satisfy $|\overrightarrow{\Delta r(\Delta t)}| > r_C$, where $|\overrightarrow{\Delta r(\Delta t)}|$ is the particle displacement in time Δt. Clusters of particles that move farther than r_C were identified by connecting nearest-neighbor pairings of "fast" particles. This definition of "fast" particles and fast particle clusters has been used previously in experiments [169] and simulations [43, 133].

The time required for a complete rearrangement varies, so we vary Δt to maximize the average number of particles per cluster at each t_w (Δt ranges from 0.33 seconds to 20.0 seconds but is typically $\sim$0.5 seconds). (See online Supplemental Information.) The average number of particles per fast cluster versus t_w is plotted in Fig. 4.4 B; it actually *decreases* from $\sim$5 particles immediately after the quench, to $\sim$2 particles at t_w = 10,000 s. This result is somewhat surprising, as previous simulations reported a dynamic length scale that grew during aging [129].

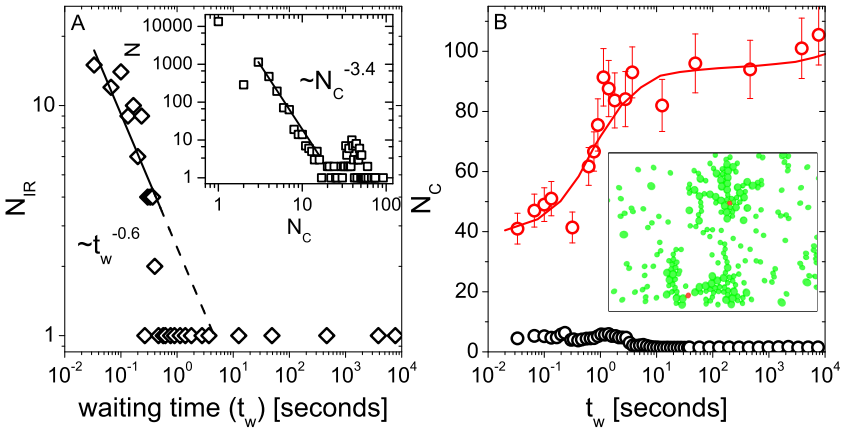

Figure 4.4: A: N_{IR}, the number of irreversible rearrangements, versus t_w. The line is a power law fit. Inset: Histogram of N_C, fast particle cluster sizes, for $0.03 \leq t_w \leq 3$ seconds. The line is a power law fit. B: Average number of fast particles per cluster for all clusters (black circles) and the average number of fast particles per cluster for only clusters containing a particle undergoing an irreversible rearrangement (red circles), versus t_w. The line guides the eye. Inset: Snapshot of the 10% fastest particles at t_w = 0.62 seconds, featuring two large clusters. Particles that irreversibly rearrange are plotted in red.

However, closer inspection reveals that very large clusters exist, some containing $\sim$100 particles (Fig. 4.4 A Inset). Interestingly, we found that most of these large clusters contained a particle undergoing an IR. A snapshot of the 10% fastest particles, featuring two such large clusters, is shown in the inset of Fig. 4.4 B. We calculated the average size of these clusters of fast particles, all of which contain a particle that underwent an IR. The results are plotted in Fig. 4.4

B. The average size of these clusters *increases* from ∼40 particles just after the quench, to ∼100 particles at t_w = 10,000 s; the radius of gyration of these clusters correspondingly increases from ∼2.5 μm to ∼4.5 μm. In other words, as the glass ages, more particles must move for IRs to occur. The observation that clusters of fast moving particles are dramatically larger *when an IR is involved* demonstrates an intimate connection between IRs and dynamic heterogeneity. This effect is reminiscent of the Adam and Gibbs hypothesis, which states that as the glass transition is approached, the number of correlated particles involved in a rearrangement increases [3, 73]. In the present case, the number of correlated fast particles involved in an irreversible rearrangement event increases with aging. Rearrangements thus become progressively more difficult to achieve, leading to slow glass dynamics and kinetic arrest (Fig. 4.2).

This growing correlated domain size helps explain why dynamics slow during aging; the connection between events that dramatically change local configurations (IRs) and large correlated domains reveal the microscopic mechanisms of the large viscosity characteristic of glass. More particles must move in a correlated manner as glass ages, making these IR events progressively more difficult to achieve. Because these events involve a more complex network of particles, they occur less frequently. The upturn in MSD occurs at later times, the relaxation time increases, or, to put it more simply: the dynamics slow. These complex correlated domains are the microscopic manifestation of the large viscosity characteristic of glass. Thus, glass has a large viscosity because many particles are required to move in a correlated manner for an IR, and relaxation, to occur.

Data derived from different final area fractions displayed similar behavior. The average size of a cluster containing at least one particle undergoing an IR after t_w = 1,000 s, increases from

$\sim$70 particles at ϕ_A = 0.81, to $\sim$100 particles at ϕ_A = 0.84.

To better understand this growing correlated domain, we calculated the initial coordination number of particles that irreversibly rearrange, and found that 90% had CN = 5, 5% had CN = 4, and 5% had CN = 6. For comparison, at t_w = 10,000 seconds, 60% of all particles have CN = 6, 31% have CN = 5, 8% have CN = 7, and 1% have CN = 4. This distribution of locally ordered stable particle configurations provides a structural source for heterogeneous dynamics in glasses [158].

4.6 Aging Structure

In fact, the enhanced stability of locally ordered particle configurations is evident during aging. The evolution of the distribution of CN during aging is readily visualized by snapshots of the glass at different t_w and is plotted in Fig. 4.8 A B. Patches of particles with coordination number CN = 6, i.e. particles with local crystalline order, develop during aging.

Properly identifying coordination number is crucial for the data analysis. Two methods are commonly used to identify nearest neighbors. Voronoi tessellation identifies a cell around each particle that contains every point in space closer to the said particle, compared to any other particle. Thus any two particles whose cells share a border are nearest neighbors. While this approach provides an entirely unambiguous definition of nearest neighbors, it can assign nearest neighbor pairings to sets of particles that are not actually in each others' first coordination shell. For example, regions of voids often exist after the quench. Particles that border the voids are sometimes

identified by Voronoi Tesselation as nearest neighbors with other particles that border the void, despite the fact that they are separated by relatively large distances. A snapshot of particles near a void with their corresponding Voronoi cells are shown in Fig. 4.5. Additionally, when glasses are at relatively high packing fractions, Voronoi Tesselation occasionally identifies two particles as nearest neighbors even though they are outside of each others' local environments (Fig. 4.6).

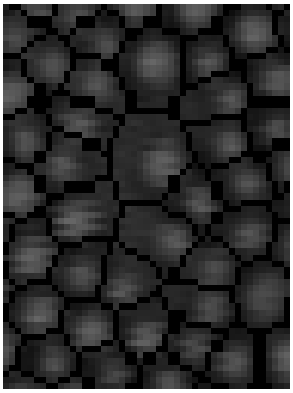

Figure 4.5: Snapshot of particles bordering a void at t_w = 0.03 seconds, with their corresponding Voronoi cells plotted over them.

To avoid the aforementioned issues, we use a different method for identification of nearest neighbors. We first assign a cutoff distance, r_c, based on the pair correlation function, g(r), such that any particles separated by less than r_c are identified as nearest neighbors [28, 62, 94]. Since the first peak in g(r) represents a particle's nearest neighbors, r_c was set to be the minimum of g(r) just after the first peak. While this scheme is trivial in a monodisperse system, the situation becomes more complex in a bidisperse system. Three distinct pair correlation functions can be calculated. In the bidisperse case we can calculate g(r) exclusively using large particles (g_{LL}), exclusively using small particles (g_{SS}), or using both large and small particles (g_{ALL}) (Fig. 4.7). In our experiments, the corresponding values of r_c were 1.75 μm (g_{LL}), 1.45 μm (g_{SS}), and 1.55 μm (g_{ALL}). In this paper we opted to use r_c = 1.55, the cutoff distance derived from g_{LS}, to

define nearest neighbors. A close examination of the data reveals this to be the most sensible choice, for the following reasons. First, our experiments did not exhibit any phase separation, $\sim$1% of particles were surrounded exclusively by particles of the same size, making g_{ALL} more representative of a typical local environment than g_{SS} or g_{LL}. We could have chosen g_{LL} for large-large bonds, g_{SS} for small-small bonds, and g_{ALL} for large-small bonds. However, examination of actual particle configurations shows that this assignment leads to inclusion of nearest neighbors that are not directly in a particle's first coordination shell, and leads to exclusion of nearest neighbors that are clearly in the particle's first coordination shell (again, see the dotted particles in Fig. 4.6, which would be identified as nearest neighbors using the cutoff from g_{LL}, but not from g_{ALL}).

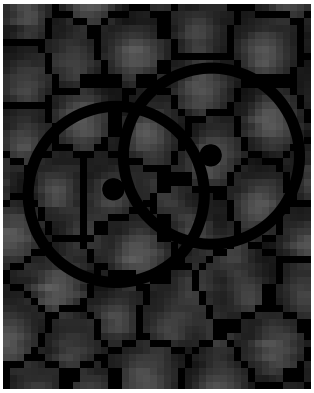

Figure 4.6: Snapshot of particles at t_w = 0.03 seconds. The particles marked with black dots are identified to be nearest neighbors by Voronoi Tesselation, or a cutoff distance based on g_{LL}. The cutoff distance from g_{LS}, represented by the black circles, does not define them to be nearest neighbors.

Fortunately, the qualitative results presented do not depend on the chosen method. Nevertheless, in this paper, we defined nearest neighbors based on a cutoff from g_{ALL}. With this method, the fraction of particles with 6 nearest neighbors grows from 0.48 to 0.59. For Voronoi

Tesselation, the fraction of particles with 6 nearest neighbors grows from 0.45 to 0.53. By using cutoffs from g_{LL}, g_{ALL}, and g_{SS} for each type of neighboring pair, the fraction of particles with 6 nearest neighbors grows from 0.40 to 0.58. When using r_c derived from g_{ALL}, $\sim$5% of irreversibly rearranging particles are identified as initially having 6 nearest neighbors. Using Voronoi Tesselation, $\sim$2% of irreversibly rearranging particles are identified as initially having 6 nearest neighbors. Finally, when using r_c derived from g_{LL}, g_{ALL}, and g_{SS} for each type of neighboring pair, $\sim$3% of irreversibly rearranging particles are identified as initially having 6 nearest neighbors.

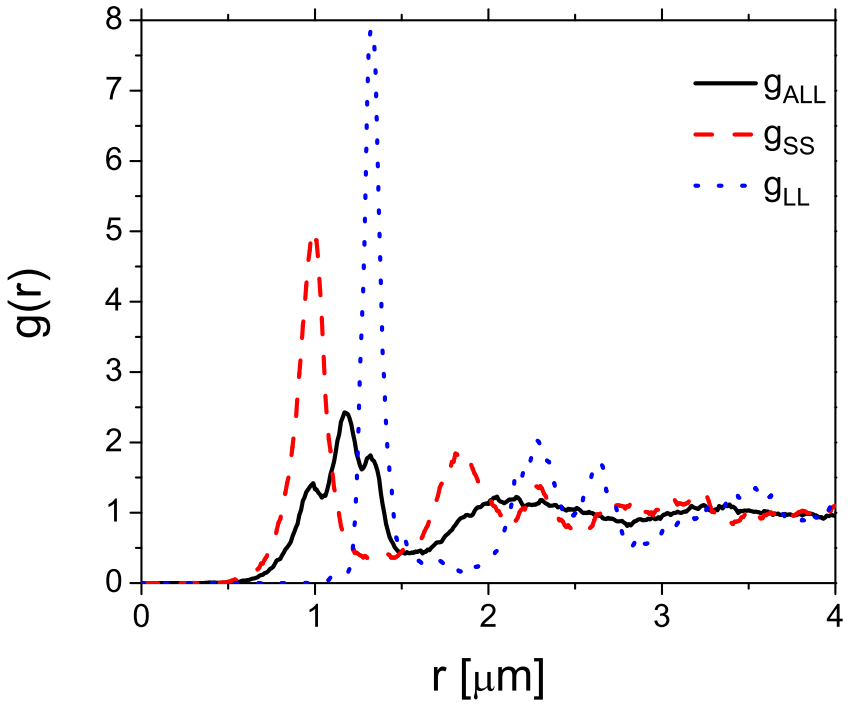

Figure 4.7: The pair correlation function for all particles (g_{LS} - solid line), large particles only (g_{LL} - dotted line), and small particles only (g_{SS} - dashed line).

Both large and small particles exhibit the same trend. The average CN for large particles is 6.1, while the average CN for small particles is 5.8. Large particles, on average, have 3.7 small

neighbors; small particles have on average 3.5 small neighbors. The number of particles with CN = 4 or 5 decreases (for both large and small particles), and the number of small particles with CN = 7 decreases as well. The number of large particles with CN = 7 increases slightly, as predicted by [79].

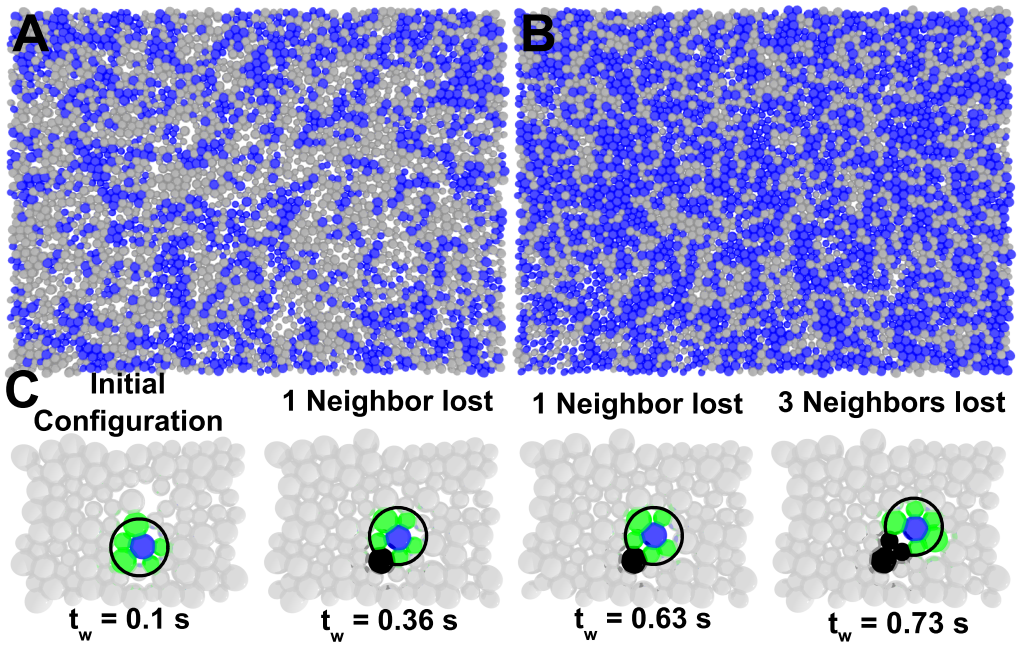

Figure 4.8: A: Snapshot of colloidal glass immediately after the quench, at t_w = 0.03 s. Particles with six nearest neighbors are plotted in blue. B: Snapshot of aged colloidal glass long after the quench, at t_w = 10,000 s. Particles with six nearest neighbors are plotted in blue. C: Example of an irreversible rearrangement that finishes at t_w = 0.67 s. The irreversibly rearranging particle is blue, its nearest neighbors are green, and nearest neighbors it loses are black. The circle represents the cutoff distance that defines nearest neighbors.

We found that $\frac{N_6}{N_{tot}}$, where N_6 is the number of particles with CN = 6 and N_{tot} is the total number of particles, increases from ∼0.48 to ∼0.59 during aging. Both large and small particles exhibit the same trend. The average CN for large particles is 6.1, while the average CN for small particles is 5.8. Large particles, on average, have 3.7 small neighbors; small particles have on average 3.5 small neighbors.

The spatial distribution of locally ordered configurations was studied, and clusters of particles with CN = 6 were identified by connecting nearest-neighbor pairings. We then identified the largest cluster of particles with CN = 6 at each t_w (Fig. 4.9 B). At t_w = 0.03 seconds, 20% of the particles with CN = 6 are in the largest cluster, at t_w = 0.43 seconds, 80% of the particles with CN = 6 are in the largest cluster and it percolates across the entire field of view (80 μm), and at t_w = 10,000 seconds, almost 100% of the particles with CN = 6 are in the largest cluster. (Recall, only 15 IRs occur after t_w = 0.4 seconds.) This large cluster of particles with CN = 6 is evident in Fig. 4.8 B.

The number of particles in clusters with CN = 6 increases from 370 particles to 2150 particles, as described in the main text. The radius of gyration of these clusters grows from $\sim$6 μm to $\sim$20 μm (Fig. 4.3). However, because the cluster percolates across the system at t_w = 0.43 seconds, the radius of gyration becomes less meaningful.

The degree of local order is also characterized by the average bond orientational order parameter [64], $\psi_6 = \frac{1}{N_{tot}CN} \sum_{j=1}^{N_{tot}} \sum_{k=1}^{CN} e^{i6\theta_{jk}}$. Here θ_{jk} is the angle between the x-axis and the j-k bond between particles j and k; CN is the coordination number of particle j, and N_{tot} is the total number of particles. ψ_6 is plotted in Fig. 4.9 C, wherein it is apparent that bond orientational order increases with t_w, consistent with previous work [88, 168].

Correlations of ψ_6 in space are constructed, yielding the correlation function $g_6(r{=}|\mathbf{r}_i{-}\mathbf{r}_j|) = \langle \psi_{6i}^*(r_i)\psi_{6j}(r_j)\rangle$. We fit the envelope of g_6(r) to an exponential (e^{-r/ξ_6}) in order to extract a correlation decay length ξ_6 for orientational order (Fig. 4.9 D) [66, 88, 168]. Initially, ξ_6 is $\sim$0.75

D_S, where D_S is the diameter of the *small* particles. Thus, immediately after the quench, the bond orientational order of a particle typically has minimal relation to that of its neighbor. However, after 10,000 seconds, ξ_6 increased to $\sim D_S$. After aging, particles typically acquire a similar amount of orientational bond order as their nearest neighbors. Taken together, the increase in N_6, ψ_6, and ξ_6 suggest that short-range order increases during aging. Thus the dramatic structural and dynamic variation that occurs during aging clearly demonstrates that particles with short-range order are more stable than particle configurations with CN $\neq$ 6, in agreement with Tanaka and co-workers [158], as well as with other theories that emphasize the importance of local structure [108, 160].

4.7 Packing Fraction Dependence

The aging experiment was done for 5 different area fractions. ϕ_A is calculated based on an effective particle diameter as the distance where the inter-particle potential is 1kBT at each final temperature. For the soft NIPA particles employed in the present study, the effective diameter is typically 10% smaller than the hydrodynamic diameter measured by dynamic light scattering. N_6, ψ_6, ξ_6, N_{6C}, the fraction of irreversibly rearranging particles that initially have CN = 6 (N_{6IR}), and the average size of clusters of fast particles that contain an irreversibly rearranging particle after t_w = 1,000 s are plotted in Fig. 4.10. The static structural quantities are weakly correlated with ϕ_A, typically exhibiting more short-range order as area fraction increases. N_6 and ψ_6 both increase by $\sim$10% as ϕ_A increases from 0.81 to 0.84. However, the orientational order decay correlation length χ_6 changes by $\sim$26%. Thus, while the samples only gain a little

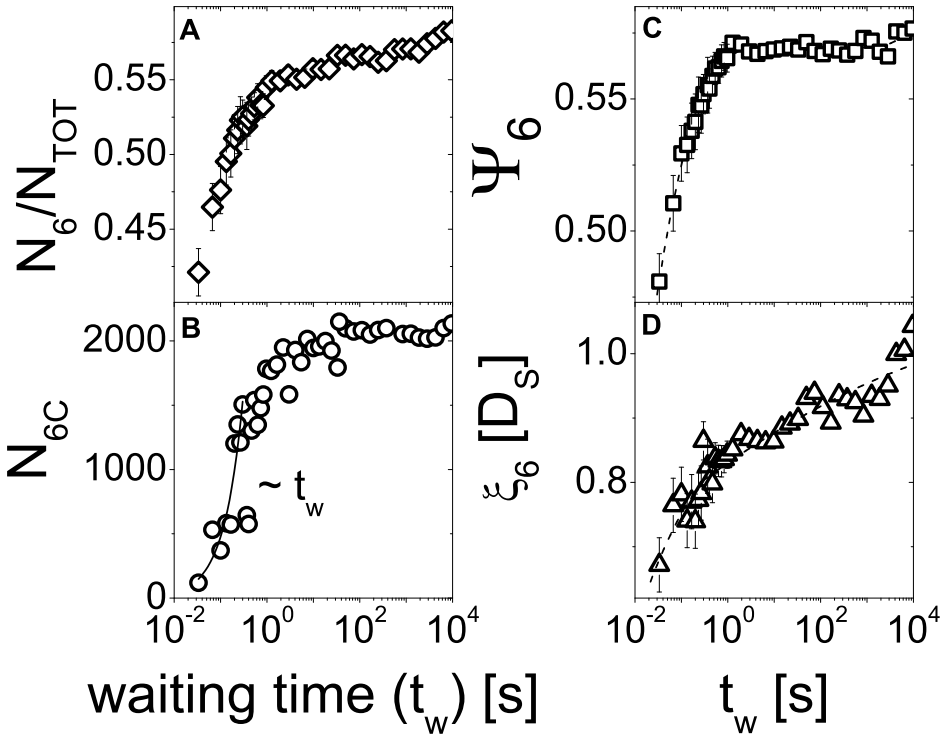

Figure 4.9: A: $\frac{N_6}{N_{tot}}$, the fraction of particles with a coordination number of 6 versus t_w. B: N_{6C}, the number of particles in the largest cluster of particles with 6 nearest neighbors versus t_w. C: Bond orientational order parameter, ψ_6 versus t_w. D: Orientational order correlation decay length ξ_6, extracted from g_6, versus t_w.

more short-range order, the amount of orientational order a particle has becomes more correlated with the amount of orientational order its neighbors have. Irreversible rearrangements have a stronger ϕ_A dependence than static structural quantities do. N_{6IR} is $\sim$500% larger at ϕ_A = 0.81 than it is at ϕ_A = 0.84. Thus, while the fraction of particles with short-range order only increases moderately, particles with short-range order become significantly more stable. The average number of particles in clusters of fast particles, containing a particle undergoing an IR increases with ϕ_A, from $\sim$70 particles at ϕ_A = 0.81 to $\sim$100 particles at ϕ_A = 0.84. This is expected due to the Adam-Gibbs hypothesis [3], as well as previous experiments [12, 169] and simulations [95].

4.8 Summary

To summarize, heterogeneous glass dynamics are governed by domains of fast particles coupled to *irreversible rearrangements*. As a glass ages, the motion of more particles is required to accompany these irreversible rearrangement events, thus making relaxation more difficult to achieve and slowing dynamics. In addition, the fraction of particles with local crystalline order increases during aging. Particles with local crystalline order are especially stable and unlikely to irreversibly rearrange. These results exhibit a clear connection to the slowing dynamics characteristic of aging, as well as to the heterogeneous dynamics of glasses.

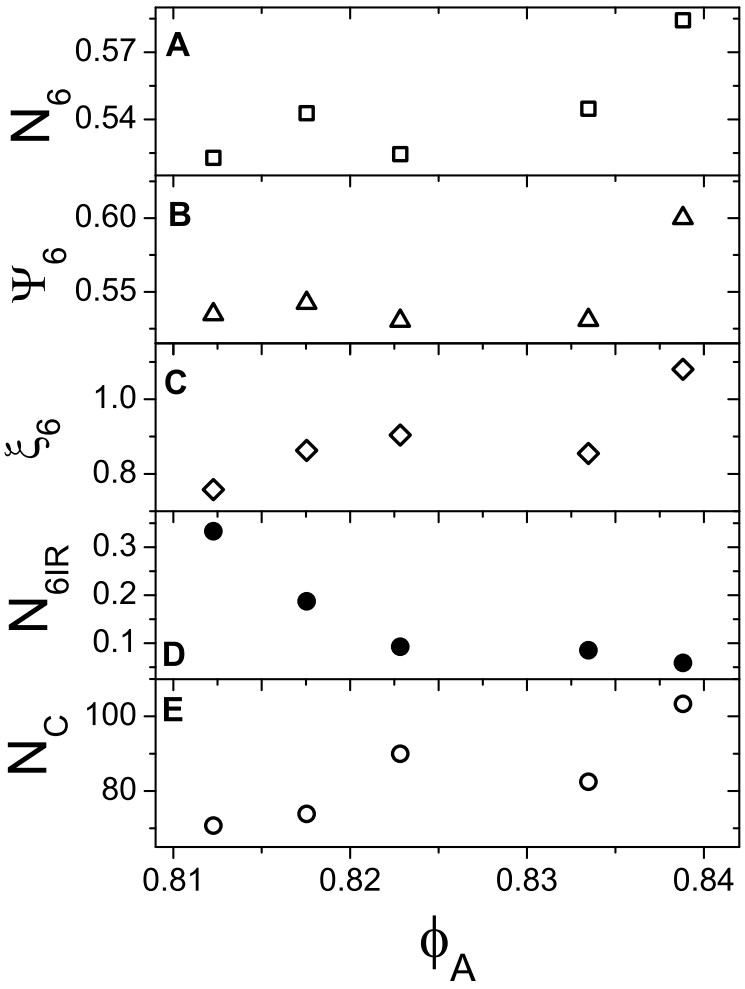

Figure 4.10: A: N_6, the fraction of particles with CN = 6, at t_w = 10,000 s, versus ϕ_A. B: ψ_6 at t_w = 10,000 s, versus ϕ_A. C: ξ_6, the orientational order decay correlation length. D: The fraction of irreversibly rearranging particles that initially have CN = 6. E: The number of fast particles in clusters containing an irreversibly rearranging particle after t_w = 1,000 s.

4.9 Future Directions

These experiments point towards a number of open questions. For example, it would be interesting to compare rearrangement events during aging to rearrangements that contribute to the particle relaxation. This would allow us to determine if IRs move the system towards equilibrium, or if they are the events that comprise equilibrium particle relaxation. To facilitate such a comparison, we could quench to a lower packing fraction which will age to completion. Initially, the MSD will age like in the data presented in this chapter, but eventually the MSD will stop changing. If the particle relaxation time is within the experimental window (~ 100 seconds), we can directly compare the rearrangements that occur after aging to the rearrangements that occur during aging.

Chapter 5

Observation of the Disorder-Induced Crystal-to-Glass Transition

5.1 Introduction

Disorder plays a critical role in traditional melting and freezing phenomena and in the formation of glasses. Melting from crystal-to-fluid, for example, is a sharp transition accompanied by loss of orientational and translational order and by a dramatic decrease in flow resistance and rearrangement timescale [123]. By contrast, orientational and translational order do not change significantly at the liquid-to-glass transition, even as viscosity and rearrangement timescale diverge [164]; nevertheless frozen-in residual disorder is critical for glass formation. An interesting, less-studied but closely related problem [51, 65, 69, 87, 88, 122, 135, 139, 140, 160, 187] concerns the role played by frustration and disorder in driving the transformation of a crystal to a glass. Herein we describe experiments which explore this transition, from crystalline solid

to glass as a function of quenched disorder. The resultant glassy phases acquire typical properties such as dynamic heterogeneity [13, 87, 88, 138, 169] and disorder, but the crystal-to-glass transition is quite sharp, exhibiting features often associated with melting.

Investigations of glass transitions and structural arrest are of broad interest, in part because the new concepts thus-generated affect understanding of a wide variety of materials across a wide swath of scientific communities [13, 87, 88, 125, 169, 174, 191], including molecular [149], colloidal [169], granular [92], and polymeric [74] glasses. The experiments reported in this contribution relate closely to studies exploring how polydispersity prevents crystallization [7, 8, 49, 96, 115, 144, 175]. Our investigation, however, differs from the above in important ways; single-particle spatial resolution, for example, permits quantitative exploration of orientational order and dynamic heterogeneity as a function of packing fraction and disorder across the crystal-glass transition.

5.2 Methods and Materials

The experiments employ temperature-dependent nearly-hard-sphere binary colloidal suspensions composed of two particle sizes with substantially different diameters [181, 191]. The number fraction of the smaller diameter 'dopant' particles is varied from 0.0 to 0.5, and the area fraction of the two-dimensional ($2D$) suspension is varied from $\sim$0.75 to $\sim$0.90 at each dopant concentration. This approach enables us to trace sample evolution as function of increasing quenched disorder at fixed area fraction. Structural correlations associated with orientational order and dynamic correlations associated with particle rearrangements are measured. The path from crystal to glass is marked by a sharp drop in structural correlations and a sudden

jump in dynamical correlations. The crystal-glass transition bears structural signatures similar to the crystal-fluid transition [66, 123]: the orientational order correlation function changes form abruptly from quasi-long-range to short-range at the transition point, and the orientational order susceptibility exhibits a maximum at the transition point. A similarly sharp transition from homogeneous to heterogeneous dynamics accompanies these structural changes; in particular, domains of correlated particle rearrangements (i.e., dynamic heterogeneity) appear to turn-on suddenly, and a dynamic correlation length-scale increases sharply from $\sim$2 to $\sim$6 particle diameters across the transition point. The crystal-to-glass transition is thus measured to differ from the liquid-to-glass transition in qualitative and quantitative ways.

Binary mixtures of repulsive particles have been used as model glasses in experiment [6, 110, 181, 191] and simulation [79, 95, 125]. The present experiment employs aqueous suspensions of micron-size poly(N-isopropyl acrylamide) microgel colloidal spheres (i.e. NIPA particles), whose diameters increase as temperature is reduced [132, 142]. The particles are very similar to those used in recent phase transformation experiments and are described therein [4, 66, 68, 147, 176, 181, 191]. A binary mixture of NIPA particles is sandwiched between two glass cover slips, creating a quasi-2D system. The sample consists of a mixture of NIPA spheres with small and large diameters, $D_S = 1.09\ \mu m$ and $D_L = 1.55\ \mu m$, respectively, at temperature $T = 28.0^{\circ}C$. The polydispersity of each particle type is $\sim 3\%$, and the particle interaction potentials are short-range repulsive with a soft tail [66].

We synthesized many bidisperse suspensions with varying small particle number fractions, n_S (i.e. $n_S = 0.00, 0.01, 0.02, 0.04, 0.05, 0.07, 0.10, 0.15, 0.20, 0.28, 0.50$). By adjusting the sample temperature using a microscope objective heater (BiOptechs), the area fraction, ϕ_A, was

readily increased from $\phi_A \approx 0.75$ to $\phi_A \approx 0.90$ with a step size of $\sim$0.01 in ϕ_A. Fig. 5.1 summarizes n_S and ϕ_A in every sample. Trajectories with varying n_S and fixed ϕ_A can be constructed by following a horizontal line across the diagram. Data were collected at each ϕ_A/n_S combination for 3000 seconds at a video rate of 3 frames per second. The field of view was 60 μm by 80 μm and contained $\sim$2000 particles.

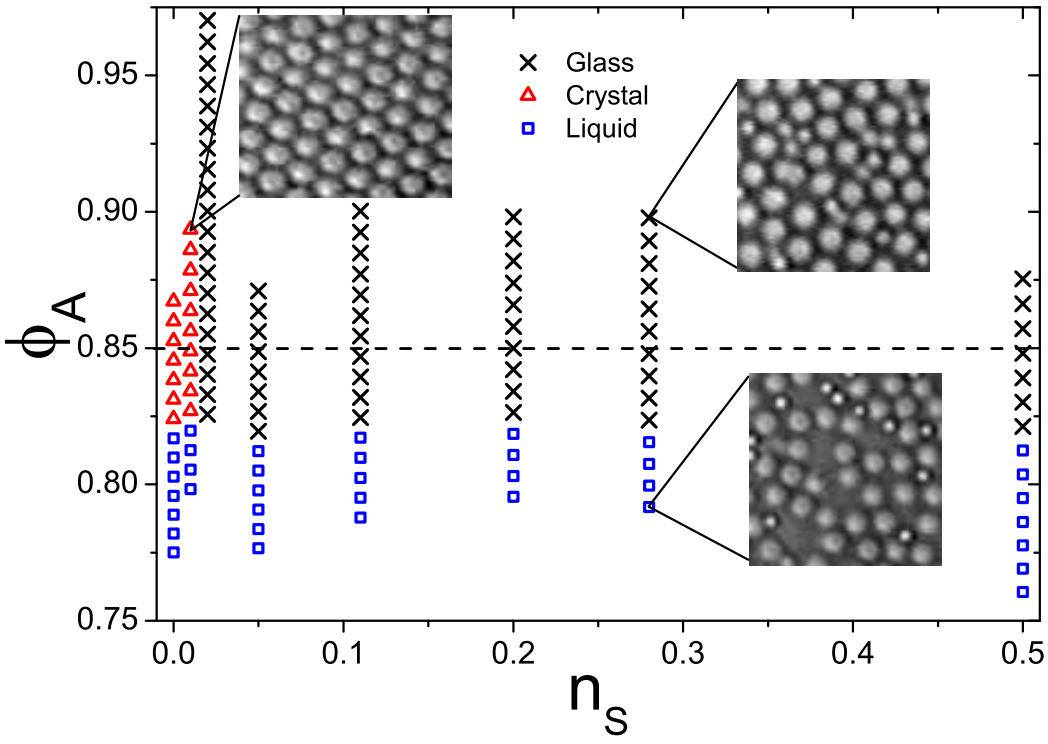

Figure 5.1: Diagram summarizing all collected data. The crystalline phase is plotted with triangles, the glass phase is plotted with crosses, and the liquid phase is plotted with squares. Data presented in the remainder of the paper come from points touching the dashed line. Experimental microscope images of sample sub-regions are displayed from suspensions with n_S = 0.01, ϕ_A = 0.89 (crystal), n_S = 0.28, ϕ_A = 0.90 (glass), and n_S = 0.28, ϕ_A = 0.79 (liquid).

5.3 Structural Quantities

Orientational order is characterized by the bond orientational order parameter: $\psi_6 = \frac{1}{N_{tot}CN}\sum_{j=1}^{N_{tot}}\sum_{k=1}^{CN}|e^{i6\theta_{jk}}|$, where θ_{jk} is the angle between the x-axis and the $j-k$ bond between particles j and k, CN is the coordination number of particle j, and N_{tot} is the total number of particles. The value of ψ_6 at ϕ_A = 0.85 is plotted as a function of n_S in Fig. 5.2 b. As n_S increases from 0, ψ_6 decays as a power law. Additionally, the areal density of free disclinations, N_D, was measured to increase sharply and then stabilize for larger n_S (Fig. 5.2 c). Breakup of dislocations (free and bound) into free disclinations is typically associated with formation of the liquid phase [66, 123].

To characterize the spatial persistence of orientational order, the correlation function $g_6(r{=}|\mathbf{r}_i{-}\mathbf{r}_j|) = \langle\psi_{6i}^*(r_i)\psi_{6j}(r_j)\rangle$, where r_i and r_j are the positions of particles i and j, is derived from the data (Fig. 5.2 d). Two distinct regimes corresponding to crystal and glass are quantitatively identified: $g_6 \sim r^{-\eta}$ (quasi-long-range) for the crystalline state ($n_S < 0.02$) and $g_6 \sim e^{-\frac{r}{\xi_6}}$ (short-range) for the glass state ($n_S \geq 0.02$). By contrast, g_6 changes very little across the liquid-to-glass transition [164].

Temporal fluctuations in ψ_6 are characterized by the susceptibility: $\chi_6 = N_{tot}(\langle(\overline{\psi_6})^2\rangle - \langle\overline{\psi_6}\rangle^2)$ where $\overline{\psi_6}$ is the average of ψ_6 within one image frame ($\overline{\psi_6} = \sum_{i=1}^{N_{tot}}|\psi_6|/N_{tot}$), and angle brackets indicate average over time (see Fig. 5.2 a). To ameliorate finite-size effects, χ_6 is calculated in multiple sub-boxes containing different numbers of particles and is then extrapolated to the infinite size limit [66] (see Online Supporting Material). Interestingly, this susceptibility reaches its maximum at n_S = 0.02, the same value of n_S that marks the change from quasi-long-range orientational order to short-range orientational order (i.e. the dashed line in Fig. 5.2 a-c).

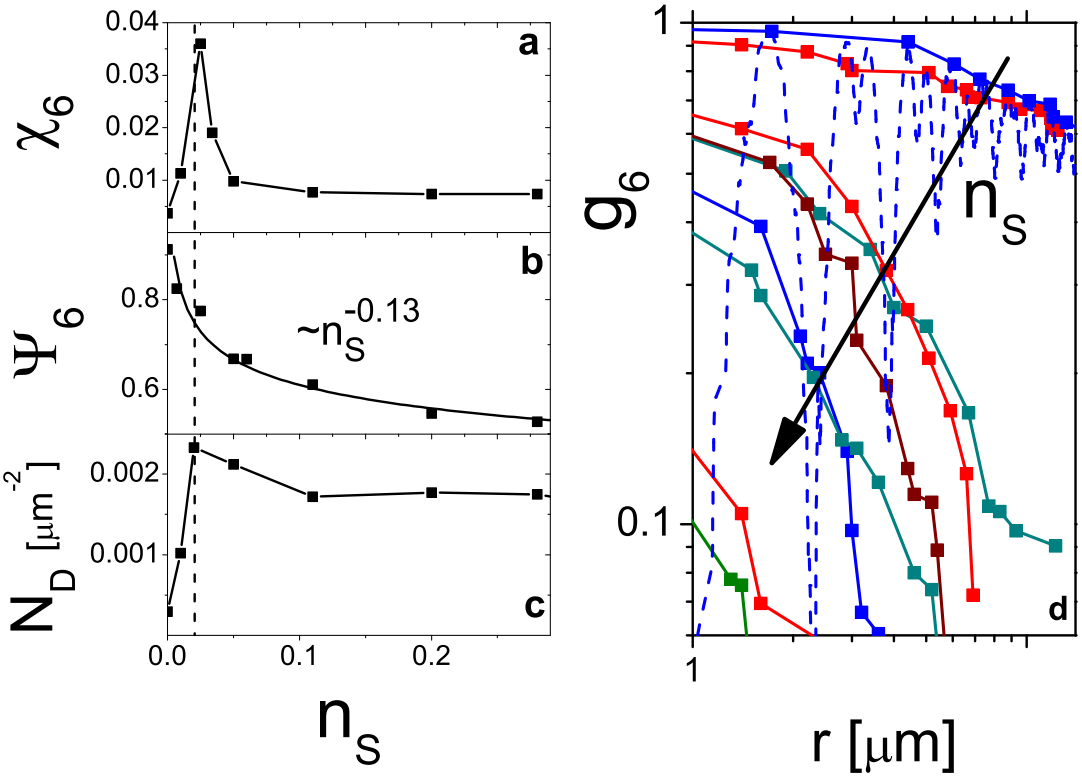

Figure 5.2: a: The bond orientational order parameter (ψ_6) susceptibility, χ_6, versus n_S, at area fraction ϕ_A = 0.85. The dashed line marks n_S = 0.02, the point where χ_6 reaches its maximum value. The solid line guides the eye. b: ψ_6 versus n_S, at area fraction ϕ_A = 0.85. The solid line is a power law fit. c: Free disclination density, N_D, the number disclinations per μm^2, versus n_S at ϕ_A = 0.85. The solid line guides the eye. d: Envelope of the local maxima of the orientational order spatial correlation functions $g_6(r)$ for n_S = 0.00, 0.01, 0.02, 0.05, 0.11, 0.20, 0.28, 0.50, and packing fraction ϕ_A = 0.85. The complete (oscillating) g_6 is shown for n_S = 0.01 (dashed line).

Thus the variation of both the correlation length and the orientational order susceptibility, χ_6, suggest a sharp transition between crystal (ordered) and glass (disordered) states as a function of quenched disorder.

To ameliorate finite-size effects, we calculated χ_6 in different size subboxes within the sample and then extrapolated to the infinite size limit, thus attaining the thermodynamic limit. The χ_6 of small subboxes were noisy due to poor statistics; thus before calculating χ_6, we randomized each particles position within the box while leaving its ψ_6 untouched. Position randomization did not affect χ_6 in the largest box, but smoothed χ_6 in subboxes, averaging over spatial fluctuations while preserving time fluctuations. χ_6 is plotted in Fig. 5.3 for N = 2000 particles and for the N$\rightarrow \infty$ limit. Without this extrapolation, χ_6 is noisier, but the transition point is still resolved.

The sharp decrease in orientational order correlation length, the peak in χ_6 (ψ_6 susceptibility), and the increase in defects (free disclinations) associated with the liquid state are all reminiscent of the crystal-liquid transition [66,123], suggesting a distinct transition from crystal-to-glass via increasing quenched disorder [51,122]. This result stands in contrast to the transition from liquid-to-glass, where changes in structural correlations are not observed [164]. Thus the present system appears to be an excellent new model for study of the relationship between structural order and glass dynamics (e.g., dynamic heterogeneity).

5.4 Dynamic Quantities

To explore dynamical variations with n_S, we first compute the two-point self correlation function: $Q_2(d_L, \Delta t) = \frac{1}{N_{tot}} \sum_{i=1}^{N_{tot}} exp(-\frac{\Delta r_i^2}{2d_L^2})$ [20]. Here d_L is a pre-selected length scale to be

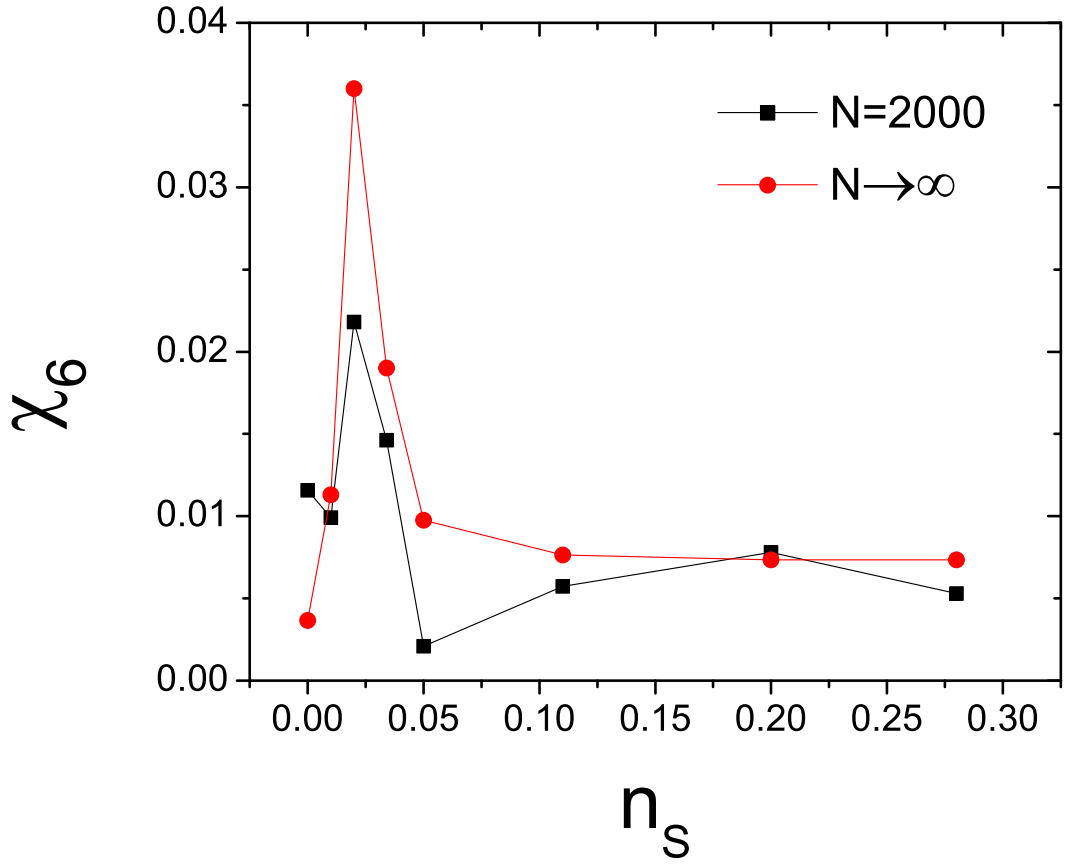

Figure 5.3: χ_6, the ψ_6 susceptibility, calculated for N = 2000 (squares) and extrapolated to N$\rightarrow \infty$ (open circles).

probed and Δr_i is the distance particle i moves in time Δt. If a particle moves a distance smaller than d_L, Q_2 will be close to 1; if a particle moves a distance greater than d_L, Q_2 will be close to 0. Plots of Q_2 for d_L = 0.05 μm are given in Fig. 5.4 a. For the crystalline states ($n_S < 0.02$), Q_2 plateaus and does not decay within the experimental window. Conversely, for glass states, Q_2 decays within the observed time frame, due to the rearrangement of particle cages as the particles seek new configurations. This effect was first noted in [65].

Small particles are slightly, but not significantly more mobile than large particles at long times. For example, Q_2 is shown in Fig. 5.5 for ϕ_A = 0.85 and n_S = 0.18 for three different values of d_L.

The emergence of domains of correlated rearrangements is central to many different properties of glasses [13, 87, 88, 138, 169]. This so-called dynamic heterogeneity is characterized by temporal fluctuations in Q_2, and these fluctuations are commonly quantified by the dynamic susceptibility [2, 13, 20], $\chi_4(d_L, \Delta t) = N_{tot}(\langle Q_2(d_L, \Delta t)^2\rangle - \langle Q_2(d_L, \Delta t)\rangle^2)$, as a function of lengthscale d_L and timescale Δt. Rather than selecting arbitrary length and time scales, χ_4 is calculated for all relevant values of d_L and Δt (shown in Fig. 5.6 for $n_S = 0.16$). From this plot, the value of d_L that maximizes χ_4 can be selected. The variation of χ_4 with n_S, at the value of d_L that maximizes the peak in χ_4, is plotted in Fig. 5.4 b for ϕ_A = 0.85 and n_S = 0.0, 0.01, 0.025, 0.07, and 0.16. For $n_S > 0.02$, χ_4 exhibits a peak similar to that found in previous works [1, 2, 13, 20, 59]. Conversely, χ_4 is small and flat for samples with $n_S < 0.02$, as expected for crystalline systems.

The maximum value of χ_4 (i.e. χ_4^*) is plotted in Fig. 5.7 a for each n_S at ϕ_A = 0.85. In crystalline suspensions, χ_4^* is small ($\sim$1). Once n_S is increased beyond 0.02, however, χ_4^* jumps

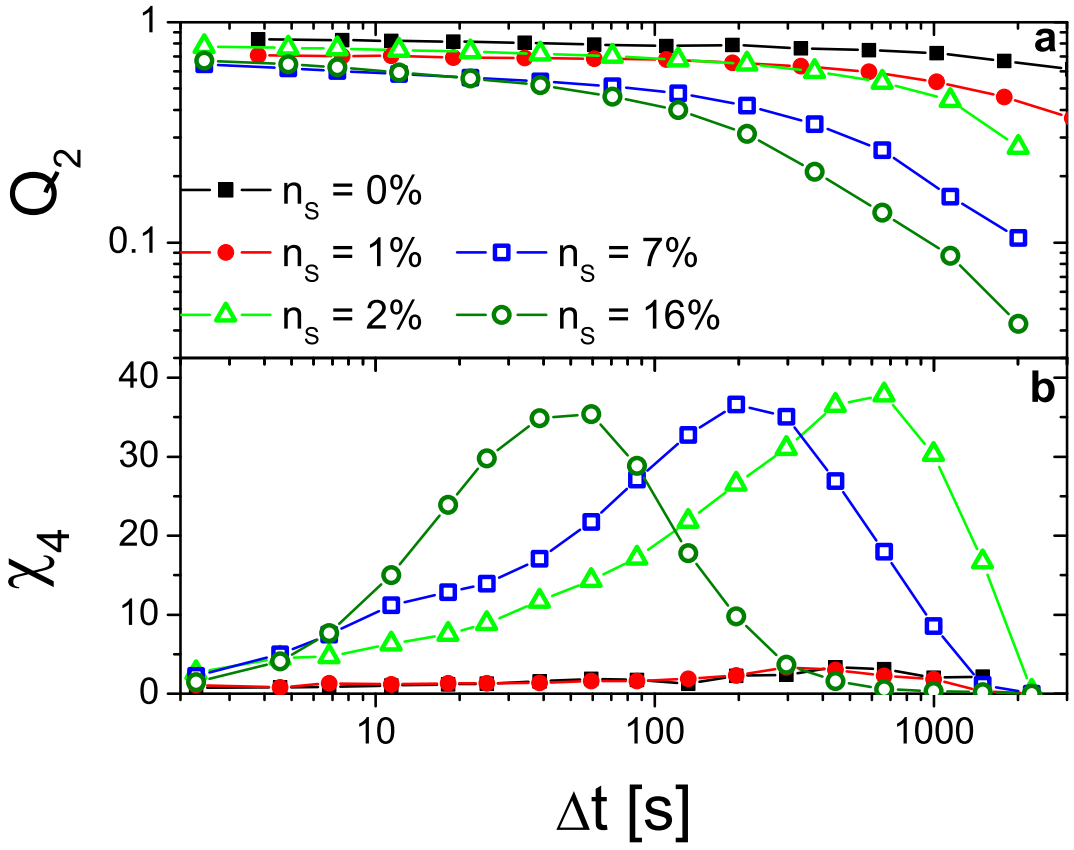

Figure 5.4: a: The two-point-correlation function, Q_2, is plotted versus Δt, for d_L = 0.05μm and for n_S = 0.00 (solid squares), 0.01 (solid circles), 0.02 (open triangles), 0.07 (open squares), 0.16 (open circles). b: The four-point dynamic susceptibility, χ_4, is plotted versus Δt for the same values of n_S as in a; the value of d_L is chosen to maximize peak height.

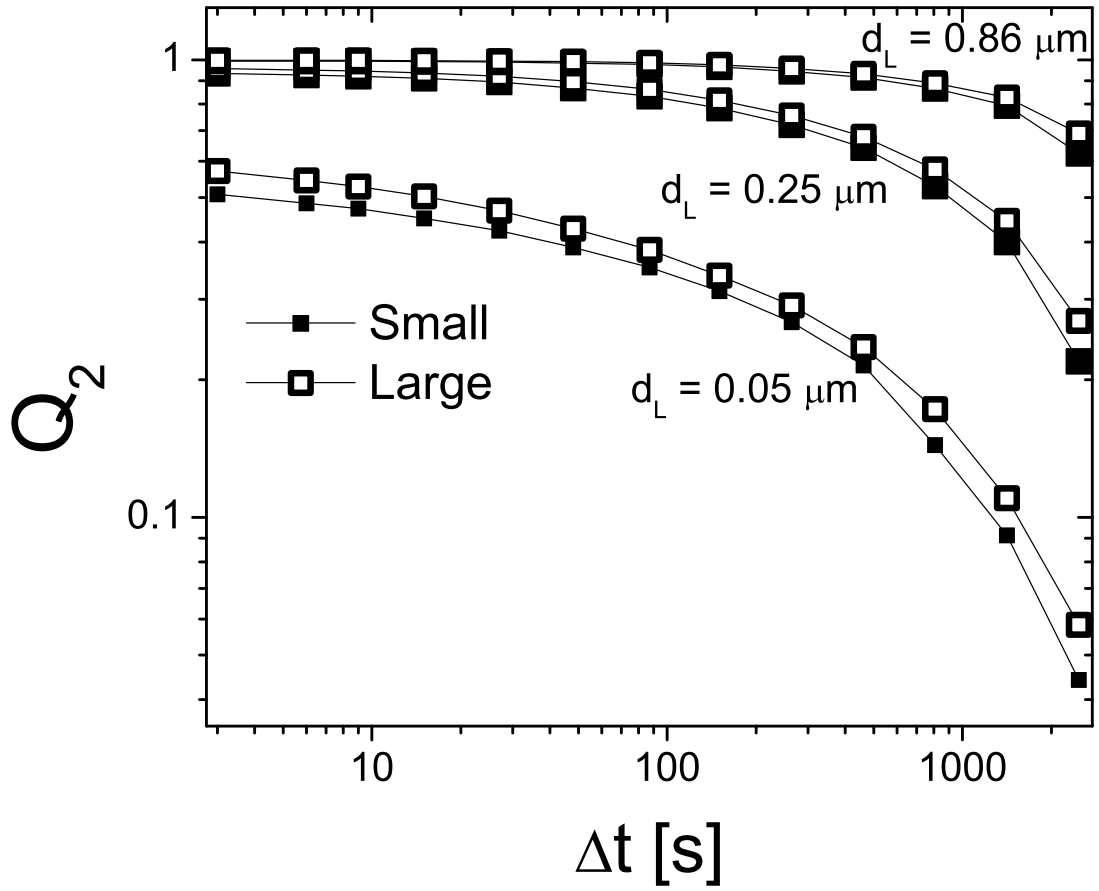

Figure 5.5: Q_2 versus Δt for d_L = 0.05, 0.25, and 0.86 μm for large particle (open squares) and small particles (solid squares) at ϕ_A = 0.85 and n_S = 0.16.

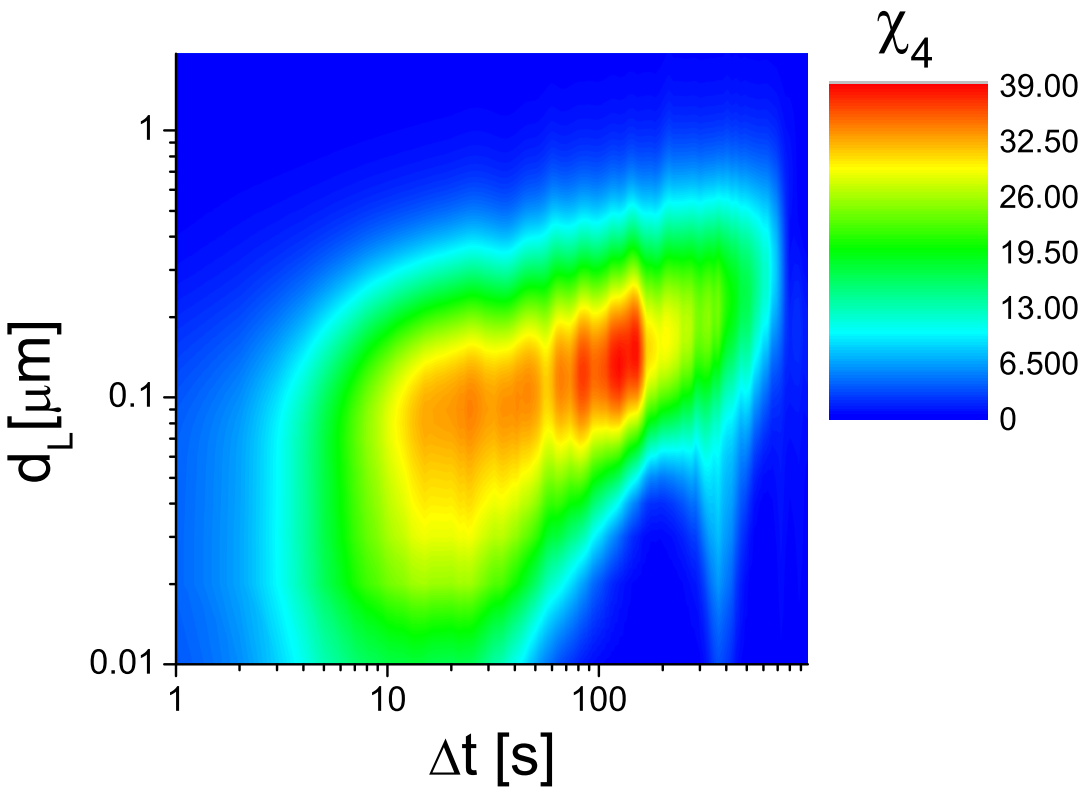

Figure 5.6: χ_4 versus probed lengthscale, d_L, and timescale, Δt for ϕ_A = 0.85 and n_S = 0.16.

discontinuously to ∼35. As n_S is increased still further, χ_4^* remains fairly constant. This sharp change is absent in the liquid-glass transition [2, 13]. For comparison we plot χ_4^* across the liquid-glass transition in this same experimental system as a function of particle area fraction at fixed dopant concentration $n_S = 0.25$ (i.e., along the vertical line with $n_S = 0.25$ in Fig. 5.1); χ_4^* increases continuously as packing fraction is increased (Fig. 5.7 b), similar to [2, 13].

χ_4^* can be related to the number of particles participating in a dynamically heterogeneous event [1]. The sudden variation of χ_4^* is thus indicative of a sudden increase in the size of domains of correlated rearranging particles as the system evolves from crystal to glass. When too much quenched disorder exists in the sample for crystallization to occur, the suspension is pushed out of equilibrium as it searches for a configuration to minimize its free energy. These search pathways are constrained by the suspension's large packing fraction, and rearrangements must occur in a collective manner. Interestingly, once in the glass phase, further increasing n_S moves χ_4^* to larger values of d_L (Fig. 5.7 c), implying relaxation events are more effective. However, χ_4^* itself does not increase significantly, thus implying the degree of quenched order has little effect on the domain size of collective rearrangements (see Online Supplemental Material for further discussion).

To further characterize the domain size of the correlated rearrangements, we derived spatial correlations of $1-Q_2^*$, yielding the rearrangement spatial correlation function: $g_{Q_2}(r{=}|\mathbf{r}_i{-}\mathbf{r}_j|) = \langle(1-Q_{2i}^*(r_i))(1-Q_{2j}^*(r_j))\rangle$. Here Q_2^* is calculated for values of d_L and Δt that maximize χ_4, and thus dynamic heterogeneity. Note that correlations of $1-Q_2^*$ relate to *rearranging* particles, i.e. particles moving farther than d_L. These correlation functions are readily fit by decaying exponentials ($g_{Q_2} \propto exp(-\frac{r}{\xi_{Q_2}})$), and a correlation length, ξ_{Q_2}, is thus readily extracted (Fig.

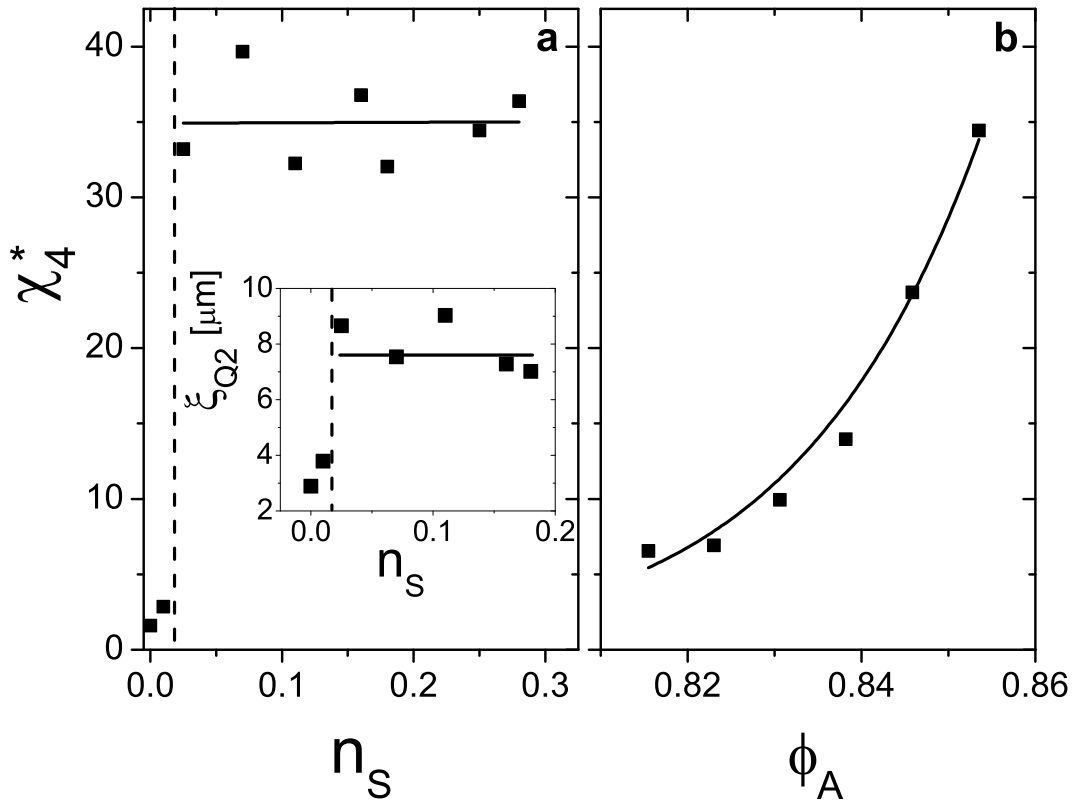

Figure 5.7: a: The maximum value of χ_4, χ_4^*, plotted versus the fraction of small particles, n_S. The solid line is a linear fit, to guide the eye. The dashed line marks n_S = 0.02. Inset: Rearrangement correlation length, ξ_{Q_2}, versus n_S. The solid line is a linear fit to guide the eye. The dashed line marks n_S = 0.02. b: χ_4^* plotted versus ϕ_A for n_S = 0.25. The solid line is a power law fit to guide the eye. c: The maximum value of χ_4 is plotted as a function of d_L for four values of n_S.

5.7 a inset). For crystalline samples ($n_S < 0.02$), $\xi_{Q_2} \sim 2D_L$, implying that when particles move large distances, only their nearest neighbors move large distances. For glass samples ($n_S > 0.02$), $\xi_{Q_2} \sim 6D_L$, implying that when particles move large distances, they do so in a correlated manner involving many particles. The size of ξ_{Q_2} jumps sharply at n_S = 0.02, along with the discontinuous increase in χ_4^* (during the liquid to glass transition, ξ_{Q_2} follows the same continuous trend as χ_4^*). Thus the onset of dynamic heterogeneity appears nearly discontinuously.

5.5 Summary

The *dynamical* transition from crystal to glass is thus characterized by a discontinuous jump in χ_4^*, the maximum value of the dynamic susceptibility, and a discontinuous increase in spatial correlation decay length from $\sim 2D_L$ to $\sim 6D_L$. These results stand in contrast to the liquid-glass transition, during which dynamics change relatively more slowly and continuously. The rapid onset of glass dynamics occurs at the same value of n_S as the structural transition from crystal to glass. In other words, dynamic heterogeneity appears simultaneously with the disappearance of quasi-long-range orientational order. To conclude, while the liquid-to-glass transition is somewhat ambiguous and often difficult to define, the crystal-to-glass transition with increasing quenched disorder appears sharp and unambiguously defined.

5.6 Future Directions

In this work, we explored the effects of holding the diameter ratio constant and varying the small particle fraction. Future experiments could investigate the crystal-to-glass transition by doing the

opposite, i.e., holding the small particle fraction constant and varying the diameter ratio. Along this trajectory, the crystal-to-glass transition might be less sharp.

It would also be interesting to repeat these experiments in three-dimensional samples. Crystallization is highly dependent on dimensionality, so the nature of the crystal-to-glass transition likely depends on dimensionality as well. For example, in three-dimensions, the phase transition is first order, and there is a large fluid-crystal coexistence regime that is absent in two-dimensions. Thus, investigating the crystal-to-glass transition in three-dimensions could potentially elucidate the effect of dimensionality on the crystal-to-glass transition.

Chapter 6

Rotational and Translational Phonon Modes in Glasses Composed of Ellipsoidal Particles

6.1 Introduction

Although the "glass transition" occurs in a broad array of disordered systems, including molecular [5], polymer [78], granular [2], and colloidal glasses [169], much of the physics of granular and colloidal glasses has been derived from investigation of the simplest realization, namely spheres. The constituent particles of many relevant glasses, however, are anisotropic in shape or have orientation-dependent interactions; such anisotropies are believed to affect many properties of glasses [44, 45, 82, 97, 114, 152]. Thus, exploration of glasses composed of anisotropic particles holds potential to uncover new consequences for both the physical mechanisms of the glass

transition and for materials applications [170].

In glasses composed of frictionless spherical constituents, rotations of the spheres do not cost energy. Rotational modes therefore correspond to zero-frequency phonon excitations in the harmonic approximation. For anisotropic constituents, however, rotations are more energetically costly and can couple to translations. Glass vibrational properties, including the phonon density of states, are therefore dependent on the major/minor-axis aspect ratio of the constituent particles. Simulations of disordered systems with aspect ratios marginally greater than 1.0, for example, find low energy rotational modes that are largely decoupled from translational modes [113, 189]; apparently, when particles rotate in such systems, neighboring particles rotate but their positions remain essentially unperturbed.

In this section, we experimentally study glasses composed of ellipsoidal particles with aspect ratios, α, ranging from $1.0 - 3.0$. By extending techniques from recent papers [23, 57, 58, 90] to rotations, we employ video microscopy to derive the phonon density of states of corresponding "shadow" ellipsoidal glasses with the same geometric configuration and interactions as the experimental colloidal system but absent damping [23]. We find the spectra and character of vibrational modes in these disordered media to be highly dependent on particle aspect ratio and particle aspect ratio distribution. For glasses composed of particles with small median aspect ratios of ~ 1.1, the lower-frequency modes are almost completely rotational in character, while higher-frequency ones are translational. In glasses of particles with larger aspect ratios (~ 3.0), significant mixing of rotations with translations is observed. In contrast to numerical findings for zero-temperature systems [113, 189], we find that the very lowest frequency modes for both

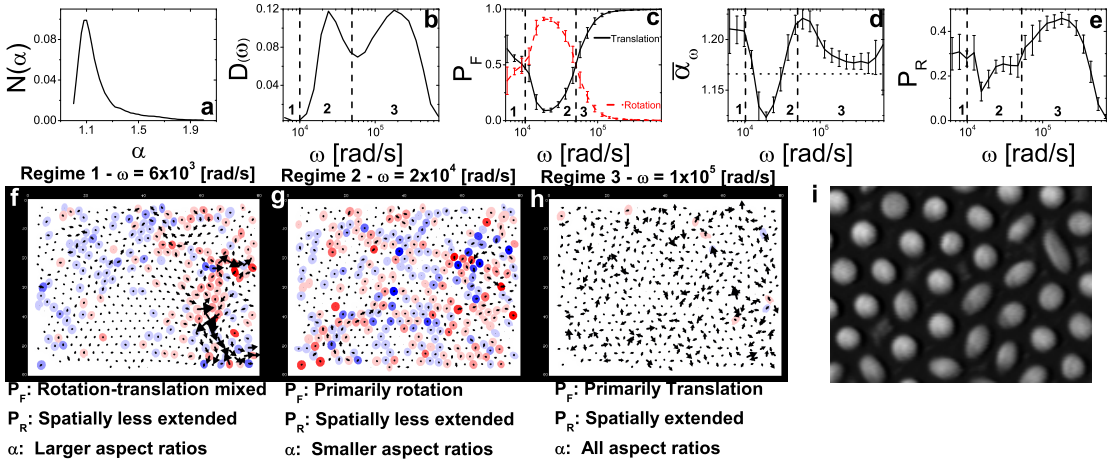

Figure 6.1: a. Distribution of particle aspect ratio, N(α), in samples with peak aspect ratio $\alpha_{Peak} = 1.1$. b. Vibrational density of states. Dashed lines separate 3 distinct regimes corresponding to modes in the vector plots displayed in f-h. c. Translational (solid black line) and rotational (dashed red line) contributions to participation fraction (P_F) plotted versus frequency ω. d. Participation fraction-averaged aspect ratio, $\bar{\alpha}_\omega$, plotted versus frequency ω. e. Participation ratio (P_R) plotted versus frequency ω. f-h. Displacement vector plots of eigenmodes from lowest frequency (f) to highest (h). The size of each arrow is proportional to the *translational* displacement of the particle at that position. The color intensity of each particle is proportional to the *rotational* displacement of the particle at that position (with red clockwise, blue counterclockwise, faint color is small rotation). Aspect ratio and frequency are specified below each plot. i. Experimental snapshot.

systems have a mixed rotational/translational character, independent of aspect ratio.

6.2 Materials and Methods

The experiments employ micron-sized polystyrene particles (Invitrogen) stretched to different aspect ratios [21, 52, 72]. Briefly, $3\mu m$ diameter polystyrene particles are suspended in a polyvinyl alcohol (PVA) gel and are then heated above the polystyrene melting point ($\sim 120^\circ\ C$) but below the PVA melting point ($\sim 180^\circ\ C$). In the process, the polystyrene melts, but the PVA gel only softens. The PVA gel is then placed in a vise and stretched. The spherical cavities that contain liquid polystyrene are stretched into ellipsoidal cavities. When the PVA gel cools, the polystyrene solidifies in the distorted cavities, and becomes frozen into an ellipsoidal shape. The hardened gel dissolves in water, and the PVA is easily removed via centrifugation. Each iteration creates $\sim 10^9$ ellipsoidal particles in $\sim 50\mu L$. Experiments are performed on samples stretched to 110% and 300% of their original size (snapshots of experimental particles are shown in Fig. 6.1 i, Fig. 6.5 i). The stretching scheme produces a distribution of aspect ratios with standard deviation $\sim 18\%$. The distribution of aspect ratios is most important for suspensions that are only slightly distorted from their initial spherical shape and therefore have greater propensity to crystallize. The distribution of aspect ratio, $\mathrm{N}(\alpha)$, for suspensions with more spherical particles (Fig. 6.1 a) is peaked at $\alpha_{Peak} = 1.1$, with mean aspect ratio $\bar{\alpha} = 1.2$, but $\mathrm{N}(\alpha)$ also has a long tail extending to aspect ratios as large as $\alpha = 2.0$. A similar plot is shown in Fig. 6.5 a for samples with $\alpha_{Peak} = 3.0$ and $\bar{\alpha} = 3.3$.

Particles are confined between glass plates to quasi-two-dimensional chambers. From separate brightness calibration studies, we estimate the chambers to be no more than 5% larger than the minor axis particle length. In all samples, dynamics are arrested on the particle diameter lengthscale and the spatial correlation functions of orientational order decay exponentially, with an average bond-orientational order parameter of 0.3 (0.03) for $\alpha_{Peak} = 1.1$ (3.0).

6.3 Glasses Composed of Anisotropic Particles

Previous works have noted that the packing fraction at the jamming transition varies with particle shape [44]. In order to characterize how close our samples are to the jamming transition, we slowly evaporated water from the sample chamber. Complete evaporation packs particles at their maximum packing fraction, which is equivalent to the jamming transition for hard particles. We verified this claim for bidisperse mixtures of spheres of size ratio 1.4, where we find $\phi_{A,MAX} = 0.84(1)$, as expected. For ellipsoids with $\alpha_{Peak} = 1.1$, $\phi_{A,MAX} = 0.87(1)$, consistent with [44,45,145], while the sample employed in this paper has $\phi_A = 0.86(1)$. For ellipsoids with $\alpha_{Peak} = 3.0$, $\phi_{A,MAX} = 0.84(1)$, again consistent with [44, 45, 145], while the sample employed in this paper has $\phi_A = 0.83(1)$. Thus both samples are near, but below, the jamming transition, with $\phi_{A,MAX} - \phi_A \approx 0.01$.

As a first step towards elucidation of glass dynamics in these systems, we compute the two-time self-overlap correlation function: $Q_2(d_L, \Delta t) = \frac{1}{N_{tot}} \sum_{i=1}^{N_{tot}} exp(-\frac{\Delta r_i(\Delta t)^2}{2d_L^2})$ (Fig. 6.1 b) [35]. Here d_L is a pre-selected length scale to be probed, N_{tot} is the total number of particles, and $\Delta r_i(\Delta t)$ is the distance particle i moves in time Δt. If a particle moves a distance smaller

than d_L, Q_2 will remain approximately unity; if a particle moves a distance greater than d_L, Q_2 will fall to zero. Notice that for glasses of each aspect ratio, $Q_2(d_L = 1.0\ \mu m)$ decays very little over the experimental timescale, thereby indicating that glass dynamics are arrested at length scales of order the particle-size.

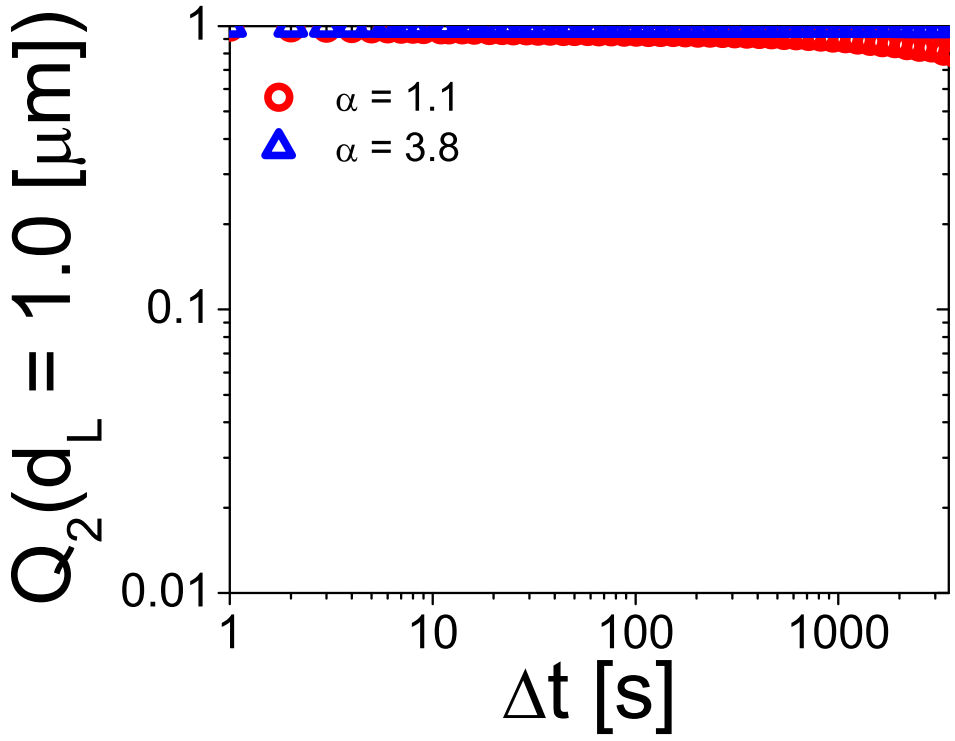

Figure 6.2: The two-point-correlation function, Q_2, which probes self overlap, is plotted versus delay time for ellipsoidal glasses with different aspect ratios. Dynamic arrest is apparent.

To demonstrate the absence of long-range orientational order in these systems, the bond-orientational order parameter, $\psi_6 = \frac{1}{N_{tot}CN}\sum_{j=1}^{N_{tot}}|\sum_{k=1}^{CN} e^{i6\theta_{jk}}|$ and its spatial correlation function $g_6(r{=}|\mathbf{r}_i{-}\mathbf{r}_j|) = \langle\psi_{6i}^*(r_i)\psi_{6j}(r_j)\rangle$ are calculated (Fig. 6.1 c). Here θ_{jk} is the angle between the x-axis and the $j-k$ bond between particles j and k, CN is the coordination number of particle j, and r_i and r_j are the positions of particles i and j. g_6 decays faster in samples with

$\alpha_{Peak} = 3.8$ than it does in samples with $\alpha_{Peak} = 1.1$. However, g_6 decays exponentially in each sample (see exponential fit line in Fig. 6.3), a signature of structural disorder characteristic of glasses (e.g. [159]).

To demonstrate the absence of long-range nematic order in these systems, the nematic order parameter, $S = \sum_{j=1}^{N_{tot}} 2 * cos(\theta_j)^2 - 1$, where θ_j is the angle between the orientation of particle i and the nematic director, and angle brackets represent ensemble averaging, is largely absent. For an isotropic distribution of orientations, S = 0, and for perfectly aligned particles S = 1. The mean value of S in our high aspect ratio samples ($\alpha_{Peak} = 3.0$) is 0.05, and the maximum value of S is 0.11 (Fig. 6.4 a). The mean value of S in samples with $\alpha_{Peak} = 1.1$ is 0.00, and the maximum value of S is 0.25 (Fig. 6.4 b).

6.4 Measurement of Phonon Modes for Anisotropic Particles

We extract vibrational properties by measuring displacement correlations. Specifically, we define $u(t)$ as the $3N$-component vector of the displacements of all particles from their average positions $(\bar{x}, \bar{y})$and orientations $(\bar{\theta})(u(t) = (x(t) - \bar{x}, y(t) - \bar{y}, \theta(t) - \bar{\theta}))$, and extract the time-averaged displacement correlation matrix, or covariance matrix, $C_{ij} = \langle u_i u_j \rangle_t$ where $i, j = 1, ..., 3N_{tot}$ run over particles, positional and angular coordinates, and the average runs over time. In the harmonic approximation, the correlation matrix is directly related to the sample's stiffness matrix, defined as the matrix of second derivatives of the effective pair interaction potential with respect to particle position and angle displacements. In particular, $(C^{-1})_{ij} k_B T = K_{ij}$ where K_{ij} is the stiffness matrix. Experiments that measure C therefore permit us to construct and derive properties of a "shadow" ellipsoidal glass system that has the

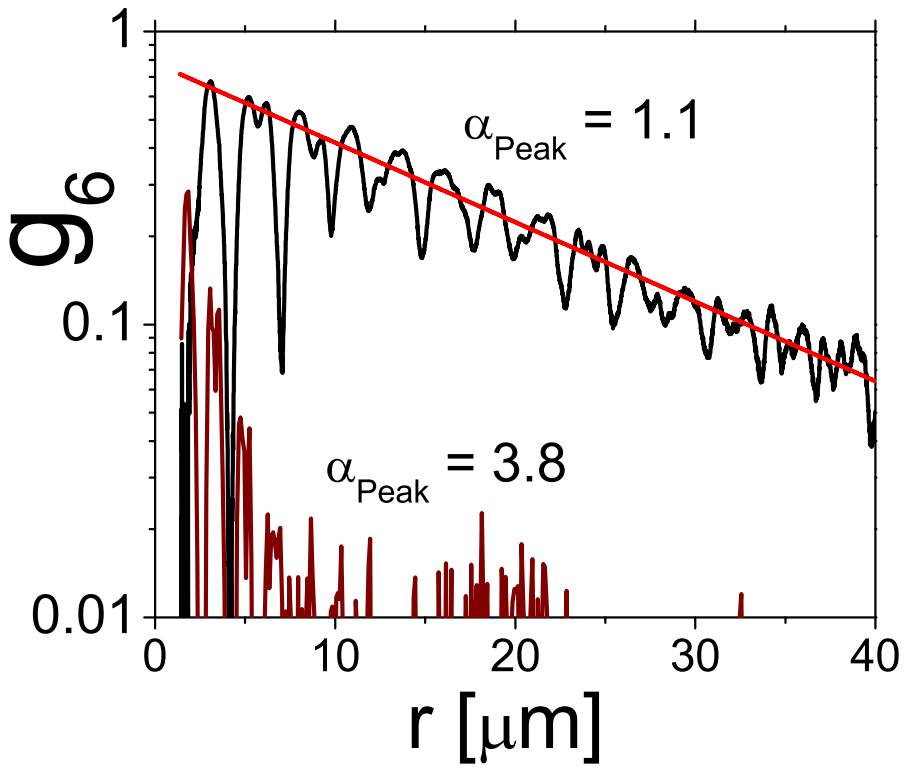

Figure 6.3: Bond orientational order spatial correlation functions, $g_6(r)$, for ellipsoidal glasses with different aspect ratios.

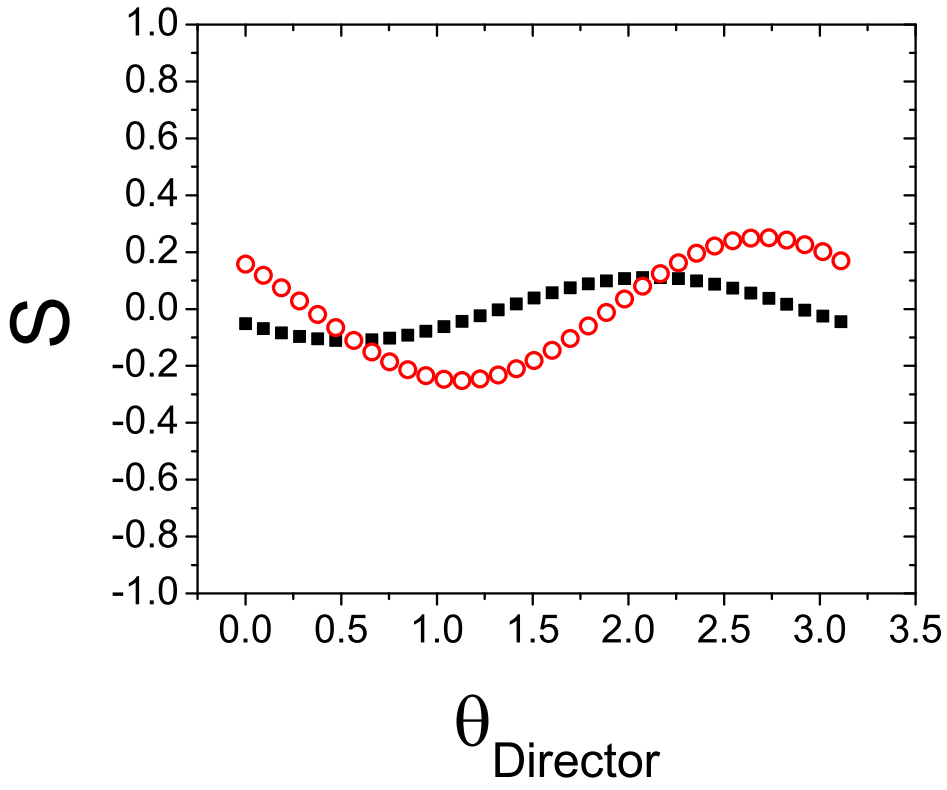

Figure 6.4: The average nematic order parameter, S, as a function of the director angle for samples with $\alpha_{Peak} = 3.0$ (closed squares) and $\alpha_{Peak} = 1.1$ (open circles).

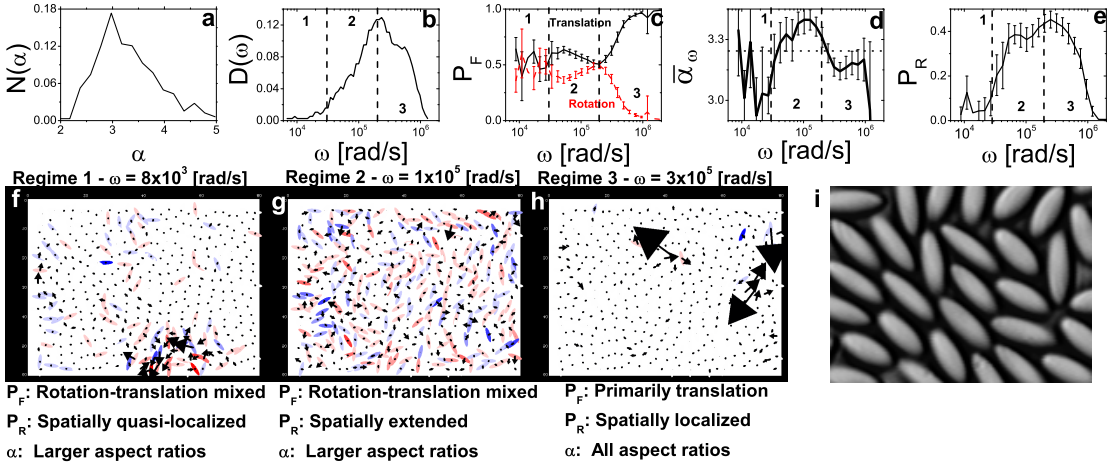

Figure 6.5: a. Distribution of aspect ratio, N(α), in samples with peak aspect ratio $\alpha_{Peak} = 3.0$. b. Vibrational density of states. Dashed lines separate 3 distinct regimes corresponding to modes in the vector plots displayed in f-h. c. Translational (solid black line) and rotational (dashed red line) contributions to participation fraction (P_F) plotted versus frequency ω. d. Participation fraction-averaged aspect ratio, $\bar{\alpha}_\omega$, plotted versus frequency ω. e. Participation ratio (P_R) plotted versus frequency ω. f-h. Displacement vector plots of eigenmodes from lowest frequency (f) to highest (h). The size of each arrow is proportional to the *translational* displacement of the particle at that position. The color intensity of each particle is proportional to the *rotational* displacement of the particle at that position (with red clockwise, blue counter-clockwise, faint color is small rotation). Aspect ratio and frequency are specified below each plot. i. Experimental snapshot.

same static properties as our colloidal system (e.g., same correlation matrix, same stiffness matrix, but no damping) [23]. Following [18], we expect undamped hard particles that repel entropically near but below the jamming transition to give rise to solidlike vibrational behavior on time scales long compared to the collision time but short compared to the time between particle rearrangement events [57, 58]. Thus, the stiffness matrix arising from entropic repulsions is directly related to the dynamical matrix characterizing vibrations, $D_{ij} = \frac{K_{ij}}{m_{ij}}$, where $m_{ij} = \sqrt{m_i m_j}$ and m_i is an appropriate measure of inertia. For translational degrees of freedom $m_i = m$, where m is the particle mass. For rotational degrees of freedom, $m_i = I_i$ represents the particle moment of inertia with respect to axes centered about each particle's center of mass and pointing in the z-direction, $I_i = m(a_i^2 + b_i^2)/2$, where a_i and b_i are the major and minor radii of the ith ellipsoid. The eigenvectors of the dynamical matrix correspond to amplitudes associated with different phonon modes, and the eigenvalues correspond to the frequencies/energies of the corresponding modes. Data were collected over $10,000$ seconds so that the number of degrees of freedom, $3N \approx 2000$, is small compared to the number of time frames of ~ 8000 [23]. Additionally, we find K_{ij} is far above the noise only for adjacent particles, as expected.

The vibrational density of states, $D(\omega)$, is plotted in Fig. 6.1 b for the system with $\alpha_{Peak} = 1.1$. We see that $D(\omega)$ exhibits two distinct peaks. By contrast, zero-temperature simulations find for α sufficiently close to 1 and for sufficiently small systems close enough to the jamming transition, that these peaks split completely [113, 189]. For ellipsoids with $\alpha_{Peak} = 3.0$ (Fig. 6.5 b), on the other hand, $D(\omega)$ has a single peak, consistent with numerical predictions [113, 189]. Thus, the vibrational spectrum of ellipsoids with small anisotropy is significantly different from those of spheres or of ellipsoids of higher aspect ratio.

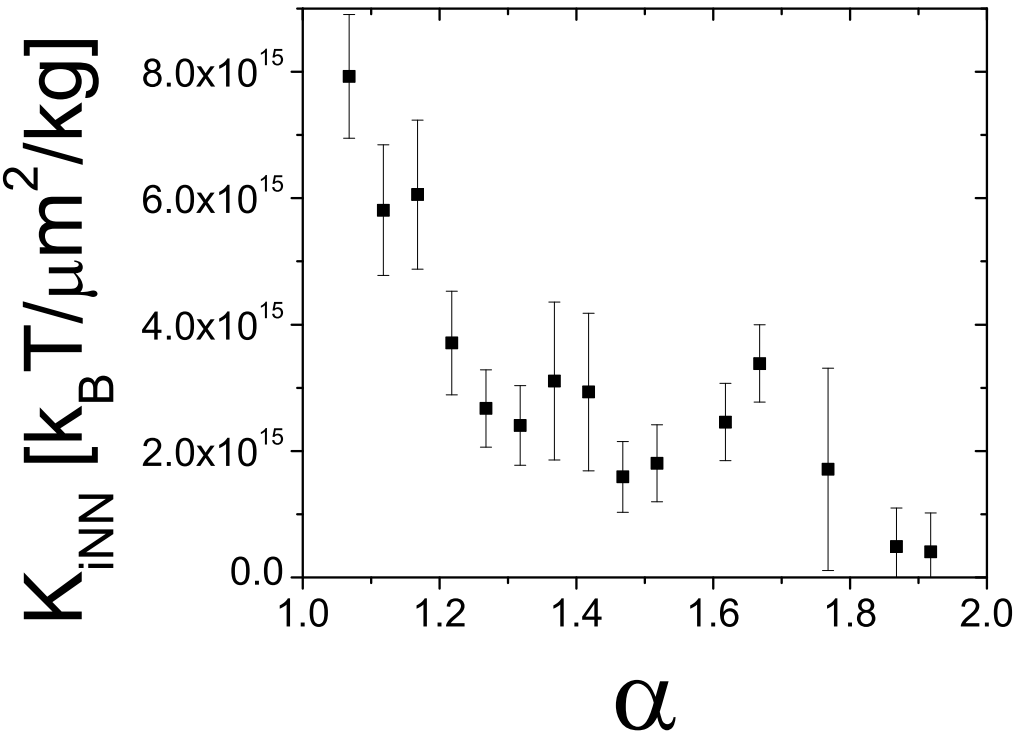

Figure 6.6: The average spring constant, K_{iNN}, connecting nearest neighbors as a function of aspect ratio, α, for samples with $\alpha_{Peak} = 1.1$. Error bars represent standard error.

6.4.1 Error and Uncertainty in Measurement of Phonon Modes

While K_{ij} is far above the noise only for adjacent particles, it is not 0 for non-neighboring particles. Uncertainty from particle tracking uncertainty leads to an uncertainty in ω of about 750 rad/s. Further, it is possible that small particle rearrangements could induce error in measured displacement covariance. While we verify that each particle has the same position at the beginning and end of the data collection period within our spatial resolution, rearrangements that occur just below our noise level could influence the measured fluctuations. Understanding the sources of noise in the displacement covariance method is an ongoing effort (e.g., [70]) that holds important consequences for colloidal experiments.

6.5 Phonon Modes for Glasses Composed of Anisotropic Particles

Representative modes are shown in Fig. 6.1 f-h and Fig. 6.5 f-h for samples with $\alpha_{Peak} = 1.1$ and 3.0, respectively. Modes from all samples can qualitatively be split into 3 regimes.

For $\alpha_{Peak} = 1.1$, 3 distinct regimes exhibiting different behavior are labelled in Fig. 6.1 b-e. Above $\omega \approx 54000$ rad/s, i.e., frequencies above the "dip" separating the two peaks in the density of states (Fig. 6.1 b), the modes in regime 3 are translational in character. The lowest frequency modes in regime 3 are spatially extended, while the highest frequency modes are spatially localized, similar to modes in glasses composed of spheres. Modes just above $\omega \approx 54000$ rad/s are enriched in longer ellipsoids and have a mixed translational/rotational character. Modes in regime 2, extending from $1300 \lesssim \omega \lesssim 54000$ rad/s, are strongly rotational in character and are concentrated on small aspect-ratio particles. In regime 1, below $\omega \approx 1300$ rad/s, modes again have a mixed rotational/translational character and are concentrated on longer

particles. Regime 1 was not observed in numerical simulations [189] of monodisperse ellipsoid packings at zero temperature. The likely origin of the new modes are the thermal fluctuations of particles with larger than average aspect ratios. Specifically, the mean value of elements of the stiffness matrix connecting particles to their neighbors decreases as aspect ratio increases; therefore longer ellipsoids are more weakly coupled to their neighbors and are more excited at low frequency.

Fig. 6.5 b-e show that for $\alpha_{Peak} = 3.0$, high frequency modes above $\omega \approx 3 \times 10^5$ rad/s in regime 3 are translational in character with a nearly average mode-averaged aspect ratio, resembling those of spheres. Thus, the modes are translational in character, crossing over from extended to localized at the upper end of the spectrum. Modes with $20000 \lesssim \omega \lesssim 3 \times 10^5$ rad/s in regime 2 are extended with a mixed rotational/translational character and are slightly concentrated on longer ellipsoids at higher frequencies and on shorter ellipsoids at somewhat lower frequencies. In regime 1, $\omega \lesssim 2 \times 10^4$ rad/s, modes are again slightly enriched in longer-aspect ratio particles and are quasilocalized with mixed character translational/rotational.

Note, the behavior of modes at high frequencies (regime 3) is qualitatively very similar in both systems. Additionally, the qualitative character of modes at the lowest frequencies (regime 2) is very similar in both systems. The largest qualitative differences between large and small aspect ratios systems occurs in regime 2, where modes have primarily rotational character for systems with $\alpha_{Peak} = 1.1$ and modes have mixed translational/rotational character for systems with $\alpha_{Peak} = 3.0$. In the rest of the paper, we present quantitative analysis supporting the qualitative characterization of modes in these systems given above.

To quantitatively decompose modes into their translational and rotational contributions, we

sum the participation fractions, P_F, of translational and rotational vibrations over all particles, for each mode. The eigenvectors of each mode are normalized such that $\sum_{m,n} e_\omega(m,n)^2 = 1$, where m runs over all particles and n runs over all coordinates. The participation *fraction* for particle m, component n, in mode with frequency ω is then $P_F(\omega) = e_\omega(m,n)^2$. Thus, the *translational* participation fraction in a mode with frequency ω is $P_{F,XY}(\omega) = \sum_{m=1..N,n=X,Y} e_\omega(m,n)^2$ and the *rotational* participation fraction is $P_{F,\theta}(\omega) = 1 - P_{F,XY}(\omega) = \sum_{m=1..N} e_\omega(m,\theta)^2$. Translational and rotational participation fractions are plotted in Fig. 6.1 c and Fig. 6.5 c.

To explore effects of polydispersity we measure the eigenvector-weighted ellipsoid aspect ratio as a function of mode frequency. Specifically, we compute $\bar{\alpha}_\omega = \sum_{m,n} \alpha_m e_\omega(m,n)^2$, where α_m is the measured aspect ratio of particle m. $\bar{\alpha}_\omega$ is thus a measure of the average particle aspect ratio for the particles participating in mode ω (Fig. 6.1 d and Fig. 6.5 d). For glasses composed of particles with $\alpha_{Peak} = 1.1$, the average over all modes of $\bar{\alpha}_\omega$ is $\bar{\alpha} = 1.17$ (the dotted horizontal line in Fig. 6.1 d). Fig. 6.1 d shows that the modes in regime 1 are concentrated on particles with higher aspect ratios. The rotational modes of regime 2 are dominated by particles with smaller aspect ratios, while the modes near the crossover between regimes 2 and 3 tend to be concentrated on particles with larger aspect ratios. It is not surprising that modes concentrated on long ellipsoids should have a mixed rotational/translational character since long ellipsoids tend to displace neighboring particles as they rotate. At high frequencies ($\omega \approx 180,000$ rad/s), $\bar{\alpha}_\omega$ approaches the global mean value of α.

For glasses composed of particles with $\alpha_{Peak} = 3.0$ (see Fig. 6.5 d), particles with smaller aspect ratios ($\sim$3.0) tend to participate in intermediate frequency modes while those with larger aspect ratios ($\sim$3.3) tend to participate in higher frequency modes. Additionally, modes with

particles with larger aspect ratios tend to participate in the lowest frequencies ($\omega < 12000$ rad/s), though the variance from mode-to-mode is large (see large error bars in Fig. 6.5 d).

Finally, we quantify the spatial extent of individual modes by computing the participation *ratio*, $P_R(\omega) = (\sum_{m,n} e_\omega(m,n)^2)^2/(N_{tot}\sum_{m,n} e_\omega(m,n)^4)$ (Fig. 6.1 e and Fig. 6.5 e). The participation ratio provides an indication of mode localization in space. If a mode is localized, a small number of terms will dominate, making $\sum_{m,n} e_\omega(m,n)^4$ and $(\sum_{m,n} e_\omega(m,n)^2)^2$ similar in size so $P_R(\omega) \approx 1/N$.

Low frequency modes for samples with $\alpha_{Peak} = 1.1$ have mixed rotational/translational character. These modes were not seen in zero-temperature simulations in which all particles have identical aspect ratios [113,189]. These 'mixed' modes typically involve larger aspect ratio particles. To understand why these modes appear at low frequencies, we calculated the average spring constant connecting a particle's rotation to its nearest neighbors $K_{iNN} =< K_{ij}/m_{ij} >_{NN}$, where $<>_{NN}$ indicates an average over nearest neighbors pairings, i runs over all theta components and j runs over all components. We then plotted K_{iNN} as a function of aspect ratio (Fig. 6.4). K_{iNN} decreases as α increases, indicating that the average spring constraining rotation decreases as α increases. Smaller spring constants K_{iNN} lead to vibrations at smaller frequencies. Thus, particles with longer aspect ratios tend to vibrate at lower frequencies.

6.6 Summary

To summarize, low frequency modes in glasses depend strongly on constituent particle aspect ratio. Rotational modes tend to occur at lower frequencies than translational vibrations, and, for glasses with aspect ratios $\sim$1.1, there is a frequency regime in which the spectrum is strongly

rotational in character. Additionally, even within each sample, particles with smaller aspect ratios tend to participate more in rotational modes while particles with larger aspect ratios tend to participate more in translational modes. The distribution of particle aspect ratio, N(α), is thus an important physical factor affecting phonon modes. Recent work suggests that low-participation-ratio, low-frequency modes appear to correlate with regions prone to rearrangement or plastic deformation [174]. Thus, the existence of additional low frequency modes concentrated around particles with short aspect ratios may have important consequences for the mechanical response of glasses.

Chapter 7

Phonon Spectra of Disordered Colloidal Clusters with Attractive Interactions

7.1 Introduction

The phase behavior and vibrational properties of ensembles of *repulsive* particles are determined largely by packing fraction [75, 136]. Samples of monodisperse spheres, for example, gain structural order and eventually crystallize with increasing packing fraction [75], giving rise to low frequency plane-wave-like phonon modes important for thermal and mechanical properties. In a related vein, ensembles of polydisperse spheres gain contacts with increased packing fraction, leading to vitrification [164] and "soft phonon modes" whose properties depend on average numbers of interparticle contacts [178]. By contrast to these "space-filling" systems, particles

with strong *attractive* interactions can form solid-like phases at low macroscopic packing fractions [188]. Dilute gels, for example, mechanically percolate across large distances [104], and disordered clusters containing relatively few particles often self-assemble into structures with large local packing fraction [107, 116]. In this paper we explore how cluster morphology and cluster size affect the vibrational properties of disordered materials held together by strong attractive interactions. New understanding thus gained holds potential to elucidate fundamental differences between glassy materials composed of particles with attractive versus repulsive interactions, to uncover connections between vibrational spectra, mechanical stability, and the jamming problem, and to discover those attributes of a disordered cluster that endow it with bulk-like properties of glasses.

To date, a diverse collection of disordered systems have been observed to display surprising commonality in their vibrational properties. Such systems include molecular [151], polymer [55], and colloidal glasses [23, 57, 90]. These disordered solids exhibit an excess of low frequency modes that are believed important for their mechanical and thermal properties [134]. The low frequency modes also appear connected to scaling and mechanical behaviors of repulsive spheres near the zero-temperature jamming transition. At the jamming point, such disordered packings are "isostatic", i.e., they have exactly the number of contacts per particle required for mechanical stability; if a single contact is removed, the packing is no longer stable. Interestingly, marginal stability permits particle displacements that maintain isostaticity without energy cost; these motions are manifest as low frequency "soft" phonon modes [81, 178]. When the sample packing fraction is increased above the jamming transition, the number of contacts per

particle increases, the system is stabilized [125], and the number of soft modes is found to decrease [178]. In fact, the minimum soft mode frequency has been predicted to increase linearly with number of contacts per particle above the isostatic requirement [178]. Recent experiments have found some of these trends in thermal packings of repulsive particles [23,57,90], but application of such concepts to systems of particles with attractive interactions has proven difficult. Packings of attractive particles can achieve isostaticity at arbitrary packing fraction, and even when they do not have enough contacts to be isostatic as a whole, the attractive systems can still have local mechanically stable regions [81]. Thus, the study of vibrational properties in clusters of attractive particles also provides useful clues about underlying mechanisms responsible for the mechanical properties of disordered solids.

In this contribution we experimentally investigate the influence of cluster morphology and size on the vibrational properties of disordered clusters of colloidal particles with attractive interactions. The disordered clusters with high local packing fractions are formed in water-lutidine (WL) suspensions wherein wetting effects induce fluid mediated attractions between micron-sized polystyrene particles. Each cluster is characterized by the number of particles it contains (N), the average number of nearest neighbors (NN), and the number of local isostatic configurations (N_{Iso}). Displacement correlation matrix techniques employed in recent papers [23, 57, 58, 90] are used to determine phonon spectra in each attractive glass cluster. Specifically, video microscopy is employed to derive the phonon density of states of corresponding "shadow" attractive glass clusters with the same geometric configuration and interactions as the "source" experimental colloidal system but absent damping [23]. Surprisingly, the spectra and character of vibrational modes depend strongly on the average number of nearest neighbors

(NN) but only weakly on the number of particles (N) in the glassy cluster. The median phonon frequency, ω_{Med}, which characterizes the distribution of low and high frequency modes, is observed to be essentially constant for NN < 2 and then grows linearly with NN for NN > 2. This behavior parallels concurrent observations about local isostatic structures, which are absent in clusters with NN < 2 and then grow linearly in number for NN> 2. Thus cluster vibrational properties appear to be strongly connected to cluster mechanical stability (i.e., fraction of locally isostatic regions), and the scaling of ω_{Med} with NN is reminiscent of the behavior of packings of spheres with repulsive interactions at the jamming transition. Simulations of random networks of springs corroborate observations and further suggest that connections between phonon spectra and nearest neighbor number are generic to disordered networks.

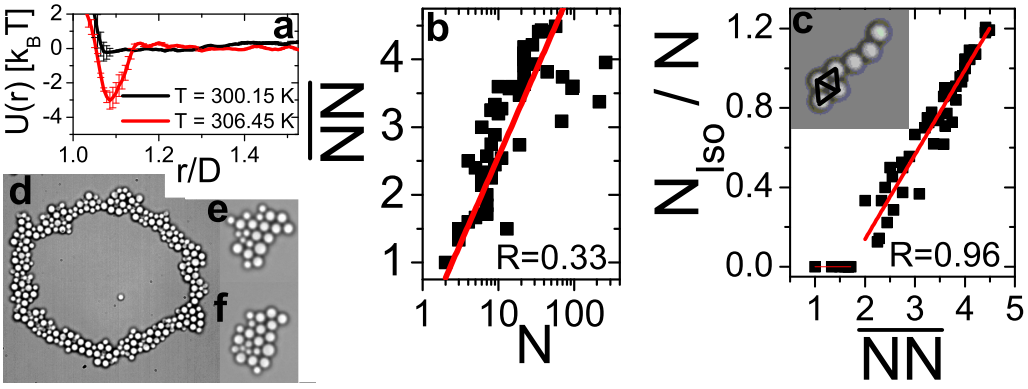

Figure 7.1: a. Plot summarizing the number of particles, N, and average number of nearest neighbors, NN, in every cluster. b. Cluster with N = 261 and NN = 3.95. c. Cluster with N = 22 and NN = 3.91. d. Cluster with N = 22 and NN = 4.09. e. Plot of the temperature-dependent interparticle potential, u(r), induced by near-critical water-lutidine mixtures, as a function of particle separation at two different temperatures, T = 300.15 K and 306.45 K. f. The number-fraction of locally isostatic configurations per particle, N_{Iso}/N is plotted versus NN. Solid lines are linear fits within two separate regimes.

7.2 Methods and Materials

The experiments employ bidisperse suspensions of micron-sized polystyrene particles (Invitrogen), with diameters $d_S = 1.5\mu$m and $d_L = 1.9\mu$m, and number ratio 1:2, respectively. Binary mixtures of particles were used to minimize crystallization effects. Particles were suspended in a mixture of water and 2, 6-lutidine (WL) near its critical composition, i.e., with lutidine mass fraction of 0.28. Colloidal particles suspended in this near-critical WL binary mixture experience temperature dependent repulsive or attractive interactions, whose origins can be fluid-mediated wetting, as in the current experiments, or critical Casimir forces [14, 71]. Interparticle potentials were determined from measurements of the particle pair correlation function with liquid structure theory and image artifact corrections [67] (Fig. 7.1 a). Many different disordered particle clusters are created by first suspending particles deep in the repulsive regime (300.15 K), and then increasing the sample temperature (to $306.5K$) *in situ*. Sample temperature control was accomplished using an objective heater (Bioptechs) connected to the microscope oil immersion objective [181, 182, 191]. Particles are confined between two glass coverslips (Fisher) with a spacing of $\sim(1.1 \pm 0.05)d_L$, making the sample system quasi-2D. The glass cell was treated with NaOH, so the particle-wall interaction potential is repulsive at relevant temperatures [154]. The global area fraction is ~ 0.2. Disordered clusters of various sizes and shapes self-assemble. Other clusters are assembled with aid of laser tweezers [61], either by grabbing particles and adding them to existing clusters, or by dragging an optical trap across a cluster and forcing rearrangements. Samples equilibrated for about six hours, and video data were collected at a rate of 10 frames per second.

7.3 Characterization of Structure

As noted above, the structure of particle clusters are characterized by several factors including average number of nearest neighbors per particle and the number of locally isostatic configurations. Neighbors are defined as particles located within a cutoff distance equal to the first minimum in the particle pair correlation function. Local isostatic regions consist of three particles (a, b, and c) that are mutually nearest neighbors (a and be are neighbors, a and c are neighbors, and b and c are neighbors). A plot summarizing N, NN, and N_{Iso} for each cluster studied is shown in Fig. 7.1, along with experimental snapshots of selected clusters. NN tends to increase non-monotonically with increasing N for our distribution of cluster sizes. The dependence of N_{Iso} on NN exhibits two regimes. Specifically, N_{Iso}/N is 0 for NN<2, becomes non-zero at NN$=/2$, and then grows linearly with NN for NN>2. Thus, we identify NN$=/2$ as the "local isostatic" point.

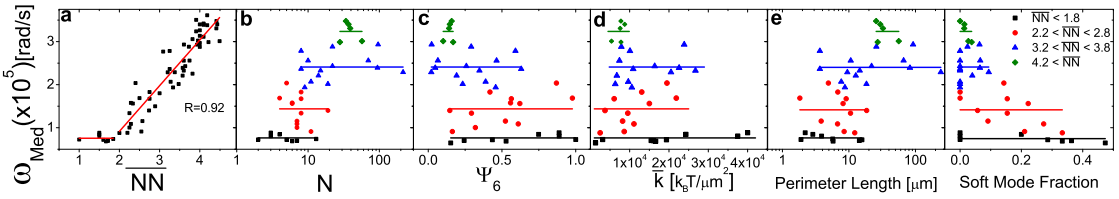

Figure 7.2: a. Median frequency, ω_{med}, versus average number of nearest neighbors, NN. Two regimes exist. For NN<2 ω_{Med} is constant (line is constant fit). For NN>2 ω_{Med} increases linearly with NN (line is a linear fit). b. ω_{med} versus number of particles, N. c. ω_{med} versus orientational order parameter, ψ_6. d. ω_{med} versus average total nearest neighbor spring constant, k.

7.4 Measurement and Characterization of Phonon Modes

7.4.1 Measurement of Phonon Modes

The vibrational properties of each cluster are extracted by measuring displacement correlations of the particles within each cluster. Specifically, we define $u(t)$ as the $2N$-component vector of the displacements of all particles from their average positions $(\bar{x}, \bar{y})$ and extract the time-averaged displacement correlation matrix (covariance matrix), $C_{ij} = \langle u_i u_j \rangle_t$ where $i, j = 1, ..., 2N_{tot}$ run over particles and positional coordinates, and the average runs over time. In the harmonic approximation, the correlation matrix is directly related to the stiffness matrix, defined as the matrix of second derivatives of the effective pair interaction potential with respect to particle position displacements. In particular, $(C^{-1})_{ij} k_B T = K_{ij}$ where K_{ij} is the stiffness matrix. Experiments that measure C therefore permit us to construct and derive properties of a "shadow" glass system that has the same static properties as our colloidal system (e.g., same correlation matrix, same stiffness matrix) [23]. Following [18], we expect undamped particles that repel at short-range to give rise to solid-like vibrational behavior on time scales long compared to particle collision times but short compared to the time between particle rearrangement events [57, 58]. The stiffness matrix is directly related to the dynamical matrix characterizing vibrations, $D_{ij} = \frac{K_{ij}}{m_{ij}}$, where $m_{ij} = \sqrt{m_i m_j}$ and m_i is the mass of particle i. The eigenvectors of the dynamical matrix correspond to amplitudes associated with the various phonon modes, and the eigenvalues correspond to the frequencies/energies of the corresponding modes. Data were collected over $10,000$ seconds so that the number of degrees of freedom, $8 \leq 2N \leq 500$, is small compared to the number of time frames ($> 10 \times 2N$) [23]. Additionally, we find K_{ij} is far above the noise only for adjacent particles, as expected.

7.4.2 Error and Uncertainty in Measurement of Phonon Modes

While K_{ij} is far above the noise only for adjacent particles, it is not 0 for non-neighboring particles. Uncertainty from particle tracking uncertainty leads to an uncertainty in ω of about 750 rad/s. Further, it is possible that small particle rearrangements could induce error in measured displacement covariance. While we verify that each particle has the same position at the beginning and end of the data collection period within our spatial resolution, rearrangements that occur just below our noise level could influence the measured fluctuations. Understanding the sources of noise in the displacement covariance method is an ongoing effort (e.g., [70]) that holds important consequences for colloidal experiments.

7.4.3 Characterization of Phonon Modes

Comparing the frequency spectra of clusters with small N can be challenging, because not enough modes are present to clearly identify a traditional "peak" frequency, and fluctuations can significantly shift the mean mode frequency. Instead, we characterize each cluster's density of states by its median frequency, ω_{med}, i.e. we choose the frequency, ω_{med}, such that half of the cluster mode frequencies are smaller than ω_{med} and half are larger. Plots of ω_{med} as a function of average number of nearest neighbors, NN, and as a function of total number of cluster particles, N (at fixed NN), are shown in Fig. 7.2. Surprisingly, ω_{med} has little correlation with N. However, ω_{med} depends strongly on the average number of nearest neighbors (NN). We observe two distinct regimes in this case. For NN$< /2$, ω_{Med} is constant. For NN> 2, ω_{Med} increases linearly with NN, exhibiting a linear correlation coefficient, R, of $R = 0.92$ ($R = 0.29$ for N and ω_{Med}). Interestingly, the dependence of ω_{Med} on NN is very similar to the dependence of

the number-fraction of locally isostatic configurations per particle, i.e., N_{Iso}/N, on NN. These observations suggest that the vibrational properties of disordered clusters is strongly dependent on the presence of locally rigid elements. Note, we also expect to observe a correlation between ω_{med} and N for our cluster distribution; this correlation arises because NN increases with N for typical cluster distributions. Thus the vibrational spectra of a disordered attractive cluster should become similar to that of a bulk glass as the total number of particles in the cluster increases; however, the underlying mechanism for this effect depends on the average number of nearest neighbors in the cluster, rather than total particle number.

The linear dependence of ω_{med} on NN (NN$<$ 2) is reminiscent of the behavior of hard-spheres in the vicinity of the zero-temperature jamming transition [178]. In this case, the characteristic frequency of excess quasi-localized or "soft" modes, ω^*, is predicted to increase linearly with NN when NN>NN_C, where NN_C is the number of contacts necessary for isostaticity. Similarly, in our experiments with attractive particles, ω_{Med} increases linearly with NN when NN$>$ $/2$ and locally rigid elements are present. Interestingly, in thermal experiments with *repulsive particles*, ω_{Med} shows a strong linear correlation with ω^* ($R = /0.96$), and ω_{Med} has a strong linear relationship with NN. These observations therefore suggest that similar physics may control properties of both highly packed glasses composed of particles with repulsive interactions and low (overall) packing fraction disordered clusters composed on particles with attractive interactions.

In order to further drive home the importance of number of nearest neighbors versus number of particles in a cluster, consider two clusters that look very different (Fig. 7.1 b and c) but have almost the same number of average nearest neighbors (NN). These clusters have similar

characteristic frequencies (i.e., ω_{Med}). On the other hand, two clusters that contain the exact same number of particles but have different NN (Fig. 7.1 c and d) possess a set of very different characteristic frequencies. More precisely, the clusters shown in Fig. 7.1 b-d contain $N = 261, 22, 22$ particles and have $NN = 3.95, 3.82, 4.18$, respectively. Despite the difference in N, ω_{med} is very similar for clusters shown in Fig. 7.1 b and c ($\omega_{med} = 3.0 \times 10^5$ and 3.1×10^5, respectively). Conversely, ω_{med} is quite different for clusters shown in Fig. 7.1 c and d ($\omega_{med} = 3.1 \times 10^5$ and 3.6×10^5, respectively).

As per other calculable cluster properties, ω_{med} does not appear to correlate strongly with many traditional structural quantities, including the bond orientational order parameter, ψ_6, the average stiffness between nearest neighbor pairs, $\bar{k} = 1/N \sum_{i=1..N} \sum_{j=1..NN_i} |K_{ij}|/NN_i$, and the cluster perimeter length, i.e., the contour length of cluster exterior. These parameters do not correlate strongly with ω_{med}, when $\overline{NN}$ is held approximately constant (Fig. 7.2 c-e). Thus, simple ideas for the effects based on surface area or perimeter length are not sufficient to explain experimental observations. Additionally, the fraction of soft modes does not correlate strongly with ω_{med}, when $\overline{NN}$ is held approximately constant (Fig. 7.2 f).

To identify the number of soft modes, we plotted a histogram of all frequencies from all clusters; the dip in this histogram at low frequencies identifies a cutoff frequency (Fig. 7.3). Modes below this frequency ($\sim 6 \times 10^5$ rad/s), which represent $\sim 10\%$ of the total modes, are identified as soft modes. The minimum number of soft modes can be calculated by summing the total number of degrees of freedom, i.e., twice the number of particles, and subtracting the number of constraints on the system, i.e., the number of nearest neighbor bonds. This procedure, known as Maxwell counting (e.g., [161]), also predicts that $\sim 10\%$ of the modes should be soft

modes.

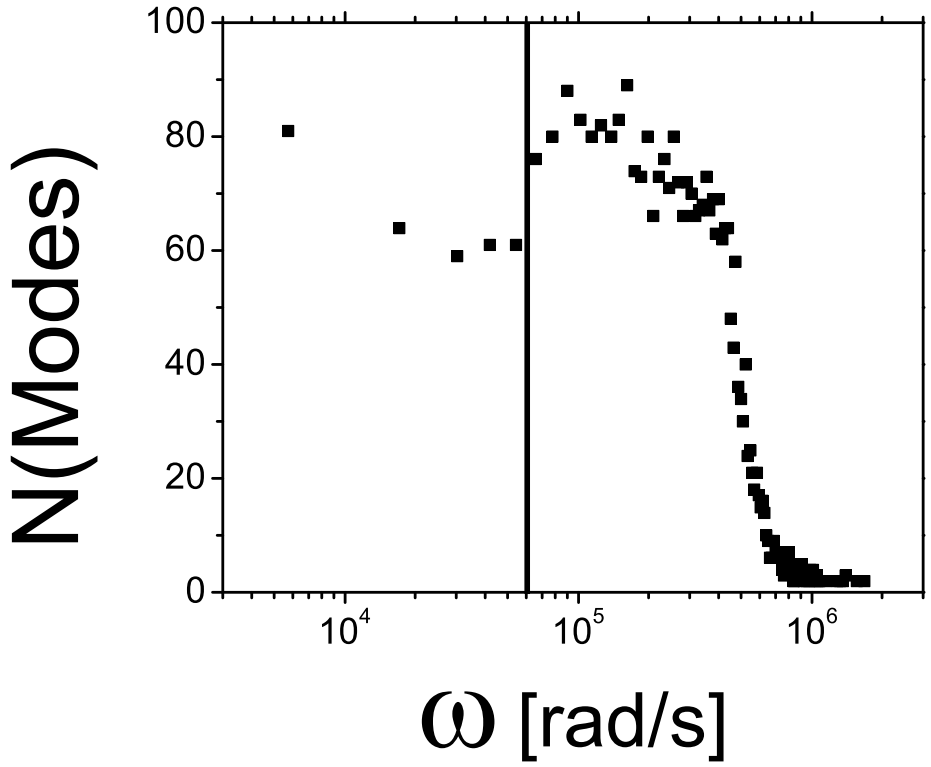

Figure 7.3: Histogram of frequencies from all clusters studied. The number of modes at a given frequency are plotted versus frequency. The vertical line marks the dip in the histogram; modes with frequencies below this cutoff are identified as soft modes.

The fraction of soft modes correlates with $\overline{NN}$ (Fig. 7.4) and the fraction of soft modes correlates with N_{ISO}/N (Fig. 7.5). However, these correlations are weaker than the correlation between $\overline{NN}$ and N_{ISO}/N (main text, Fig. 7.1 c). Additionally, the two separate regimes readily identifiable in plots of N_{ISO}/N versus $\overline{NN}$ and ω_{med} versus $\overline{NN}$, are not apparent in plots involving the fraction of soft modes.

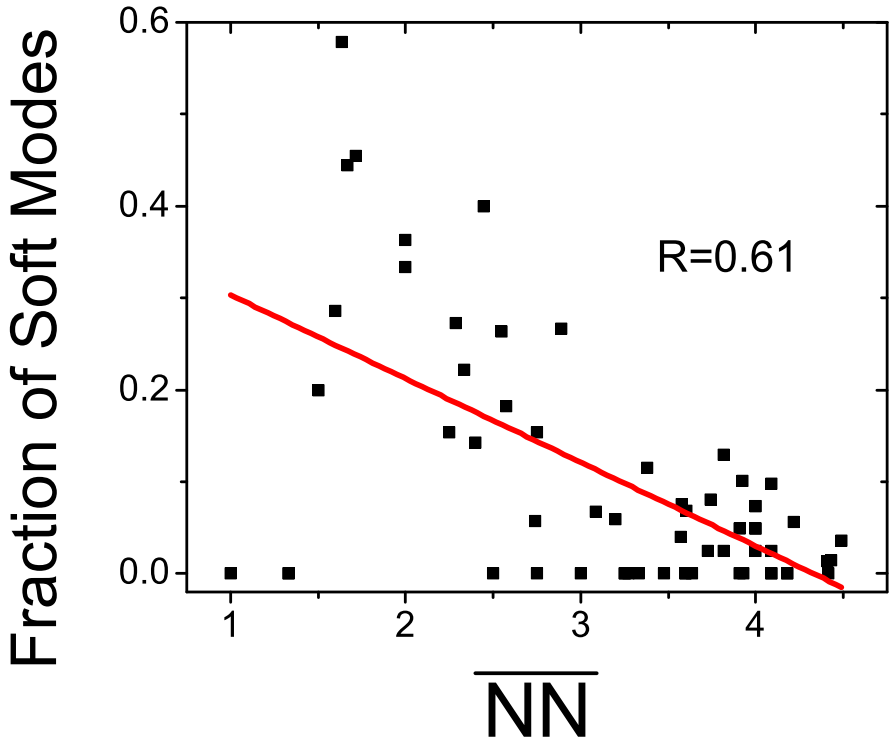

Figure 7.4: The fraction of soft modes is plotted versus the average number of nearest neighbors ($\overline{NN}$). The solid read line represents the best linear fit, and R represents the linear correlation coefficient.

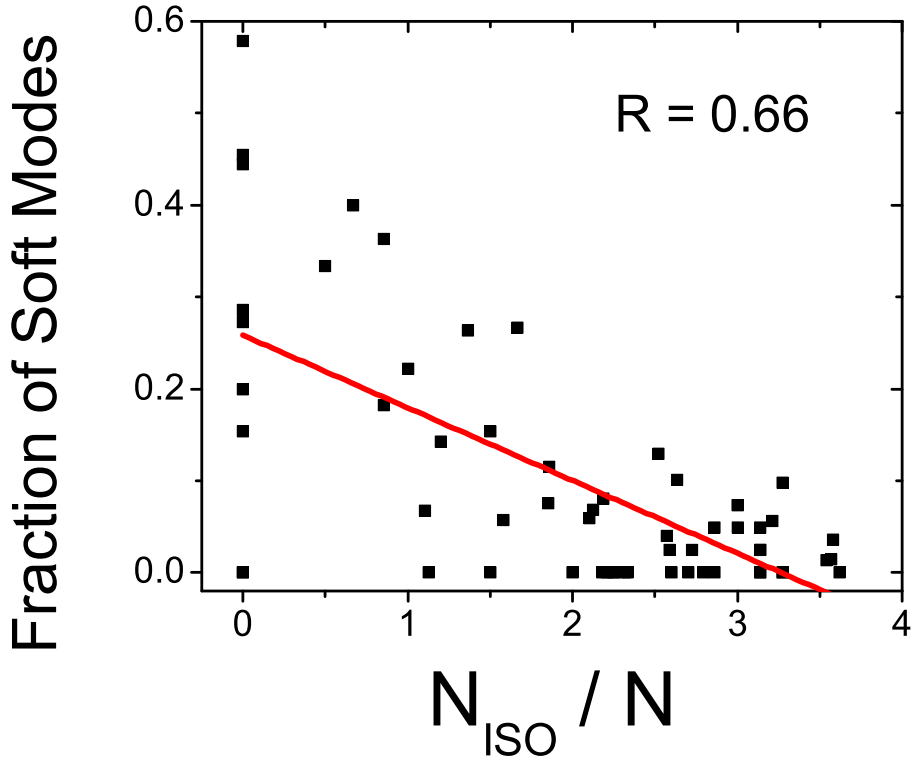

Figure 7.5: The fraction of soft modes is plotted versus the number of locally isostatic elements (N_{ISO}) normalized by the number of particles in the cluster (N). The solid read line represents the best linear fit, and R represents the linear correlation coefficient.

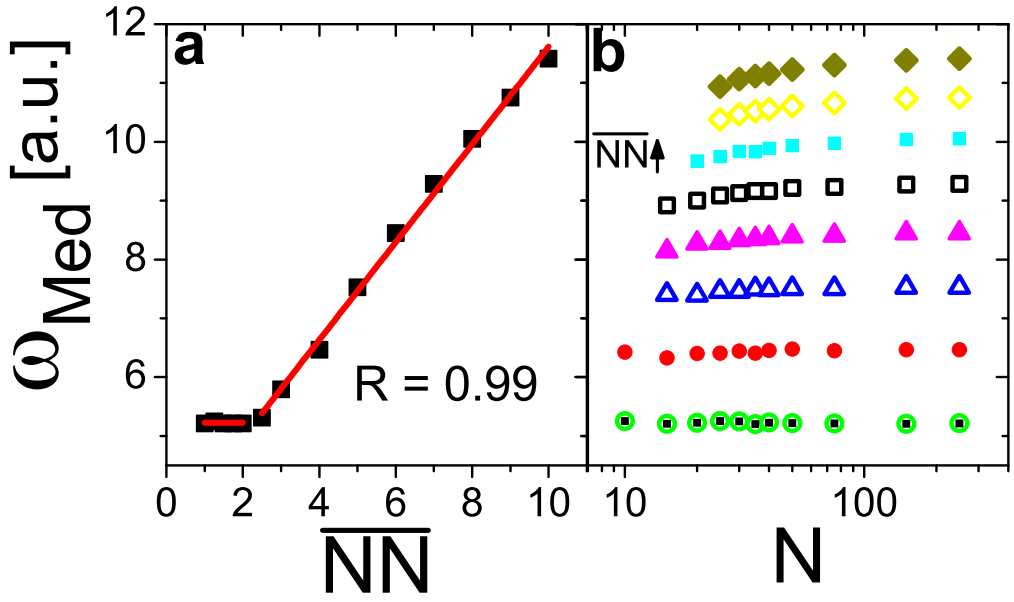

Figure 7.6: a. Median frequency, ω_{med}, plotted versus average number of nearest neighbors, NN, from simulations of random matrices. b. Median frequency, ω_{med}, plotted versus number of particles, N, from random matrices with NN$=$ 1 (closed squares), 2 (open circles), 3 (solid circles), 4 (open triangles), 5 (solid triangles), 6 (open squares), 7 (solid squares), 8 (open diamonds), and 9 (solid diamonds).

7.5 Computationally Generated Spring Networks

Unfortunately, in real experimental systems, structural parameters cannot be tuned completely independently. For example, clusters with large N and small NN are very difficult to create. As a final check on the importance of structural quantities of the attractive clusters other than NN, the spectra of randomly generated networks of springs were calculated. Random networks of springs, expressed as matrices, K_{ij}, were generated following a few simple rules that ensure the matrices only contain information about N and NN [10, 63, 177]. Each element, ij, in the matrix represents the spring constant between particle/coordinate i and particle/coordinate j. The number of rows/columns in these symmetric matrices is twice the number of particles, while the number of off diagonal elements greater than zero is equivalent to the number of nearest neighbors. Thus N and NN can be varied completely independently. Diagonal elements are set such that the sum of each row/column is zero, ensuring translational invariance. For every combination of N and NN, $10,000$ random matrices are generated. ω_{med} is calculated from the combination of all generated frequencies (Fig. 7.6). Many of these networks could not be duplicated in real systems, as nearest neighbor pairings are assigned at random and not based on proximity. However, ω_{med} follows the same trends in these simulations as observed in our experiments. Namely, ω_{med} has little or no correlation with N (i.e., with NN held constant, ω_{med} changes by less than 5%), but it exhibits a very strong correlation with NN (linear correlation coefficient > 0.99). Thus, ω_{med} appears to be the result of network connectivity, rather than a result of specific structure.

7.6 Summary

In conclusion, the spectra and character of vibrational modes in disordered "attractive" clusters do not depend strongly on the number of particles in the cluster, but do depend strongly on the average number of nearest neighbors and the number of locally isostatic configurations. Two regimes exist. When locally isostatic configurations are present (NN$>$ 2), then an increase in the number of nearest neighbors in the glass shifted the median frequency to higher frequencies, regardless of the total number of particles in the cluster. When locally isostatic regions are absent (NN$<$ 2), the median frequency is constant. The fact that ω_{med} depends on NN, but not on total number and packing fraction, suggests that these disordered clusters are a useful model system for network glasses (e.g. silica [56]). Network glasses are composed of particles (usually molecules) that have directional bond forming interactions which set NN [146], leading to the formation of solids at low packing fractions. In fact, the vibrational [84] and mechanical [190] properties of network glasses depend strongly on NN. Thus, disordered clusters composed of particles with attractive interactions could serve as a convenient model system for network glasses and their many applications (e.g. non-crystalline semiconductors [85]).

7.7 Future Directions

Recent experiments investigated three-dimensional clusters [116]. They utilized holographic microscopy, which enabled them to measure the x-, y-, and z-coordinates of each particle instantaneously. Thus, the vibrational properties of these clusters can measured using the same technique we used (extended to three translational degrees of freedom). This would allow us to

experimentally investigate the effects of dimensionality on the vibrational properties of disordered systems.

Chapter 8

Conclusion / Future Directions

8.1 Summary

Colloids are a versatile tool, capable of producing a wide swath of behaviors. In this dissertation we used colloids to study two broad problems: particle deposition and the glass transition. Colloids proved to be amenable to both topics. By modifying particle shape, sample geometry, and utilizing novel colloids and solvents, we were able to learn new details about complex nonequilibrium phenomenon.

The first group of experiments concerned the behavior of colloidal particles in evaporating drops, and the effects of particle shape. We started by evaporating drops of colloidal suspensions containing particles that range in shape from isotropic spheres to very anisotropic ellipsoids. Spheres are deposited in a heterogeneous ringlike fashion, also known as the coffee-ring effect. Conversely, ellipsoids are deposited uniformly. Due to their anisotropic shape, ellipsoids significantly deform the air-water interface, thus producing strong capillary-based interparticle attraction. After ellipsoids are carried to the air-water interface by the same outward flow that

drives the coffee ring effect for spheres, strong interparticle attraction leads to the formation of loosely-packed open networks of ellipsoids on the drop's surface. These quasi-static structures are capable of resisting shear, and thus lead to a more uniform deposition of ellipsoids.

Next, we confined drops of colloidal suspensions between glass plates, and allowed them to evaporate. After particles coated the air-water interface, it underwent buckling events similar to those seen in spherical elastic membranes. By analyzing the shape of these buckling events, we were able to measure elastic properties of these colloidal monolayer membranes (CMMs). The bending rigidity of CMMs is very dependent on particle shape; specifically, the bending rigidity increases by more than an order of magnitude as shape anisotropy is increased from isotropic spheres to anisotropic ellipsoids. This increase in bending rigidity leads to a dramatic difference in particle deposition. When colloids of any shape reach the drop's edge, they locally pin the contact line. For CMMs with low bending rigidity (e.g., spheres), the air-water interface bends around the local pinning point, leading to the formation of channels that are very dense with particles. Conversely, CMMs with large bending rigidity (e.g., ellipsoids) do not bend around local pinning sites; instead, ellipsoids adsorb on the air-water interface and are simply deposited as the meniscus recedes.

The next group of experiments concerns a different nonequilibriumn system, the glass transition. In the first experiment of this group, bidisperse colloidal suspensions of temperature-sensitive microgel spheres were quenched from liquid to glass states by a rapid temperature drop, achieved via optical heating. Once the particle returned to their original size, the glass was permitted to age. Irreversible rearrangements were measured. These events dramatically change a particle's local environment and appear closely related to dynamic heterogeneity. The rate of

these irreversible events decreased during aging and the the number of particles required to move as part of these irreversible rearrangements increased during aging. Thus, the slowing dynamics of aging were governed by a growing correlated domain of particles required to move for relaxation to occur. Additionally, short-range order and a length scale associated with orientational order both increased during aging.

The second glass transition experiment explored the role of frustration in the formation of glass by following the crystal-to-glass transition as a function of increasing frustration in quasi-two-dimensional binary colloidal suspensions. In these experiments, frustration is increased by adding a smaller species of particles to a crystal of large particles. The crystal-glass transition was found to be significantly different from the liquid-glass transition in structural and dynamic ways. In fact, the crystal-to-glass transition is structurally similar to the crystal-to-fluid transition. At the transition point, the orientational order spatial correlation function decreases sharply from quasi-long-range to short-range, and the orientational order susceptibility exhibits a maximum. However, the crystal-glass transition is also similar to the liquid-to-glass transition, as dynamic heterogeneity develops. Unlike the liquid-to-glass transition, the dynamic change associated with the crystal-to-glass transition is sharp: dynamic heterogeneity grows rapidly, and a dynamic correlation length-scale increases abruptly.

In the fifth overall set of experiments, we investigated the effect of particle shape on the phonon modes in colloidal glasses. We sythesized colloidal particles that are slightly anisotropic, and colloidal particles that are significantly anisotropic. By measuring displacement correlations between particles, we extract vibrational properties of the corresponding “shadow” ellipsoidal

glass with the same geometric configuration and interactions as the 'source' suspension but without damping. Low frequency modes were highly dependent on particle size. For suspensions of slightly anisotropic particles, low frequency modes were dominated by rotations. For suspensions of significantly anisotropic particles, low frequency modes mixed rotational and translational character. Due to particle aspect ratio polydispersity, we found that even within the same sample small-aspect-ratio particles tend to participate more in rotational modes, while large-aspect-ratio particles tend to participate more in translational modes.

In the final set of experiments, we sought to discover how big a disordered cluster has to be to behave like a bulk glass. To this end, we investigated the influence of morphology and size on the vibrational properties of disordered clusters of colloidal particles with attractive interactions. Spectral features of the vibrational modes are found to depend strongly on the average number of nearest neighbors, NN, but only weakly on the number of particles in each glassy cluster. Specifically, the median phonon frequency, ω_{Med}, is essentially constant for NN < 2 and then grows linearly with NN for NN > 2. This behavior parallels concurrent observations about local isostatic structures, which are absent in clusters with NN < 2 and then grow linearly in number for NN> 2. Thus cluster vibrational properties appear to be strongly connected to cluster mechanical stability (i.e., fraction of locally isostatic regions), and the scaling of ω_{Med} with NN is reminiscent of the behavior of packings of spheres with repulsive interactions at the jamming transition. Simulations of random networks of springs corroborate observations and further suggest that connections between phonon spectra and nearest neighbor number are generic to disordered networks. Thus, disordered clusters do not need a certain number of particles to behave like bulk glasses, but a certain number of neighbors.

8.2 Future Work

In this section, we describe ideas for future work with colloids exploring nonequilibrium phenomena.

8.2.1 Adsorption on the Air-Water Interface during Evaporation

When particles reach the edge of an evaporating drop, they adsorb on the air-water interface. The equilibrium position and contact angle of a particle on an interface is well described by the Laplace equation, which balances the various surface tensions. However, recent experiments utilizing high-resolution holographic microscopy found that spheres adsorbed on interfaces approach their equilibrium contact angles very slowly [91]. In fact, these spheres never reached their equilibrium contact angles within the experimental window, but approached them logarithmically over time. Returning to evaporating drops, do particles in evaporating drops reach their equilibrium contact angles? Holographic microscopy will not work in this system, as the air-water interface is not index matched. Understanding the behavior of spheres at the edge of drops will explain further details of coffee-ring effect, and likely suggest additional methods to alter or avoid the formation of a coffee-ring.

Instead, we can attempt to answer this question with more traditional experimental techniques. While a drop containing spheres evaporates, we can measure the distance between the spheres which have adsorbed nearest to the contact line and the contact line itself. This "front row" of spheres always sits on the glass substrate, which can be confirmed with confocal microscopy. By using large drops ($\geq 2\mu$l), the contact angle (measured in a separate set of experiments) will change very little during the first ~ 10 seconds of observation, thus keeping the

geometry of the problem constant. In this way, the contact angle between spheres at the edge of the drop and the air-water interface can be measured. This experiment can be repeated with different sizes of spheres to confirm the results. Further, spheres with rough surfaces or varying surface chemistry can be used to potentially slow the relaxation process.

An extension of this set of experiments could also help us interpret the behavior of colloidal particles on or near interfaces coated with surfactant. As noted in Chapter 2, adding surfactant to evaporating drops that contain ellipsoids restores the coffee-ring effect. However, the reason why ellipsoids are no longer deposited uniformly is unclear. It's possible that the ellipsoids adsorb on the interface, but deform it weakly as the surfactant decreases the surface tension. It's also possible that the ellipsoids never actually adsorb on the interface, which instead is densely coated with surfactant. To resolve this question, we could measure the position of spheres in evaporating drops containing surfactant.

8.2.2 Disordered Clusters as Model Glasses

The vibrational properties of small disordered clusters can be similar to the vibrational properties of macroscopic glasses (Chapter 7). This result suggests that the same underlying physics may be controlling vibrational properties in these superficially very different systems. Thus, it would be interesting to try to study other aspects of dense glasses in small clusters. A small cluster is less complex than a bulk glass, simply because it has fewer particles and thus fewer degrees of freedom.

Specifically, the dynamics of a cluster that contains ~ 100 particles can be observed and analyzed. If this cluster exhibits dynamic heterogeneity, then the source of these collective rearrangements may be easier to isolate than in a typical colloidal glass that has more than 2000

particles in the field of view alone. Further, by utilizing holographic optical tweezers [61], particles can be assembled into identical clusters many times, allowing us to collect meaningful statistics. The configuration of clusters could also be slightly modified with holographic optical tweezers from one iteration to the next, in an effort to isolate the source of collective rearrangements in glasses. For example, a region that is especially prone to rearrangements could be rearranged by hand in an effort to stabilize it.

In a different vein, recent experiments investigated three-dimensional clusters [116]. They utilized holographic microscopy, which enabled them to measure the x-, y-, and z-coordinates of each particle instantaneously. Thus, the vibrational properties of these clusters can measured using the same technique we used (extended to three translational degrees of freedom). This would allow us to experimentally investigate the effects of dimensionality on the vibrational properties of disordered systems.

8.2.3 Mixing Spheres and Ellipsoids in Colloidal Glasses

We demonstrated in Chapter 6 that particle shape anisotropy has a strong effect on the vibrational properties of glasses. Further, we showed that even within a sample, particles with slightly different degrees of anisotropy behave differently. Thus, it's natural to wonder what happens when spheres are mixed with ellipsoids of varying aspect ratios. To this end, dopant ellipsoids with various aspect ratios could be added to a glass composed of spherical particles, and the vibrational properties of the glass can be measured. Slightly anisotropic particles are an especially interesting case. Our previous experiments found that slightly anisotropic particles participate in low frequency modes with primarily rotational character. Adding a few particles that are slightly anisotropic to a glass composed of spheres would thus (possibly) create low frequency

modes that are localized around the anisotropic particles. Recently, it was demonstrated that low frequency modes in glasses composed of spheres are spatially correlated with regions prone to rearrangement [25]. Thus, adding slightly anisotropic particles to a glass composed of spherical particles may induce localized modes that are related to rearrangements. To figure this out, samples primarily containing spheres mixed with a small number of slightly anisotropic ellipsoids could be observed for long periods of time until rearrangements occur.

8.2.4 Aging to Completion

It would be interesting to compare rearrangement events during aging to rearrangements that contribute to the particle relaxation. This would allow us to determine if irreversible rearrangements move the system towards equilibrium, or if they are the events that comprise equilibrium particle relaxation. To facilitate such a comparison, we could quench to a lower packing fraction which will age to completion. Initially, the MSD will age like in the data presented in Chapter 4, but eventually the MSD will stop changing. If the particle relaxation time is within the experimental window (~ 100 seconds), we can directly compare the rearrangements that occur after aging to the rearrangements that occur during aging.

8.2.5 Evaporation of Drops Containing PNIPAM Particles

At first glance, it may appear that evaporating a drop containing PNIPAM particles will trivially produce the coffee-ring effect. However, recent experiments have shown that PNIPAM particles exhibit intriguing properties on interfaces (e.g., the air-water interface) [100, 120]. Specifically, PNIPAM particles were found to be especially good stabilizers for Pickering emulsions [100]. This is apparently due to the fact that PNIPAM particles flatten upon adsorption [100, 120].

Thus, the deformations of PNIPAM particles may make them especially susceptible to surface flows along the drop's air-water interface, which are typically directed radially inward. Thus, the coffee-ring effect may be avoided for PNIPAM particles due to *changing* shape.

Thus, PNIPAM particles might coat the surface of a drop during evaporation. If they do, monolayer membranes could be created by adding a small amount of cross-linker to a relatively dilute suspension. Specifically, PNIPAM will coat the air-water interface, forming a densely packed monolayer. Crosslinking molecules can then connect neighboring particles on the drop's surface. Since the PNIPAM particle packing fraction is low, particles are unlikely to be cross-linked in the bulk fluid.

Bibliography

[1] A. R. Abate and D. J. Durian. Topological persistence and dynamical heterogeneities near jamming. *Physical Review E* **76** (2007).

[2] A. R. Abate and D. J. Durian. Effective temperatures and activated dynamics for a two-dimensional air-driven granular system on two approaches to jamming. *Physical Review Letters* **101** (2008).

[3] G. Adam and J. H. Gibbs. On the temperature dependence of cooperative relaxation properties in glass-forming liquids. *The Journal of Chemical Physics* **43**, 139–146 (1965).

[4] A. M. Alsayed, M. F. Islam, J. Zhang, P. J. Collings, and A. G. Yodh. Premelting at defects within bulk colloidal crystals. *Science* **309**, 1207–1210 August (2005).

[5] C. A. Angell. Formation of glasses from liquids and biopolymers. *Science* **267**(5206), 1924–1935 (1995).

[6] L. Assoud, F. Ebert, P. Keim, R. Messina, G. Maret, and H. Löwen. Ultrafast quenching of binary colloidal suspensions in an external magnetic field. *Physical Review Letters* **102**(23), 238301 (2009).

[7] S. Auer and D. Frenkel. Prediction of absolute crystal-nucleation rate in hard-sphere colloids. *Nature* **409**, 1020–1023 (2001).

[8] P. Bartlett and P. B. Warren. Reentrant melting in polydispersed hard spheres. *Phys. Rev. Lett.* **82**, 1979–1982 (1999).

[9] M. G. Basavaraj, G. G. Fuller, J. Fransaer, and J. Vermant. Packing, Flipping, and Buckling Transitions in Compressed Monolayers of Ellipsoidal Latex Particles. *Langmuir* **22**(15), 6605–6612 July (2006).

[10] Y. M. Beltukov and D. A. Parshin. Density of states in random lattices with translational invariance. Nov (2010).

[11] E. Berthier, J. Warrick, H. Yu, and D. J. Beebe. Managing evaporation for more robust microscale assaysPart 1. Volume loss in high throughput assays. *Lab Chip* **8**(6), 852–859 (2008).

[12] L. Berthier, G. Biroli, J. P. Bouchaud, L. Cipelletti, E. D. Masri, D. L'Hote, F. Ladieu, and M. Pierno. Direct experimental evidence of a growing length scale accompanying the glass transition. *Science* **310**, 1797–1800 December (2005).

[13] L. Berthier, G. Biroli, J. P. Bouchaud, L. Cipelletti, E. D. Masri, D. L'Hote, F. Ladieu, and M. Pierno. Direct experimental evidence of a growing length scale accompanying the glass transition. *Science* **310**, 1797–1800 December (2005).

[14] D. Beysens and T. Narayanan. Wetting-Induced Aggregation of Colloids. *Journal of Statistical Physics* **95**(5), 997–1008 June (1999).

[15] T. P. Bigioni, X.-M. Lin, T. T. Nguyen, E. I. Corwin, T. A. Witten, and H. M. Jaeger. Kinetically driven self assembly of highly ordered nanoparticle monolayers. *Nature Materials* **5**(4), 265–270 March (2006).

[16] N. Bowden, F. Arias, T. Deng, and G. M. Whitesides. Self-Assembly of Microscale Objects at a Liquid/Liquid Interface through Lateral Capillary Forces. *Langmuir* **17**(5), 1757–1765 March (2001).

[17] G. Brambilla, D. E. Masri, M. Pierno, L. Berthier, L. Cipelletti, G. Petekidis, and A. B. Schofield. Probing the Equilibrium Dynamics of Colloidal Hard Spheres above the Mode-Coupling Glass Transition. *Physical Review Letters* **102**(8), 085703+ February (2009).

[18] C. Brito and M. Wyart. On the rigidity of a hard-sphere glass near random close packing. *EPL (Europhysics Letters)* **76**(1), 149–155 October (2006).

[19] A. B. D. Brown, C. G. Smith, and A. R. Rennie. Fabricating colloidal particles with photolithography and their interactions at an air-water interface. *Physical Review E* **62**(1), 951–960 Jul (2000).

[20] R. Candelier, O. Dauchot, and G. Biroli. Building blocks of dynamical heterogeneities in dense granular media. *Physical Review Letters* **102**(8) (2009).

[21] J. A. Champion, Y. K. Katare, and S. Mitragotri. Making polymeric micro- and nanoparticles of complex shapes. *Proceedings of the National Academy of Sciences* **104**(29), 11901–11904 July (2007).

[22] D. Chandler and J. D. Weeks. Equilibrium structure of simple liquids. *Physical Review Letters* **25**, 149+ July (1970).

[23] K. Chen. *Physical Review Letters* (2010).

[24] K. Chen, W. G. Ellenbroek, Z. Zhang, D. T. N. Chen, P. J. Yunker, S. Henkes, C. Brito, O. Dauchot, W. van Saarloos, A. J. Liu, and A. G. Yodh. Low-Frequency Vibrations of Soft Colloidal Glasses. *Physical Review Letters* **105**(2), 025501+ July (2010).

[25] K. Chen, M. L. Manning, P. J. Yunker, W. G. Ellenbroek, Z. Zhang, A. J. Liu, and A. G. Yodh. Measurement of Correlations between Low-Frequency Vibrational Modes and Particle Rearrangements in Quasi-Two-Dimensional Colloidal Glasses. *Physical Review Letters* **107**, 108301+ August (2011).

[26] T. Chou, K. Mallick, and R. K. P. Zia. Non-equilibrium statistical mechanics: from a paradigmatic model to biological transport. *Reports on Progress in Physics* **74**(11), 116601+ November (2011).

[27] G. C. Cianci, R. E. Courtland, and E. R. Weeks. Correlations of structure and dynamics in an aging colloidal glass. *Solid State Communications* **139**, 599–604 September (2006).

[28] G. C. Cianci and E. R. Weeks. Aging of tetrahedral structure in a Lennard-Jones glass. In *Reports of the Institute of Fluid Science* volume 19 pages 51–56. Tohoku University (2007).

[29] F. Clément and J. Leng. Evaporation of Liquids and Solutions in Confined Geometry. *Langmuir* **20**(16), 6538–6541 August (2004).

[30] C. Cottin, H. Bodiguel, and A. Colin. Influence of wetting conditions on drainage in porous media: A microfluidic study. *Physical Review E* **84**(2), 026311+ August (2011).

[31] R. E. Courtland and E. R. Weeks. Direct visualization of ageing in colloidal glasses. *Journal of Physics: Condensed Matter* **15**, S359–S365 (2003).

[32] K. D. Danov and P. A. Kralchevsky. Capillary forces between particles at a liquid interface: General theoretical approach and interactions between capillary multipoles. *Advances in Colloid and Interface Science* **154**(1-2), 91–103 February (2010).

[33] K. D. Danov, P. A. Kralchevsky, and S. D. Stoyanov. Elastic Langmuir Layers and Membranes Subjected to Unidirectional Compression: Wrinkling and Collapse. *Langmuir* **26**(1), 143–155 January (2010).

[34] L. Daubersies and J. B. Salmon. Evaporation of solutions and colloidal dispersions in confined droplets. *Physical Review E* **84**, 031406+ September (2011).

[35] O. Dauchot, G. Marty, and G. Biroli. Dynamical heterogeneity close to the jamming transition in a sheared granular material. *Physical Review Letters* **95**(26), 265701+ Dec (2005).

[36] R. D. Deegan. Pattern formation in drying drops. *Physical Review E* **61**(1), 475–485 Jan (2000).

[37] R. D. Deegan, O. Bakajin, T. F. Dupont, G. Huber, S. R. Nagel, and T. A. Witten. Capillary flow as the cause of ring stains from dried liquid drops. *Nature* **389**(6653), 827–829 October (1997).

[38] R. D. Deegan, O. Bakajin, T. F. Dupont, G. Huber, S. R. Nagel, and T. A. Witten. Contact line deposits in an evaporating drop. *Physical Review E* **62**(1), 756–765 Jul (2000).

[39] B. J. deGans, P. . C. Duineveld, and U. . S. Schubert. Inkjet Printing of Polymers: State of the Art and Future Developments. *Adv. Mater.* **16**(3), 203–213 (2004).

[40] N. D. Denkov, O. D. Velev, P. A. Kralchevsky, I. B. Ivanov, H. Yoshimura, and K. Nagayama. Two-dimensional crystallization. *Nature* **361**(6407), 26 January (1993).

[41] E. Dickinson. Food emulsions and foams: Stabilization by particles. *Current Opinion in Colloid & Interface Science* **15**(1-2), 40–49 April (2010).

[42] P. Dillmann, G. Maret, and P. Keim. Polycrystalline solidification in a quenched 2d colloidal system. *Journal of Physics: Condensed Matter* **20**, 404216+ (2008).

[43] C. Donati, S. C. Glotzer, P. H. Poole, W. Kob, and S. J. Plimpton. *Physical Review E* **60** (1999).

[44] A. Donev, I. Cisse, D. Sachs, E. A. Variano, F. H. Stillinger, R. Connelly, S. Torquato, and P. M. Chaikin. Improving the density of jammed disordered packings using ellipsoids. *Science* **303**(5660), 990–993 February (2004).

[45] A. Donev, R. Connelly, F. H. Stillinger, and S. Torquato. Underconstrained jammed packings of nonspherical hard particles: Ellipses and ellipsoids. *Physical Review E* **75**(5), 051304+ May (2007).

[46] V. Dugas. Immobilization of single-stranded DNA fragments to solid surfaces and their repeatable specific hybridization: covalent binding or adsorption? *Sensors and Actuators B: Chemical* **101**(1-2), 112–121 June (2004).

[47] V. Dugas, J. Broutin, and E. Souteyrand. Droplet Evaporation Study Applied to DNA Chip Manufacturing. *Langmuir* **21**(20), 9130–9136 September (2005).

[48] H. B. Eral, D. M. Augustine, M. H. G. Duits, and F. Mugele. Suppressing the coffee stain effect: how to control colloidal self-assembly in evaporating drops using electrowetting. *Soft Matter* **7**(10), 4954–4958 (2011).

[49] M. Fasolo and P. Sollich. Equilibrium phase behavior of polydisperse hard spheres. *Phys. Rev. Lett.* **91**, 068301 (2003).

[50] P. Faure and P. Coussot. Drying of a model soil. *Physical Review E* **82**(3), 036303+ September (2010).

[51] H. Fecht. Defect-induced melting and solid-state amorphization. *Nature* **356**(6365), 133–135 (1992).

[52] B. Felder. Uber die TeilchengrossenabhangigkeIt der Lichtabsorption in heterogenen Systemen. 11. Experimentelle Untersuchungen an Modell-Teilchen. *Helvetica Chimica Acta* **49**, 440 (1966).

[53] D. A. Fletcher and R. D. Mullins. Cell mechanics and the cytoskeleton. *Nature* **463**(7280), 485–492 January (2010).

[54] J. B. Fournier and P. Galatola. Anisotropic capillary interactions and jamming of colloidal particles trapped at a liquid-fluid interface. *Physical Review E* **65**(3), 031601 Feb (2002).

[55] B. Frick and D. Richter. The Microscopic Basis of the Glass Transition in Polymers from Neutron Scattering Studies. *Science* **267**(5206) (1995).

[56] P. H. Gaskell and D. J. Wallis. Medium-Range Order in Silica, the Canonical Network Glass. *Physical Review Letters* **76**(1), 66–69 Jan (1996).

[57] A. Ghosh, V. K. Chikkadi, P. Schall, J. Kurchan, and D. Bonn. Density of states of colloidal glasses. *Physical Review Letters* **104**(24), 248305+ Jun (2010).

[58] A. Ghosh, R. Mari, V. Chikkadi, P. Schall, J. Kurchan, and D. Bonn. Density of states of colloidal glasses and supercooled liquids. *Soft Matter* (2010).

[59] S. Glotzer. Spatially heterogeneous dynamics in liquids: insights from simulation. *Journal of Non-Crystalline Solids* **274**, 342–355 (2000).

[60] S. C. Glotzer and M. J. Solomon. Anisotropy of building blocks and their assembly into complex structures. *Nature Materials* **6**(7), 557–562 August (2007).

[61] D. G. Grier. A revolution in optical manipulation. *Nature* **424**(6950), 810–816 August (2003).

[62] M. Guerdane and H. Teichler. Short-range-order lifetime and the "boson peak" in a metallic glass model. *Physical Review Letters* **101** (2008).

[63] V. Gurarie and J. T. Chalker. Some Generic Aspects of Bosonic Excitations in Disordered Systems. *Physical Review Letters* **89**(13), 136801+ Sep (2002).

[64] B. I. Halperin and D. R. Nelson. *Physical Review Letters* **41**, 519 (1978).

[65] T. Hamanaka and A. Onuki. Heterogeneous dynamics in polycrystal and glass in a binary mixture with changing size dispersity and composition. *Physical Review E* **75** (2007).

[66] Y. Han, N. Y. Ha, A. M. Alsayed, and A. G. Yodh. Melting of two-dimensional tunable-diameter colloidal crystals. *Physical Review E* **77** (2008).

[67] Y. L. Han and D. G. Grier. *Physical Review Letters* **91** (2003).

[68] Y. Han, Y. Shokef, A. M. Alsayed, P. Yunker, T. C. Lubensky, and A. G. Yodh. Geometric frustration in buckled colloidal monolayers. *Nature* **456**, 898–903 December (2008).

[69] S. I. Henderson, T. C. Mortensen, S. M. Underwood, and W. van Megen. Effect of particle size distribution on crystallisation and the glass transition of hard sphere colloids. *Physica A: Statistical and Theoretical Physics* **233**, 102 – 116 (1996).

[70] S. Henkes, C. Brito, and O. Dauchot. Dynamical fluctuations close to Jamming versus Vibrational Modes : a pedagogical discussion illustrated on hard spheres simulations, colloidal and granular experiments. December (2011).

[71] C. Hertlein, L. Helden, A. Gambassi, S. Dietrich, and C. Bechinger. Direct measurement of critical Casimir forces. *Nature* **451**(7175), 172–175 January (2008).

[72] C. C. Ho, A. Keller, J. A. Odell, and R. H. Ottewill. Preparation of monodisperse ellipsoidal polystyrene particles. *Colloid and Polymer Science* **271**, 469–479 (1993).

[73] I. M. Hodge. Effects of annealing and prior history on enthalpy relaxation in glassy polymers. 6. adam-gibbs formulation of nonlinearity. *Macromolecules* **20**, 2897–2908 November (1987).

[74] I. M. Hodge. Physical aging in polymer glasses. *Science* **267**, 1945–1947 (1995).

[75] W. G. Hoover and F. H. Ree. Melting Transition and Communal Entropy for Hard Spheres. *The Journal of Chemical Physics* **49**(8), 3609–3617 (1968).

[76] H. Hu and R. G. Larson. Evaporation of a Sessile Droplet on a Substrate. *The Journal of Physical Chemistry B* **106**(6), 1334–1344 February (2002).

[77] H. Hu and R. G. Larson. Marangoni Effect Reverses Coffee-Ring Depositions. *The Journal of Physical Chemistry B* **110**(14), 7090–7094 April (2006).

[78] J. Hutchinson. Physical aging of polymers. *Progress in Polymer Science* **20**, 703–760 (1995).

[79] V. Ilyin, I. Procaccia, I. Regev, and N. Schupper. Aging and relaxation in glass-forming systems. *Physical Review E* **77** (2008).

[80] S. D. J. Guzowski, M. Tasinkevych. Capillary interactions in Pickering emulsions. *arXiv:1103.5314* (2011).

[81] D. J. Jacobs and M. F. Thorpe. Generic Rigidity Percolation: The Pebble Game. *Physical Review Letters* **75**(22), 4051–4054 Nov (1995).

[82] A. Jaoshvili, A. Esakia, M. Porrati, and P. M. Chaikin. Experiments on the random packing of tetrahedral dice. *Physical Review Letters* **104**(18), 185501+ May (2010).

[83] T. Kajiya, W. Kobayashi, T. Okuzono, and M. Doi. Controlling the Drying and Film Formation Processes of Polymer Solution Droplets with Addition of Small Amount of Surfactants. *The Journal of Physical Chemistry B* **113**(47), 15460–15466 November (2009).

[84] W. A. Kamitakahara, R. L. Cappelletti, P. Boolchand, B. Halfpap, F. Gompf, D. A. Neumann, and H. Mutka. Vibrational densities of states and network rigidity in chalcogenide glasses. *Physical Review B* **44**(1), 94+ Jul (1991).

[85] T. Kamiya, K. Nomura, and H. Hosono. Present status of amorphous In"Ga"Zn"O thin-film transistors. *Science and Technology of Advanced Materials* **11**(4), 044305+ August (2010).

[86] S. H. Kang, N. Wu, A. Grinthal, and J. Aizenberg. Meniscus Lithography: Evaporation-Induced Self-Organization of Pillar Arrays into Moiré Patterns. *Physical Review Letters* **107**, 177802+ October (2011).

[87] T. Kawasaki, T. Araki, and H. Tanaka. *Physical Review Letters* **100**, 099602 (2008).

[88] T. Kawasaki, T. Araki, and H. Tanaka. Correlation between dynamic heterogeneity and medium-range order in two-dimensional glass-forming liquids. *Physical Review Letters* **99** (2007).

[89] D. Kaya, V. A. Belyi, and M. Muthukumar. Pattern formation in drying droplets of polyelectrolyte and salt. *The Journal of Chemical Physics* **133**(11), 114905 (2010).

[90] D. Kaya, N. L. Green, C. E. Maloney, and M. F. Islam. Normal modes and density of states of disordered colloidal solids. *Science* **329**(5992), 656–658 August (2010).

[91] D. M. Kaz, R. McGorty, M. Mani, M. P. Brenner, and V. N. Manoharan. Physical ageing of the contact line on colloidal particles at liquid interfaces. *Nat Mater* **advance online publication**(2), 138–142 December (2011).

[92] A. S. Keys, A. R. Abate, S. C. Glotzer, and D. J. Durian. Measurement of growing dynamical length scales and prediction of the jamming transition in a granular material. *Nature Physics* **3**, 260–264 (2007).

[93] W. Kob and J.-L. Barrat. Aging effects in a lennard-jones glass. *Physical Review Letters* **78**, 4581+ June (1997).

[94] W. Kob, J.-L. Barrat, F. Sciortino, and P. Tartaglia. Aging in a simple glass former. *Journal of Physics: Condensed Matter* **12**, 6385–6394 (2000).

[95] W. Kob, C. Donati, S. J. Plimpton, P. H. Poole, and S. C. Glotzer. Dynamical heterogeneities in a supercooled lennard-jones liquid. *Physical Review Letters* **79**, 2827–2830 Oct (1997).

[96] D. A. Kofke and P. G. Bolhuis. Freezing of polydisperse hard spheres. *Phys. Rev. E* **59**, 618–622 (1999).

[97] R. C. Kramb, R. Zhang, K. S. Schweizer, and C. F. Zukoski. Glass formation and shear elasticity in dense suspensions of repulsive anisotropic particles. *Physical Review Letters* **105**(5), 055702+ Jul (2010).

[98] P. Kumnorkaew, Y.-K. Ee, N. Tansu, and J. F. Gilchrist. Investigation of the Deposition of Microsphere Monolayers for Fabrication of Microlens Arrays. *Langmuir* **24**(21), 12150–12157 November (2008).

[99] L. D. Landau, L. P. Pitaevskii, E. M. Lifshitz, and A. M. Kosevich. *Theory of Elasticity, Third Edition: Volume 7 (Theoretical Physics)*. Butterworth-Heinemann 3 edition January (1986).

[100] V. Lapeyre, M. Wolfs, E. Sellier, F. Leal-Calderon, V. Ravaine, and V. Schmitt. Soft microgels as Pickering emulsion stabilisers: role of particle deformability. *Soft Matter* **7**(17), 7689–7698 (2011).

[101] H. Lehle, E. Noruzifar, and M. Oettel. Ellipsoidal particles at fluid interfaces. *The European Physical Journal E: Soft Matter and Biological Physics* **26**(1), 151–160 May (2008).

[102] J. Leng. Drying of a colloidal suspension in confined geometry. *Physical Review E* **82**(2), 021405+ August (2010).

[103] E. P. Lewandowski, J. A. Bernate, A. Tseng, P. C. Searson, and K. J. Stebe. Oriented assembly of anisotropic particles by capillary interactions. *Soft Matter* **5**(4), 886–890 (2009).

[104] M. Y. Lin, H. M. Lindsay, D. A. Weitz, R. C. Ball, R. Klein, and P. Meakin. Universality in colloid aggregation. *Nature* **339**(6223), 360–362 June (1989).

[105] J. C. Loudet, A. M. Alsayed, J. Zhang, and A. G. Yodh. Capillary Interactions Between Anisotropic Colloidal Particles. *Physical Review Letters* **94**(1), 018301 Jan (2005).

[106] J. C. Loudet, A. G. Yodh, and B. Pouligny. Wetting and Contact Lines of Micrometer-Sized Ellipsoids. *Physical Review Letters* **97**(1), 018304 Jul (2006).

[107] P. J. Lu, J. C. Conrad, H. M. Wyss, A. B. Schofield, and D. A. Weitz. Fluids of Clusters in Attractive Colloids. *Physical Review Letters* **96**(2), 028306+ Jan (2006).

[108] V. Lubchenko and P. G. Wolynes. Theory of aging in structural glasses. *The Journal of Chemical Physics* **121**, 2852–2865 (2004).

[109] J. M. Lynch, G. C. Cianci, and E. R. Weeks. *Physical Review E* (2008).

[110] J. M. Lynch, G. C. Cianci, and E. R. Weeks. Dynamics and structure of an aging binary colloidal glass. *Physical Review E* **78** (2008).

[111] B. Madivala, J. Fransaer, and J. Vermant. Self-Assembly and Rheology of Ellipsoidal Particles at Interfaces. *Langmuir* **25**(5), 2718–2728 March (2009).

[112] B. Madivala, S. Vandebril, J. Fransaer, and J. Vermant. Exploiting particle shape in solid stabilized emulsions. *Soft Matter* **5**(8), 1717–1727 (2009).

[113] M. Mailman, C. F. Schreck, C. S. O'Hern, and B. Chakraborty. Jamming in systems composed of frictionless ellipse-shaped particles. *Physical Review Letters* **102**(25), 255501+ Jun (2009).

[114] W. Man, A. Donev, F. H. Stillinger, M. T. Sullivan, W. B. Russel, D. Heeger, S. Inati, S. Torquato, and P. M. Chaikin. Experiments on random packings of ellipsoids. *Physical Review Letters* **94**(19), 198001+ May (2005).

[115] S. Martin, G. Bryant, and W. van Megen. Crystallization kinetics of polydisperse colloidal hard spheres: Experimental evidence for local fractionation. *Physical Review E* **67** (2003).

[116] G. Meng, N. Arkus, M. P. Brenner, and V. N. Manoharan. The Free-Energy Landscape of Clusters of Attractive Hard Spheres. *Science* **327**(5965), 560–563 January (2010).

[117] D. B. Miracle. A structural model for metallic glasses. *Nat Mater* **3**, 697–702 October (2004).

[118] M. Mittal and E. M. Furst. Electric Field-Directed Convective Assembly of Ellipsoidal Colloidal Particles to Create Optically and Mechanically Anisotropic Thin Films. *Adv. Funct. Mater.* **19**(20), 3271–3278 (2009).

[119] P. Moldenaers and J. Vermant. Interfacial rheology of stable and weakly aggregated two-dimensional suspensions. *Phys. Chem. Chem. Phys.* **9**(48), 6463–6475 (2007).

[120] C. Monteux, C. Marliere, P. Paris, N. Pantoustier, N. Sanson, and P. Perrin. Poly(N-isopropylacrylamide) Microgels at the OilWater Interface: Interfacial Properties as a Function of Temperature. *Langmuir* **26**(17), 13839–13846 August (2010).

[121] K. E. Mueggenburg, X.-M. Lin, R. H. Goldsmith, and H. M. Jaeger. Elastic membranes of close-packed nanoparticle arrays. *Nature Materials* **6**(9), 656–660.

[122] D. Nelson. Reentrant melting in solid films with quenched random impurities. *Physical Review B* **27** (1983).

[123] D. Nelson and B. Halperin. Dislocation-mediated melting in 2 dimensions. *Physical Review B* **19**(5), 2457–2484 (1979).

[124] V. X. Nguyen and K. J. Stebe. Patterning of Small Particles by a Surfactant-Enhanced Marangoni-Bénard Instability. *Physical Review Letters* **88**(16), 164501 April (2002).

[125] C. S. O'Hern, S. A. Langer, A. J. Liu, and S. R. Nagel. Random Packings of Frictionless Particles. *Physical Review Letters* **88**(7), 075507+ Jan (2002).

[126] B. J. Park and E. M. Furst. Fluid-interface templating of two-dimensional colloidal crystals. *Soft Matter* **6**(3), 485–488 (2010).

[127] B. J. Park and E. M. Furst. Attractive interactions between colloids at the oil-water interface. *Soft Matter* , – (2011).

[128] J. Park and J. Moon. Control of Colloidal Particle Deposit Patterns within Picoliter Droplets Ejected by Ink-Jet Printing. *Langmuir* **22**(8), 3506–3513 April (2006).

[129] A. Parsaeian and H. E. Castillo. Growth of spatial correlations in the aging of a simple structural glass. *Physical Review E* **78** (2008).

[130] L. Pauchard and Y. Couder. Invagination during the collapse of an inhomogeneous spheroidal shell. *EPL (Europhysics Letters)* , 667+ June (2004).

[131] L. Pauchard, M. Mermet-Guyennet, and F. Giorgiutti-Dauphiné. Invagination process induced by 2D desiccation of colloidal solutions. *Chemical Engineering and Processing: Process Intensification* **50**(5-6), 483–485 May (2011).

[132] R. Pelton. Temperature-sensitive aqueous microgels. *Advances in Colloid and Interface Science* **85**, 1–33 February (2000).

[133] D. N. Perera and P. Harrowell. Relaxation dynamics and their spatial distribution in a two-dimensional glass-forming mixture. *The Journal of Chemical Physics* **111**, 5441–5454 (1999).

[134] R. O. Pohl, X. Liu, and E. Thompson. Low-temperature thermal conductivity and acoustic attenuation in amorphous solids. *Reviews of Modern Physics* **74**(4), 991+ Oct (2002).

[135] S. Pronk and D. Frenkel. *Physical Review E* **69**, 066123 (2004).

[136] P. N. Pusey and W. van Megen. Phase behaviour of concentrated suspensions of nearly hard colloidal spheres. *Nature* **320**(6060), 340–342 March (1986).

[137] C. Roland, S. Hensel-Bielowka, M. Paluch, and R. Casalini. Supercooled dynamics of glass-forming liquids and polymers under hydrostatic pressure. *Reports on Progress in Physics* **68**, 1405–1478 June (2005).

[138] C. P. Royall, S. R. Williams, T. Ohtsuka, and H. Tanaka. Direct observation of a local structural mechanism for dynamic arrest. *Nature Materials* **7**, 556–561 July (2008).

[139] P. C. Royall, E. C. Vermolen, A. Blaaderen, and H. Tanaka. Controlling competition between crystallization and glass formation in binary colloids with an external field. *Journal of Physics: Condensed Matter* **20**, 404225 (2008).

[140] M. R. Sadr-Lahijany, P. Ray, and H. E. Stanley. *Physical Review Letters* **79**, 3206 (1997).

[141] L. M. C. Sagis. Rheology of interfaces stabilized by a 2D suspension of anisotropic particles: a classical irreversible thermodynamics theory. *Soft Matter* **7**(17), 7727–7736 (2011).

[142] B. R. Saunders and B. Vincent. Microgel particles as model colloids: theory, properties and applications. *Advances in Colloid and Interface Science* **80**, 1–25 February (1999).

[143] M. Scheel, R. Seemann, M. Brinkmann, M. Di Michiel, A. Sheppard, B. Breidenbach, and S. Herminghaus. Morphological clues to wet granular pilestability. *Nature Materials* **7**(3), 189–193 February (2008).

[144] H. J. Schöpe, G. Bryant, and W. van Megen. Effect of polydispersity on the crystallization kinetics of suspensions of colloidal hard spheres when approaching the glass transition. *The Journal of Chemical Physics* **127**, 084505 (2007).

[145] C. F. Schreck, N. Xu, and C. S. O'Hern. A comparison of jamming behavior in systems composed of dimer- and ellipse-shaped particles. *Soft Matter* **6**(13), 2960–2969 (2010).

[146] F. Sciortino. Gel-forming patchy colloids and network glass formers: thermodynamic and dynamic analogies. *The European Physical Journal B - Condensed Matter and Complex Systems* **64**(3), 505–509 August (2008).

[147] H. Senff and W. Richtering. Temperature sensitive microgel suspensions: Colloidal phase behavior and rheology of soft spheres. *The Journal of Chemical Physics* **111**, 1705–1711 (1999).

[148] Y. T. Shen, T. H. Kim, A. K. Gangopadhyay, and K. F. Kelton. Icosahedral order, frustration, and the glass transition: Evidence from time-dependent nucleation and supercooled liquid structure studies. *Physical Review Letters* **102** (2009).

[149] H. W. Sheng, W. K. Luo, F. M. Alamgir, J. M. Bai, and E. Ma. Atomic packing and short-to-medium-range order in metallic glasses. *Nature* **439**, 419–425 (2007).

[150] D. A. Sivak and G. E. Crooks. Near-Equilibrium Measurements of Nonequilibrium Free Energy. *Physical Review Letters* **108**, 150601+ April (2012).

[151] A. P. Sokolov, A. Kisliuk, M. Soltwisch, and D. Quitmann. Medium-range order in glasses: Comparison of Raman and diffraction measurements. *Physical Review Letters* **69**(10), 1540–1543 Sep (1992).

[152] M. J. Solomon and P. T. Spicer. Microstructural regimes of colloidal rod suspensions, gels, and glasses. *Soft Matter* **6**(7), 1391–1400 (2010).

[153] A. P. Sommer and N. Rozlosnik. Formation of Crystalline Ring Patterns on Extremely Hydrophobic Supersmooth Substrates: Extension of Ring Formation Paradigms. *Crystal Growth & Design* **5**(2), 551–557 March (2005).

[154] F. Soyka, O. Zvyagolskaya, C. Hertlein, L. Helden, and C. Bechinger. Critical Casimir Forces in Colloidal Suspensions on Chemically Patterned Surfaces. *Physical Review Letters* **101**(20), 208301+ Nov (2008).

[155] D. Stamou, C. Duschl, and D. Johannsmann. Long-range attraction between colloidal spheres at the air-water interface: The consequence of an irregular meniscus. *Physical Review E* **62**(4), 5263–5272 October (2000).

[156] T. Still, P. J. Yunker, and A. G. Yodh. Surfactant-Induced Marangoni Eddies Alter the Coffee-Rings of Evaporating Colloidal Drops. *Langmuir* **28**(11), 4984–4988 February (2012).

[157] H. A. Stone. Fluid motion of monomolecular films in a channel flow geometry. *Physics of Fluids* **7**(12), 2931–2937 (1995).

[158] H. Tanaka. Two-order-parameter model of the liquid-glass transition. i. relation between glass transition and crystallization. *Journal of Non-Crystalline Solids* **351**, 3371–3384 November (2005).

[159] H. Tanaka, T. Kawasaki, H. Shintani, and K. Watanabe. Critical-like behaviour of glass-forming liquids. *Nature Materials* **9**(4), 324–331 February (2010).

[160] G. Tarjus, S. A. Kivelson, Z. Nussinov, and P. Viot. The frustration-based approach of supercooled liquids and the glass transition: a review and critical assessment. *Journal of Physics: Condensed Matter* **17**, R1143–R1182 (2005).

[161] M. F. Thorpe. *J. Non-Cryst. Solids* **57**, 355 (1983).

[162] N. Tsapis, E. R. Dufresne, S. S. Sinha, C. S. Riera, J. W. Hutchinson, L. Mahadevan, and D. A. Weitz. Onset of Buckling in Drying Droplets of Colloidal Suspensions. *Physical Review Letters* **94**(1), 018302+ January (2005).

[163] M. Ulbricht. Advanced functional polymer membranes. *Polymer* **47**(7), 2217–2262 March (2006).

[164] A. van Blaaderen and P. Wiltzius. Real-Space Structure of Colloidal Hard-Sphere Glasses. *Science* **270**(5239), 1177–1179 November (1995).

[165] D. Vella, P. Aussillous, and L. Mahadevan. Elasticity of an interfacial particle raft. *EPL (Europhysics Letters)* , 212+ October (2004).

[166] J. Vermant. Fluid mechanics: When shape matters. *Nature* **476**(7360), 286–287 August (2011).

[167] G. A. Vliegenthart and G. Gompper. Compression, crumpling and collapse of spherical shells and capsules. *New Journal of Physics* **13**(4), 045020+ April (2011).

[168] K. Watanabe and H. Tanaka. Direct observation of medium-range crystalline order in granular liquids near the glass transition. *Physical Review Letters* **100** (2008).

[169] E. Weeks, J. C. Crocker, A. C. Levitt, A. Schofield, and D. Weitz. *Science* **287** January (2000).

[170] D. A. Weitz. Physics: Packing in the spheres. *Science* **303**(5660), 968–969 February (2004).

[171] B. M. Weon and J. H. Je. Capillary force repels coffee-ring effect. *Physical Review E* **82**(1), 015305 July (2010).

[172] A. Widmer-Cooper and P. Harrowell. Free volume cannot explain the spatial heterogeneity of debye-waller factors in a glass-forming binary alloy. *Journal of Non-Crystalline Solids* **352**, 5098–5102 November (2006).

[173] A. Widmer-Cooper and P. Harrowell. Predicting the long-time dynamic heterogeneity in a supercooled liquid on the basis of short-time heterogeneities. *Physical Review Letters* **96** (2006).

[174] A. Widmer-Cooper, H. Perry, P. Harrowell, and D. R. Reichman. Irreversible reorganization in a supercooled liquid originates from localized soft modes. *Nature Physics* **4**, 711–715 (2008).

[175] S. Williams, I. Snook, and W. van Megen. Molecular dynamics study of the stability of the hard sphere glass. *Physical Review E* **64** (2001).

[176] J. Wu, B. Zhou, and Z. Hu. Phase behavior of thermally responsive microgel colloids. *Physical Review Letters* **90**, 048304+ January (2003).

[177] M. Wyart. Scaling of phononic transport with connectivity in amorphous solids. *EPL (Europhysics Letters)* , 64001+ March (2010).

[178] M. Wyart, S. R. Nagel, and T. A. Witten. Geometric origin of excess low-frequency vibrational modes in weakly connected amorphous solids. *EPL (Europhysics Letters)* , 486+ November (2005).

[179] R. Yamamoto and A. Onuki. Dynamics of highly supercooled liquids: Heterogeneity, rheology, and diffusion. *Physical Review E* **58**, 3515+ (1998).

[180] G. Yatsenko and K. S. Schweizer. Ideal glass transitions, shear modulus, activated dynamics, and yielding in fluids of nonspherical objects. *The Journal of Chemical Physics* **126**(1), 014505+ (2007).

[181] P. Yunker, Z. Zhang, K. B. Aptowicz, and A. G. Yodh. Irreversible Rearrangements, Correlated Domains, and Local Structure in Aging Glasses. *Physical Review Letters* **103**(11), 115701+ Sep (2009).

[182] P. Yunker, Z. Zhang, and A. G. Yodh. Observation of the Disorder-Induced Crystal-to-Glass Transition. *Physical Review Letters* **104**(1), 015701+ Jan (2010).

[183] P. J. Yunker, K. Chen, Z. Zhang, W. G. Ellenbroek, A. J. Liu, and A. G. Yodh. Rotational and translational phonon modes in glasses composed of ellipsoidal particles. *Physical Review E* **83**(1), 011403+ January (2011).

[184] P. J. Yunker, K. Chen, Z. Zhang, and A. G. Yodh. Phonon Spectra, Nearest Neighbors, and Mechanical Stability of Disordered Colloidal Clusters with Attractive Interactions. *Physical Review Letters* **106**(22), 225503+ June (2011).

[185] P. J. Yunker, M. Gratale, M. A. Lohr, T. Still, T. C. Lubensky, and A. G. Yodh. *Physical Review Letters, In press* (2012).

[186] P. J. Yunker, T. Still, M. A. Lohr, and A. G. Yodh. Suppression of the coffee-ring effect by shape-dependent capillary interactions. *Nature* **476**(7360), 308–311 August (2011).

[187] E. Zaccarelli, C. Valeriani, E. Sanz, W. C. K. Poon, M. E. Cates, and P. N. Pusey. Crystallization of hard-sphere glasses. *Physical Review Letters* **103** (2009).

[188] E. Zaccarelli. Colloidal gels: equilibrium and non-equilibrium routes. *Journal of Physics: Condensed Matter* **19**(32), 323101+ August (2007).

[189] Z. Zeravcic, N. Xu, A. J. Liu, S. R. Nagel, and W. V. Saarloos. Excitations of ellipsoid packings near jamming. *EPL (Europhysics Letters)* **87**(2), 26001+ July (2009).

[190] M. Zhang, S. Mancini, W. Bresser, and P. Boolchand. Variation of glass transition temperature, Tg, with average coordination number, łm, in network glasses: evidence of a threshold behavior in the slope —dTg/dłm — at the rigidity percolation threshold (łm = 2.4). *Journal of Non-Crystalline Solids* **151**(1-2), 149–154 December (1992).

[191] Z. Zhang, N. Xu, D. T. Chen, P. Yunker, A. M. Alsayed, K. B. Aptowicz, P. Habdas, A. J. Liu, S. R. Nagel, and A. G. Yodh. Thermal vestige of the zero-temperature jamming transition. *Nature* **459**(7244), 230–233 May (2009).

[192] Z. Zhang, P. J. Yunker, P. Habdas, and A. G. Yodh. Cooperative Rearrangement Regions and Dynamical Heterogeneities in Colloidal Glasses with Attractive Versus Repulsive Interactions. *Physical Review Letters* **107**, 208303+ November (2011).